**The Dissertation Committee for Carlos Andres Aguilar Certifies that this is the approved version of the following dissertation:**

# Synthesis, Characterization and Integration of Piezoelectric Zinc Oxide Nanowires

**Committee:**

Shaochen Chen, Supervisor

Marc D. Feldman

Brian Korgel

Dean Neikirk

Li Shi

Krishnendu Roy

# Synthesis, Characterization and Integration of Piezoelectric Zinc Oxide Nanowires

**by**

**Carlos Andres Aguilar, B.S.E.; M.S.E.**

**Dissertation**

Presented to the Faculty of the Graduate School of

The University of Texas at Austin

in Partial Fulfillment

of the Requirements

for the Degree of

**Doctor of Philosophy**

**The University of Texas at Austin**

**December 2008**

# Dedication

For my family

## Acknowledgements

It would be incredibly long if I thanked everyone who has ever helped me or sacrificed so I could write this and be in this position. I apologize if you weren't listed here.

From the beginning, I have been surrounded with people that have guided me on my path. I would like to thank several teachers from high school, most notably Eduardo Cancino and Juan Ibarra for seeing the potential in me. I would like to offer thanks to my high school football coach Ernest Sanchez, for teaching me about how to take the hardest hits and keep my feet moving. My appreciation goes to my undergraduate advisor at Michigan, Prof. Noel Perkins, who taught me to enjoy struggling for solutions. My deepest thanks go to my undergraduate mentor at Michigan, Prof. Steven Skerlos, who defines the Michigan Difference and without, I wouldn't have attended graduate school. I would like to thank my supervisor here at Texas, Prof. Shaochen Chen, for supporting me through my doctoral study and for the opportunity to work with him. I would like to thank my co-supervisor here at Texas, Dr. Marc Feldman, for his encouragement and invaluable comments during this dissertation. I am indebted to Prof. Brian Korgel, for teaching me about the growth of nanostructures and for always lending an ear to help guide this research. I would like to extend my gratitude to Prof. Li Shi for his encouragement, advice and helping push me when things didn't work. I want to also thank Prof. Dean Neikirk and Prof. Krish Roy for serving in my committee and carefully reading this dissertation. I would also like to thank Doh C. Lee, of Brian Korgel's group for helping this project get started and teaching me about growth of nanostructures in solution, Anastassios Mavrokefalos of Li Shi's group for his assistance with the nanomanipulator and discussions, Brandon Beberwyck of Shaochen Chen's group for his

assistance, Vahid Akhavan of Brian Korgel's group for his input, Dr. Richard Haight at IBM-Research for the opportunity to work with him on the PES project and for many fruitful conversations, Prof. Jeffrey Schwartz of Princeton University for discussions and insight on the PES project, Li-Hsin Han of Shaochen Chen's group for guidance on this work and life, Dr. Ranjani Sirdeshmukh at IBM-Research for help with the patterned Si substrates in the PES project, Brian Long of Grant Willson's group for help in calculating the dipole moments of the molecules, and Lori Greene in Prof. Peidong Yang's group at the University of California-Berkeley for her help and insight with the synthesis.

Beyond the people in academia, my sisters, cousins, aunts and uncles and grandmothers have galvanized me to reach higher and taught me the best measures of success are those found within. I'm thankful to them for listening to me and providing guidance whenever I needed it. I'm very appreciate of my friends (in particular Kristan Diaz, Paul Rogers, Chuck Martinez, Angelo McDowell, Mike Martinez, Rico Luna, Ita Villanueva, Mathew Palmer, Sean Whitney, Chris Leis, Mike Kiplinger, Rob Lange, Steve Tom, Andy Vilardo, Brian Marchena, Joe Niewiadomski, Derek Bell, Alex Heltzel, Anastassios Mavrokefalos) for always making me feel home and laugh my way through the hardest and best times. I can't thank my fiancé Elizabeth with words here, but offer a small thanks for always having faith in me. You are the compass that guides my life…Lastly, my mother Cynthia and father Raul; there aren't words big enough to thank you and even if there were, words written here still wouldn't be good enough. I can only write one thing to you two and imagine y'all reading it; no matter what I attempt to call myself after this, it will never define me. Being your son defines me and always will.

# Synthesis, Characterization and Integration of Piezoelectric Zinc Oxide Nanowires

Publication No._____

Carlos Andres Aguilar, Ph.D.

The University of Texas at Austin, 2008

Supervisor: Shaochen Chen

An automatic implantable cardiac defibrillator (AICD) is a device that is implanted in the chest to constantly monitor and, if necessary, correct episodes of arrhythmia. While the longevity of the average AICD patient has increased to 10 years after implantation, only 5% of implants functioned for seven years, and this mismatch poses a significant and ever growing clinical and economic burden. Moreover, there are now efforts to "piggyback" devices on AICDs and BVPs for additional functionality, all of which require more power. An innovative approach towards generating power for AICDs is to harness the energy of the heart by embedding energy generators in AICD leads. The cardiovascular system as a source generator is appealing due to its ability to continuously deliver mechanical energy as long as the patient is alive.

Herein a device incorporating nanostructured piezoelectrics was developed as a means to harvest the energy of heart. The generator system integrates inorganic piezoelectric nanomaterials, including aligned arrays of nanowires of crystalline zinc oxide (ZnO), with elastomeric substrates. The design combines several innovative structural configurations including a "wavy" flexible electrode and a layout where the nanowires are near or on the neutral mechanical plane. A wet synthetic strategy to reliably prepare piezoelectric ZnO nanostructures directly onto the devices was also developed and optimized to produce nanowires with high densities, large aspect ratios and high orientation. The elastomeric support permits direct integration within AICD leads and is small and flexible enough to not add resistance in systole. The flexible devices were integrated into a testbed mimicking the input a failing right ventricle and the results demonstrate progress towards energy harvesting from the cardiovascular system. A model was developed to gain insight as to how to structure the nanowire array within the

latitude of the synthesis to boost the energy production. To further improve the output, the nanowires were passivated with dipolar molecules to change their resistivities and the barrier height of the Schottky contact. A novel low photon energy photoelectron spectroscopy tool was developed to measure the effects of the molecules on the individual nanowire properties. This concept of using nanostructured piezoelectrics as a means to convert the energy of the body may in the coming years represent a paradigm shift from battery dependant AICD modules to completely autonomous functional systems.

***J.J.***

# Table of Contents

List of Tables ..... xi

List of Figures ..... xii

Chapter 1 Introduction ..... 1

1.1 Rationale ..... 1

1.2 Power for AICDs and BVPs and Other Medical Implants ..... 3

1.3 Body Powered Generators ..... 4

1.4 Piezoelectric Materials For Use In Body Powered Generators ..... 6

1.5 Piezoelectric Nanowires ..... 21

1.6 Synthesis of Nanostructures ..... 22

1.7 Device Development ..... 25

1.8 Optimization of Generator for Enhanced Response and Lifetime ..... 26

1.9 Development of Single Nanowire Photoelectron Spectroscopy Tool ..... 28

Chapter 2 Optimized Synthesis ..... 29

2.1 Optimized Synthesis of Piezoelectric Nanostructures ..... 33

2.2 ZnO Nanocrystal Synthesis ..... 34

2.2.1 Spherical ZnO Nanoparticle Synthesis ..... 34

2.2.2 Quasi-Spherical ZnO Nanoparticle Synthesis ..... 36

2.2.3 Triangular ZnO Nanoprism Synthesis ..... 38

2.2.4 'C-axis' Textured ZnO Nanoplatelet Synthesis ..... 41

2.3 Hydrothermal ZnO Nanowire Growth ..... 44

2.3.1 Optimized Point of Entry into Growth Solution ..... 51

2.3.2 Growth of High Aspect Ratio Nanowires ..... 53

2.3.3 Further Enhancement of Aspect Ratio of ZnO Nanowires ..... 56

2.3.4 Limit to Aspect Ratio of Nanowires ..... 59

2.3.5 Ostwald Ripening of Nanowires After Extended Growth ..... 63

2.3.6 Effect of Substrate on Nanowire Aspect Ratio and Orientation ..... 66

2.3.7 Optimized Oriented Growth on Flexible Substrates ..... 70

2.3.8 Oriented Growth on Relief Patterned Flexible Substrates ..... 71

2.4 Conclusions....81

Chapter 3 Piezoelectric Performance of ZnO Nanowire Arrays....83

3.1 Cost of Harvesting Metric....84

3.1.1 Generator Location and Initial Materials Selection....84

3.1.2 Performance of Polymeric Piezoelectric Generator....86

3.2 Methods to Improve Performance of Piezoelectric Generator....89

3.3 1st Generation Nanostructured Piezoelectric Device....94

3.4 2nd Generation Nanostructured Piezoelectric Device....103

3.5 Optimization Model....115

3.6 Conclusions....124

Chapter 4 Molecular Engineered ZnO Nanowires....128

4.1 Low Photon Energy Photoelectron Spectroscopy....129

4.2 Experimental Design and Setup....132

4.3 Electronic Properties of Individual ZnO Nanowires....137

4.3.1 Surface Sensitivity of Nanowire Electronic Properties....140

4.4 Molecular Engineered Nanowire Electronic Properties....148

4.4.1 Functionalization of Nanowires Using T-BAG Method....149

4.5 Conclusions....159

Chapter 5 Conclusions and Outlook....161

5.1 Conclusions....161

5.2 Outlook....163

References....167

Vita....176

# List of Tables

Table 4.1: Comparison of changes to ZnO nanowire work functions .....158

# List of Figures

Figure 1.1: Longevity of standard and large-battery-capacity AICDs ..... 3
Figure 1.2: Molecular model of piezoelectric crystal ..... 10
Figure 1.3: Piezoelectric coefficients and associated axes ..... 12
Figure 1.4: Loading configurations for piezoelectric generators ..... 13
Figure 1.5: Schematics of several piezoelectric composite structures ..... 17
Figure 1.6: Schematic of a 1-3 piezoelectric nanowire: polymer composite ..... 18
Figure 1.7: Vapor-Liquid-Solid (VLS) growth mechanism ..... 23
Figure 1.8: Idealized Diagram of Solution-Liquid-Solid Growth ..... 23
Figure 2.1: Diagram of Nucleation and Growth. ..... 30
Figure 2.2: Structural model of ZnO ..... 32
Figure 2.3: Spherical ZnO nanoparticles. ..... 36
Figure 2.4: Quasi-spherical ZnO nanoplatelets ..... 38
Figure 2.5: Triangular nanoprisms of ZnO ..... 40
Figure 2.6: 'C-axis' textured ZnO nanoplatelets. ..... 43
Figure 2.7: Nanowire arrays grown from each type of catalyst seed ..... 51
Figure 2.8: Optimized point of entry for the substrate into the reaction bath ..... 53
Figure 2.9: Growth of high aspect ratio nanowires ..... 54
Figure 2.10: Automated system to produce high-aspect ratio nanowires ..... 55
Figure 2.11: Optimized extended growth of nanowires ..... 56
Figure 2.12: Further enhancement of aspect ratio of ZnO nanowires ..... 59
Figure 2.13: Limit to nanowire aspect ratio ..... 61
Figure 2.14: Higher density of catalyst seeds induced Ostwald ripening ..... 62
Figure 2.15: Ostwald ripening of nanowires grown for extended periods ..... 66

Figure 2.16: Effect of substrate on nanowire aspect ratio and orientation. .....68
Figure 2.17: Effect of polymer substrate on orientation of nanowire array .....70
Figure 2.18: Optimized oriented growth on flexible substrates .....71
Figure 2.19: Preparation of disordered metal films on PDMS .....73
Figure 2.20: Preparation of wrinkled metal films on patterned PDMS.....77
Figure 2.21: Growth of highly oriented nanowire arrays on wavy metal films ....80
Figure 3.1: Initial experimentation with PVDF.....87
Figure 3.2: Schematic of integrated circuit .....88
Figure 3.3: Charging rate of PVDF film(s) in simulated systole .....89
Figure 3.4: Optimal shape to oppose RV deformation.....92
Figure 3.5: Proposed location for helical coiled generator.....93
Figure 3.6: 1st-generation device substrate. .....95
Figure 3.7: SEM image of nanowires extending from grafted polymer layer.....97
Figure 3.8: Completed device characteristics.....98
Figure 3.9: Diagram of modified testbed .....100
Figure 3.10: SEM images of nanowires fractured from device.....102
Figure 3.11: 'Sandwich' styled device. .....103
Figure 3.12: Profilometer scans of masters created from optical lithography ....106
Figure 3.13: Schematic of process flow to create PDMS spacer layer .....108
Figure 3.14: Nanowire output during single loading.....111
Figure 3.15: Nanowire output during cyclic loading.....113
Figure 3.16: Schematic of bending of surface buckled structures on PDMS.....114
Figure 3.17: Illustration of coordinate system to define AICD lead parameters.116
Figure 3.18: Minimum force to bend nanowires with varying aspect ratios.....118
Figure 3.19: Strain as a function of deflection angle for various aspect ratios ...119

Figure 3.20: Current output versus degrees deflected by the nanowire .....120
Figure 3.21: Current as a function of aspect ratio .....121
Figure 3.22: Role of Young's Modulus in output current.....122
Figure 4.1: Theoretical framework for PES experiment .....132
Figure 4.2: Experimental setup to perform PES on individual nanowires.....133
Figure 4.3: Nanomanipulation assembly and integration.....136
Figure 4.4: SEM image of nanowire extending into patterned gap.....137
Figure 4.5: Photoelectron spectra of individual native ZnO nanowire .....140
Figure 4.6: Spectra after thermolysis of electronegative adsorbates.....143
Figure 4.7: Photoelectron spectra after annealing in dry oxygen.....146
Figure 4.8: Photolysis of $O_2^-$ and $CO_2^-$ from the nanowire surface.....147
Figure 4.9: Functionalization of nanowires using T-BAG method.....150
Figure 4.10: Spectra of ZnO nanowires coated with electron-donating SAMs..152
Figure 4.11: FTIR spectra of nanowires grafted with electron-accepting SAMs154
Figure 4.12: Spectrum of ZnO nanowire coated with electron-accepting SAMs155
Figure 4.13: FTIR spectra of nanowires grafted with electron-accepting SAMs156

# Chapter 1: Introduction

This dissertation focused on the synthesis, characterization, and integration of piezoelectric zinc oxide nanowires for use in development of a nanostructured flexible electronic device to convert cardiac motion into electrical power for Automatic Implantable Cardiac Defibrillators and bi-ventricular pacemakers. This chapter describes the motivation of these experiments as well as a brief introduction.

## 1.1 RATIONALE

According to estimates from the World Health Organization (WHO), 16.7 million people around the world die of heart disease each year, which contributes to nearly one-third of global deaths. In the United States, heart disease has been the number one killer each year since 1900, causing more than 700,000 deaths per year since the 1960s. The estimated direct and indirect cost of heart disease in 2004 was $368.4 billion. Nearly half of the deaths from coronary heart disease are from sudden deaths caused by cardiac arrest[1].

The leading cause of sudden cardiac death is ventricular fibrillation (V-FIB). An Automatic Implantable Cardiac Defibrillator (AICD) can prevent sudden cardiac death from V-FIB by an early defibrillation (large jolt of electricity to "reset" the heart rate). An AICD is a device that is implanted in the chest to constantly monitor and, if necessary, correct episodes of arrhythmia. Most AICDs are combined with a bi-ventricular pacemaker (BVP)[2], a type of implantable pacemaker designed to simultaneously treat both ventricles when they do not pump in unison. Both BVPs and AICDs typically consist of a sealed, battery-powered, sensor-laden pulse generator;

several steroid-tipped wire electrodes (or leads) that connect the pulse generator to the myocardium; and a custom ultra-low power microprocessor with very little RAM for telemetry storage. The primary corrective functions of an AICD are to control tachycardia through cardioversion (low-energy shocks to convert the heart rhythm to a more normal rate) and manage V-FIB through defibrillation. Conventional pacemakers regulate the right atrium and right ventricle (Atrium-Ventricle (AV) synchrony), while BVPs add a third lead to help the left ventricle contract at the same time.

Over 100,000 patients received AICDs in 2004, an increase of 58% from 2002. Publication of the Madit II, SCDHeFT, COMPANION, and CARE – HF trials has made it clear that the majority of patients with cardiomyopathy of any cause will benefit from placement of AICD and BVP to both reduce hospital admissions and prolong life[3,4,5,6]. The SCD-HeFT study results alone could double the number of ICD implants in the next few years. Based on data from the Multicenter Registry, approximately 70% of AICDs and BVPs implanted in 2004 will require replacement because of battery depletion over the next five years[7,8]. While the longevity of the average AICD patient has increased to 10 years after implantation, only 5% of implants functioned for seven years (Fig. 1.1), and this mismatch poses a significant and ever growing clinical and economic burden[9]. Furthermore, approximately 90% of AICD failures were caused by normal battery depletion and the shift to dual-chamber models has significantly shortened battery life even further. Since each AICD shock consumes 14 to 40 J, a single defibrillation can reduce an AICD's lifetime by several weeks[10]. Moreover, there are now efforts to "piggyback" devices on AICDs and BVPs for additional functionality such as pressure and volume sensors to warn of impending congestive heart failure (CHF), lung

impedance sensors to warn of CHF and chemical sensors to provide telemetric measures of glucose, potassium, bun and creatinine, all of which would require additional power.

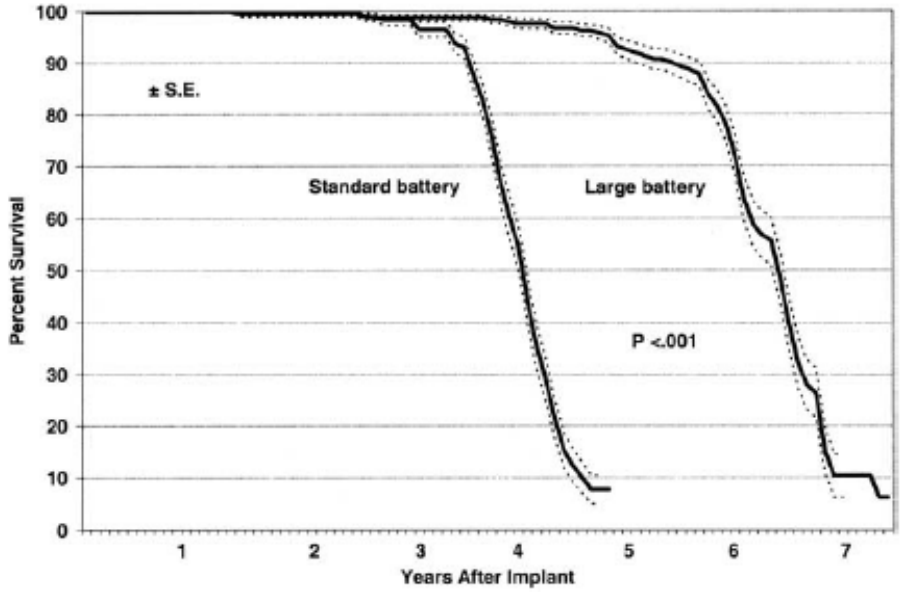


Figure 1.1: Longevity of standard and large-battery-capacity AICDs (Reproduced from [8]).

Clinical studies that quantify the risks of regular AICD and BVP replacement surgeries demonstrate 4 of every 5 device implant infections happen in the "pocket" where the replacement device sits[11]. Since an infection in the “pocket” from a generator replacement raises risk of death 300%, and other complications from surgery such as bleeding and potential lead damage can occur[12], it is imperative to reduce replacement surgeries to prevent morbidity and increased risk of death.

## 1.2 POWER FOR AICDS AND BVPS AND OTHER MEDICAL IMPLANTS

Methods to provide longer lifetimes for AICD and BVPs and other medical implants include using larger batteries, nuclear power and inductive charging through

subcutaneous coils. Using larger batteries and in turn larger pulse generators may increase the risk of pocket complications, including erosion and discomfort, and most patients would not accept such models. Nuclear-powered batteries were shown to last considerably longer than conventional battery-powered units and concerns regarding environmental hazards, dermal, subcutaneous reactions and carcinogenesis were unfounded.[13] However, patients still expressed concerns about high initial costs, radiation effects, integrity of the encapsulation of the radioisotope during unexpected trauma, and larger implant sizes. Of the medical implants that contain rechargeable batteries such as neurological pain management devices, the most common method of recharging the battery uses induction through subcutaneous coils inside the housing. This scheme is inherently limited due to the high frequency of prolonged charging times, which can be weekly for hours at a time. Another potential problem for recharging externally in a life-critical device such as an AICD and BVP would be patient compliance, where the potential penalty for a missed recharging appointment would be death. With increasing demands from decreases in size and enhanced capabilities of AICDs and BVPs, new ways to supply electrical energy to these devices is necessitated. An innovative approach towards generating power for implantable devices is to develop and store energy at the device by scavenging energy from human movement.

## 1.3 BODY POWERED GENERATORS

The human body provides a remarkable storehouse for energy, consuming power at a rate of 81-1630W a day[14]. While the energy expenditure of the human body is large, harnessing a fraction of this power is relatively cumbersome without putting an onerous load on the person. To date the most successful power recovery schemes from body

motion have been demonstrated from walking[15] and pedaling[16]. Several other schemes using body heat, respiration[17], and arm motion[18] have also been demonstrated but their power generation has been limited. Recently, high frequency ultrasonic wave energy generators[19] have been developed to potentially draw power from blood pressure pulses but the hydraulic energy in our blood operates typically at much lower frequencies (>10Hz). Moreover, the integration of such power scavenging devices into AICD/BVP technology would require multiple devices to generate practical power outputs which in turn would demand obtrusive interconnects and distribution lines inside the body that would ultimately reduce their power generating efficiency. Therefore such a system would be cumbersome and impractical for a user in addition to requiring additional surgical implantation.

Even though theoretically all moving systems of the body can be considered power generators, systems that operate intermittently such as arm movement, typing and gait will be limited to operation during the specific exercise. Activities such as cardiac contraction, arterial wall distension and expansions of the thorax, that operate continuously without interruption offer more promising avenues to pursue body-powered generators. The cardiovascular system as a source generator is appealing due to its ability to continuously deliver mechanical energy as long as the patient is alive.

The systolic ventricular mechanics of a failing heart have been studied using tagged MRI and showed the free wall of a right ventricle (RV) undergoes the largest displacement (~10-14mm)[20], making it the most natural location to place an energy generator. Since the free wall of the RV is the site of attachment for an AICD lead, a generator placed inside a lead can be directly integrated into existing AICD technology

without interconnects and harness the local RV free wall displacements[21]. Admittedly, scavenging all or most of the energy of the heart would be impossible but if an efficient generator could scavenge a fraction of the power output, remove it imperceptibly and efficiently store the energy over time, a significant amount of energy can be extracted from the cardiovascular system. Moreover, by integrating a generator inside the lead, the generator is protected from body fluids and macrophages which could potentially degrade or break down the device.

Attempts to tap the kinetic energy of the cardiovascular system for the expressed purpose of generating electric power to drive in vivo systems saw heavy research several decades ago[22,23,24,25,26]. However, implantable batteries and low-power electronics had not been developed well enough because the generated electric power was much to low to rely solely on biological power. Recently, remarkable progress in electronics engineering has made it possible to drive a cardiac pacemaker with as little as 50μW worth of power. As better and longer-lasting batteries were introduced to pacemakers in the 80s, research to harvest the kinetic motion of the heart resurged[27,28,29,30] and then quickly subsided due to lack of market interest. However, given the recent trend for added functionality from AICDs and BVPs, smaller modules, and the problems associated with replacements, the need for alternative sources of power becomes more apparent.

## 1.4 PIEZOELECTRIC MATERIALS FOR USE IN BODY POWERED GENERATORS

There are three types of electro-mechanical devices that can perform energy conversion and they are electrostatic, electromagnetic and piezoelectric. Electromagnetic materials produce electricity from the motion of a magnetic field relative to a conductive coil, which causes current to flow in the coil. Typically, the electricity is generated by

either the relative movement of the magnet and coil, or due to changes in the magnetic field. Therefore, the amount of electricity that can be generated is a function of magnetic field strength, relative motion velocity and the number of turns in the coil. In most systems, the magnets are attached to a cantilever and act as inertial masses. Electromagnetic energy harvesters are well established and macroscaled, high-performance bulk magnets and multi-turn, large coils are readily available. The electromagnetic energy systems also require no input voltage source to initiate power generation. However, the production of micro and nano-scaled magnets has remained a challenge due to non-planar fabrication methods. In the case of recharging a battery inside an AICD lead, the number of turns that can be achieved with a set of planar coils would be greatly reduced. Moreover, the amplitudes of vibration and reduced relative velocities would limit the energy production from such a set of devices. Finally, assembly and integration of sub-millimeter electromagnetic energy harvesting systems into an AICD lead would be exigent due to the curved surface of the lead and plastic casing.

Electrostatic generators are comprised of two conductive plates that are electrically isolated from air, vacuum, or a dielectric insulator (capacitor), which move relative to one another. There are two modes of electrostatic energy conversion: one where the charge on the capacitor is constrained, while the voltage increases and the capacitance decreases and the other when the voltage across the capacitor is constrained, while the charge moves from the capacitor as the capacitance decreases. The plates are charged via an external source such as a battery. Charging of the plates creates equal and opposite charges on the plates, which results in stored charge when the source is disconnected. The harvested energy is derived from the work done against the

electrostatic force between the plates. Electrostatic energy harvesters are excellent candidates for further integration into microsystems with work done already on in-plane and out-of-plane capacitors[31]. The energy density of a variable capacitor (VC), which is a component of the electrostatic generator, can be raised by enlarging the surface area of electrodes and shortening the gap between electrodes. An attempt to scavenge the power of the left ventricle of a canine was attempted with such an electrostatic generator[32], but the generator was too large to put on the LV free wall. As a proof of concept, the VC generator followed the motion of a simulated LV and was able to produce enough power to drive a cardiac pacemaker for 2 hours. In order for this type of device to be physiologically realizable, the size of the device must be reduced to less than $1cm^3$ without compromising the energy density. Since the energy density of an electrostatic generator scales as volume to the ($^4/_3$), different geometries and/or better materials that accommodate the same type of energy production must be implemented. One such example may be to use micro-electro-mechanical-systems (MEMS) and/or nano-electro-mechanical-systems (NEMS) comb-drive actuators. A comb-drive actuator uses the same principle as a VC, as one comb slides back and forth by an external stimulation relative to a fixed electrode, the capacitance is changed. If three-dimensional micro or nano comb-type VCs could be batch fabricated within the limits of the fatigue of systolic function and assembled into an AICD lead, a physiologically realizable device(s) may be accomplished. However, fabrication of such a device inside an AICD lead, where space is limited, would again face daunting challenges of non-planar fabrication and transfer. Moreover, such an electrostatic generator would still require an input charge or voltage to operate. Additionally, since the output impedance and voltage is high in this type of device, its current output tends to be low and limits it potential as a power supply. Considering custom circuitry and signal processing could circumvent the aforementioned

problems, the parasitic capacitance within any type of electrostatic generator (micro/nano or macro) would still plague the efficiency. Lastly, in such a confined space as in an AICD lead, with such small capacitor spacing for a micro/nano VC, the issue of electrodes shorting would significantly limit device performance.

Of the three types of energy transducers, a piezoelectric transducer that makes use of the material's electro-mechanical coupling to covert energy is the most attractive owing to the potentially greater energy densities achievable than that with electrostatic or electromagnetic devices[33,34]. Piezoelectrics produce an electrical charge via strain from an external mechanical load. A molecular model of a piezoelectric is displayed in Figure 1.2a, where the centers of positive and negative charges of each molecule cancel one another. When an external load is applied, the molecular structure is distorted whereby the positive and negative charges are separated (Figure 1.2b), resulting electric dipoles within the material. The collective phenomenon of the dipoles result in an electric polarization of the material, where the dipoles within the material cancel one another, and centers of positive charge accumulate at the cathode and centers of negative charge accumulate at the anode (Figure 1.2c). The net polarization is reversed as current is allowed to flow in the material and neutralize the charge (Figure 1.2d).

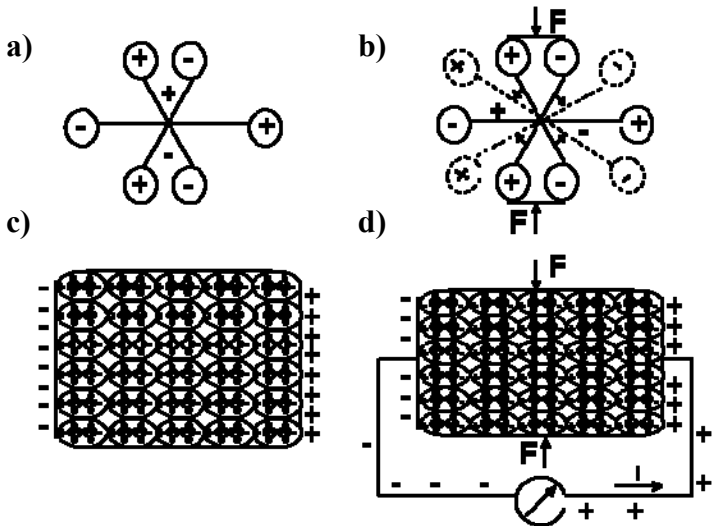


Figure 1.2: Molecular model of piezoelectric crystal. a) Undisturbed molecular model of piezoelectric where internal molecular charges cancel each other. b) Molecular structure after mechanical load is applied causing positive and negative gravity centers to displace and create dipoles. c) Polarized piezoelectric, where internal dipoles cancel each other and charge is present on both surfaces in opposite sign. d) Reversal of net polarization due to current flow (Reproduced from [33]).

The only drawback of a piezoelectric generator is it would require a step-down transformer to decrease the losses and a regulator to condition the signal. This issue can easily be solved with minimal additional circuitry into the AICD housing. However, since the produced piezoelectric output is intermittent and relatively small, storing the rectified charge must be addressed. The most direct solution to the problem of electrical storage is to charge a capacitor or array of capacitors that can be drained for power during periods of no power generation. While simply charging one or several capacitors will result in some additional losses, it may not be such a restraint for the case of energy harvesting from the heart because of the low power requirement of an AICD and BVP.

Fabrication techniques to produce micro and nano-scaled as well as macro-scaled piezoelectric devices such as thick and thin-film deposition enable their integration into more complex geometries. Furthermore, piezoelectrics do not require an input voltage to operate as opposed to electrostatic devices. Bearing in mind that any technique that harvests the heart's energy must be totally unobtrusive and not increase the load on the heart, only a limited suite of piezoelectric technologies are available to parasitically scavenge energy.

In principle, a piezoelectric structure designed to efficiently convert the kinetic motion of the heart into power for an implantable device would be flexible, nontoxic, possess a high piezoelectric coefficient (mechanical-to-electrical conversion), not present any load on the heart, utilize multiple inputs (for a fail-safe and redundant design), sustain a long lifetime, and be able to act synergistically with the implantable device lead. We see from the governing equations for a piezoelectric material (equations 1.1-1.6) that optimizing a piezoelectric device will roughly depend on three factors: (a) *the material's piezoelectric properties, (b) the mechanical or electrical excitation vector, and (c) the structure's dimensions and geometry*.

The relationships between the response of a piezoelectric element and the force applied are:

$$S_{ij} = s^{E}_{ijkl}T_{kl} + d_{ijk}E_k \tag{1.1}$$

$$D_i = d_{ikl}T_{kl} + \varepsilon^{T}_{ik}E_k \tag{1.2}$$

where S is the second-rank strain tensor, $s^E$ is the fourth-rank elastic compliance tensor at a constant electric field ($m^2/N$), T is the second-rank stress tensor ($N/m^2$), d is the third-rank piezoelectric tensor coefficient (m/V), E is the first-rank electric field tensor (V/m), D is the first rank electric displacement tensor ($C/m^2$) and $\varepsilon^T$ is the second-rank permittivity matrix at a constant stress ($N/V^2$). The subscripts in the coefficients correspond to directions of the electrodes (i,j,k) and direction of the applied load (l) (figure 1.3). The three-dimensional piezoelectric coefficient tensor can be reduced to a more tractable 2-dimesional matrix due to crystal symmetry ($d_{ikl} \rightarrow d_{ik}$) and reduced from nine coefficients to six because it is a symmetrical tensor ($d_{ik} = d_{ki}$). Rewritten in full form, the piezoelectric coefficient matrix for most high performance piezoelectrics can be described by the matrix below:

**a)**

$$d_{ik} = \begin{pmatrix} 0 & 0 & 0 & 0 & d_{15} & 0 \\ 0 & 0 & 0 & d_{15} & 0 & 0 \\ d_{31} & d_{31} & d_{33} & 0 & 0 & 0 \end{pmatrix}$$

**b)**

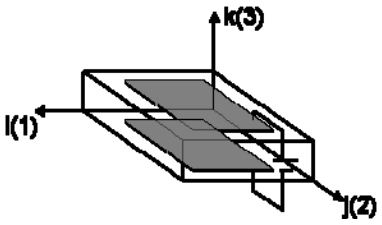


Figure 1.3: Piezoelectric coefficients and associated axes. a) Piezoelectric coefficient matrix for most high-performance piezoelectric materials. b) Schematic of different directions a piezoelectric material can be loaded and polarized. The '5' subscript corresponds to a shear direction or twist of the material (Reproduced from [33]).

In Figure 1.3a, the six different piezoelectric coefficients are listed and vary according to loading direction. The most common loading configurations for piezoelectric generators are the '31' and '33' loadings. In the '31' mode, charge is collected on the electrode surface perpendicular to the polarization direction (Figure 1.4a). In the '33' mode, charge is collected on the electrode surfaces that are parallel to the polarization direction (Figure 1.4b). In this case, the stress and direction of the

polarization / direction of voltage act in the same direction. The '33' coefficient is largest in most materials and therefore achieves the highest rate of energy conversion. However, for a limited device size such as in an AICD lead, the '31' loading mode may be more appropriate as it can accommodate larger strains from smaller input forces.

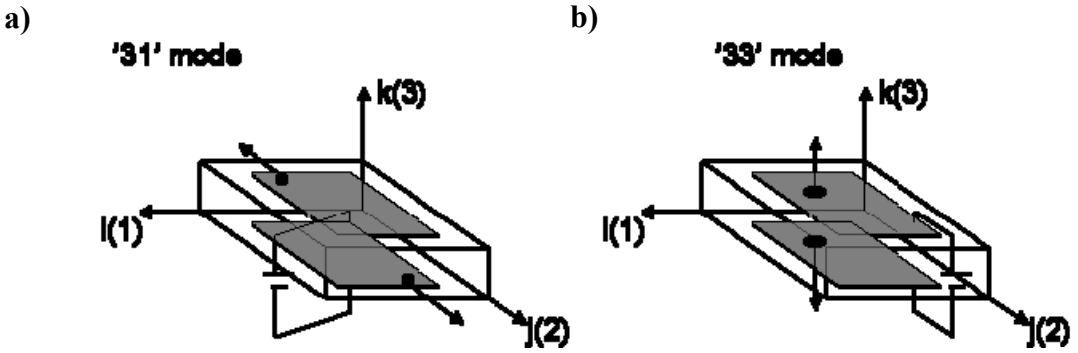


Figure 1.4: Loading configurations for piezoelectric generators. (a) '31' loading where the direction of the loading is perpendicular to the direction the voltage is collected. (b) '33' loading where the direction of the loading is parallel to the direction the voltage is collected (Reproduced from [33]).

Since the dimension of an AICD lead and the excitation vector of the heart or mechanical load are fixed components, the material properties of a piezoelectric must be tailored to extract the largest possible response. To view how to optimize the material properties, the electromechanical coupling factor (k), which is the ratio of stored electrical energy per input mechanical energy, and its related quantities must be examined. The coupling coefficient (k) for a piezoelectric generator is depicted below in equation 1.3:

$$k^2 = d_{ik}^{2*}E_y / \varepsilon = d_{ik}^2 / \varepsilon_o * K * s \qquad (1.3)$$

where $d_{ik}$ is the piezoelectric coefficient, $E_y$ is the Young's modulus and $\varepsilon$ is the permittivity of the material. The relationship may also be rewritten in terms of the elastic compliance (s), dielectric constant (K) and permittivity of the free space ($\varepsilon_o$). However, not all of the stored electrical energy can actually be used, and the actual work done by the device depends on the mechanical load. Therefore the energy transmission coefficient ($\lambda$) in equation 1.4 is introduced:

$$\lambda = [(1/k) - \sqrt{((1/k^2)-1)}]^2 \tag{1.4}$$

This expression relates the output electrical energy to the input mechanical energy and is only a function of the coupling coefficient. This relationship is the most significant for a piezoelectric generator because it illustrates the dependence of the coupling coefficient to the amount of energy that can be extracted. Now the efficiency ($\eta$) of the piezoelectric generator can be introduced below in equation 1.5, which is the ratio of the output electrical energy of the device to the mechanical energy the device consumes:

$$\eta = ½ * (k^2/(1-k^2)) / ((1/Q_m) +(½*(k^2 / (1-k^2))) \tag{1.5}$$

where $Q_m$ is the mechanical quality factor of the device. However, the mechanical quality factor is only used for vibration-based piezoelectric generators and from hereon it will be temporarily neglected to focus on optimizing the coupling coefficient, k.

As viewed from equation 1.4, increasing the coupling coefficient, k, increases both the output electrical energy and the efficiency. The most straightforward method to

increase the coupling coefficient is to use materials that have a large piezoelectric coefficient. The third-rank piezoelectric coefficient can be defined in equation 1.6 as:

$$d_{ikl} = x_{kl} / E_i \tag{1.6}$$

where $x_{kl}$ is the strain tensor and E is the electric field tensor (V/m). Most high-performance piezoelectric materials that possess a large piezoelectric coefficient and high coupling coefficient such as lead-zirconate-titanate (PZT, d=593pC/N, k=0.5) contain at least 60% lead, which is toxic. Although there have been concerted efforts to develop lead-free piezoelectric materials, no effective alternative has to date been identified. Very promising bulk binary systems of orthorhombic perovskite-type $(K_{0.5}Na_{0.5})NbO_3$ and hexagonal pseudo-ilmenite-type $LiTaO_3$ were fabricated with piezoelectric properties (d=416pC/N, k=0.6) near actuator-grade PZT5H[35]. Thin films of other similar inorganic piezoelectric materials such as potassium niobate ($KNbO_3$, d=175pC/N) and barium titanate ($BaTiO_3$, d=190pC/N, k=0.51) with high stiffness and strong piezoelectric activity in bulk poly-crystalline form have also been produced as thin as tens of microns. Unfortunately, thin films of such materials could not be synthesized directly on an AICD lead without melting or severely compromising the integrity of the plastic sheath. Moreover, ceramic structures comprised of such materials cannot be implemented as energy scavenging means into an AICD/BVP lead without heavy contributions to the lead stiffness. Furthermore, thin film ceramic structures undergoing cyclic loading are susceptible to cracking and fracture, which would short-circuit the device. Considering a lower-temperature synthesis could be employed or precipitation from a solution or vapor could produce a continuous thin film of such ferroelectrics, the films would still suffer from susceptibility to cracking and subsequent electrical short-circuit. Lastly and most

critically, even if such materials could be produced and/or transferred into an AICD lead, it would still take a large force to compress the material a small amount, especially in directions that the piezoceramics do not have much range of motion. Since energy is defined as force through distance, the effective energy generated through cardiac compression on one or several thin films would be exceedingly small, even with perfect conversion. Thus, such materials are unsuitable for incorporation into an AICD lead.

Alternatively, flexible piezoelectric polymers such as polyvinylideneflouride (PVDF, d=20pC/N, k=0.12) and composites of PVDF or rubber with PZT can be fabricated and bonded at low temperature using commercial adhesives. The permanent electrical polarization present in the ferroelectric β-phase of PVDF is due to the influence of highly electronegative fluorine on the polymer chain[36]. The β-phase (or piezoelectric phase) consists of parallel packing trans chains, which fit into an orthorhombic unit cell. The chain units $CH_2$-$CF_2$, deviate from a perfect planar zig-zag plane, which is responsible for the spontaneous alignment of the $CF_2$, and results in a permanent remnant polarization of the PVDF. The conformability of the material permits its integration into AICD leads without substantial contributions to lead stiffness. Furthermore, the high molecular weight of PVDF enables an excellent resistance to wear[37] and the material has also shown biocompatibility with tissue[17]. However, the main drawback of PVDF as an energy generator is its relatively low coupling coefficient (k<13%). In order to increase the piezoelectric activity of such a material, multiple layers stacked in parallel must be employed. Given the limited dimension (<1mm) of the interior of an AICD lead limits the number of layers that can be stacked. Therefore, in order to amplify the piezoelectric response without a significant increase in the dimension of the generator or load placed

on the RV, this work focused on raising the energy density by adding oriented arrays of piezoelectric nanowires to create a nanocomposite structure.

Piezoelectric composites, comprised of an organic (polymer) phase and an inorganic (nanowire or ceramic) phase, are very promising materials for energy harvesting because of their high coupling factors (k≈0.3-0.4), low acoustic impedance, and mechanical flexibility[38]. The geometry for two-phase (diphasic) composites can be classified according to dimensional connectivity of each phase; 0-0, 0-1, 0-2, 0-3, 1-1, 1-2, 1-3, 2-2, 2-3 and 3-3. Several composite structures that represent some of these connectivities are shown in Figure 1.5.

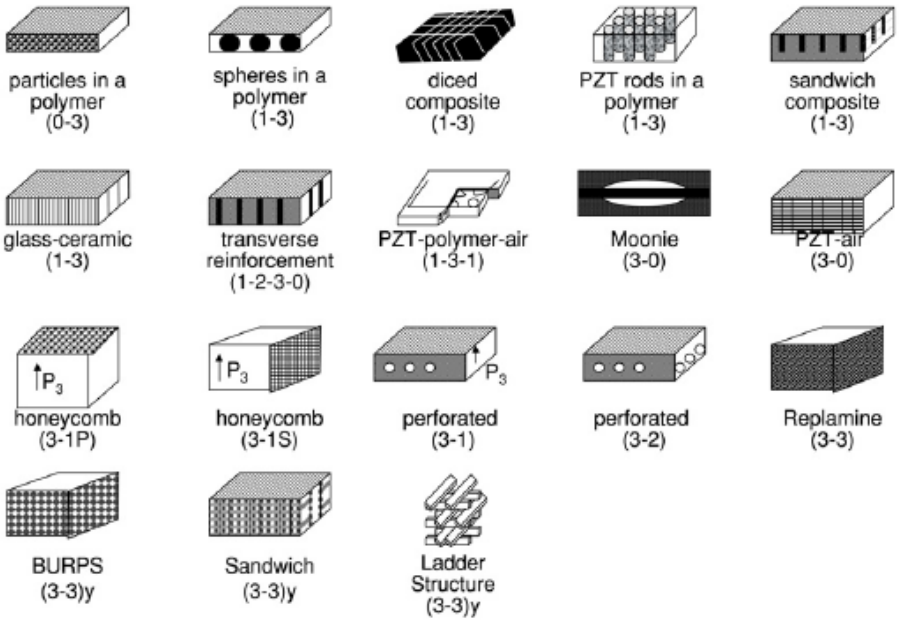


Figure 1.5: Schematics of several piezoelectric composite structures (Reproduced from [38]).

A 1-3 composite, such as the PZT rods in polymer shown in Figure 1.5, poses two key advantages over several of the other composite structures listed, 1) high electro-mechanical coupling (k) and 2) mechanical flexibility. Since the acoustic impedance is the square root of the product of the material's density and elastic stiffness, acoustic matching to cardiac tissue or blood can be accomplished by selecting organic phases with appropriate densities. Moreover, the thickness mode electromechanical coupling of the composite can exceed that of the organic phase and approach the magnitude of the coupling factor of the inorganic phase[39]. Figure 1.6 depicts the ideal case where all of the inorganic rod elements share the same electrode as the organic polymer phase.

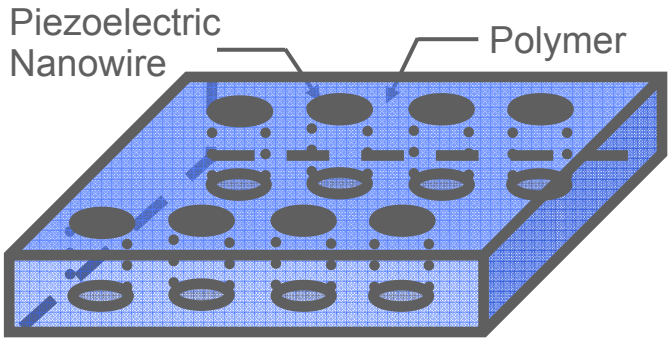


Figure 1.6: Schematic of a 1-3 piezoelectric nanowire: polymer composite. The top and bottom surfaces are metal electrodes.

In such a device, the top and bottom electrodes are common to all of the elements in the parallel configuration, which then requires the electric field to be the same to both the inorganic and organic phases. Since this is true, the displacement is a serial addition of both phases and written as:

$$D_3 = {}^1V^1K_{33}\varepsilon_o E_3 + {}^2V^2K_{33}\varepsilon_o E_3 \qquad (1.7)$$

where ${}^1V$ is the volume fraction of the inorganic element and ${}^2V$ is the volume fraction of the organic element, ${}^1K_{33}$ is the dielectric constant of the inorganic element and $E_3$ is the electric field. Also, given the strain experienced by both phases is the same, which can be written as equation 1.8:

$$ {}^1x_3 = {}^1d_{33}E_3 \tag{1.8a} $$

$$ {}^2x_3 = {}^2d_{33}E_3 \tag{1.8b} $$

the effective strain ($x_3$') of the system ($x_3' = {}^2x_3 = {}^1x_3$), can be written and solved for as below in equations 1.9a-b.

$$ ({}^1V * ({}^1x_3 - x_3') / {}^1s_{33}) = ({}^2V * (x_3' - {}^2x_3) / {}^2s_{33}) \tag{1.9a} $$

$$ x_3' = [ ({}^1V{}^2s_{33}{}^1d_{33} + {}^2V{}^1s_{33}{}^2d_{33}) / ({}^1V{}^2s_{33}{}^1 + {}^2V{}^1s_{33}) ] * E_3 \tag{1.9b} $$

The effective piezoelectric constant can be written as in equation 1.10:

$$ d_{33}' = [({}^1V{}^2s_{33}{}^1d_{33} + {}^2V{}^1s_{33}{}^2d_{33}) / ({}^1V{}^2s_{33}{}^1 + {}^2V{}^1s_{33})] \tag{1.10} $$

Equation 1.10 demonstrates the effective increase in piezoelectric coefficient achieved by merging the two phases into a composite material. In addition to the raise in piezoelectric coefficient, the strength and toughness properties of the inorganic stiff nanostructured materials are improved with a surrounding polymer matrix[40]. The polymeric material provides a path for efficient load transfer loading through and around the wires which in turn would allow for higher mechanical strains than on the individual inorganic nanowires. Moreover, the matrix would help to prevent a fracture in one area of the device from propagating to adjacent areas, thereby inhibiting macroscopic damage at larger strain values. Such a composite material satisfies the previous criterion of a piezoelectric structure designed to efficiently convert the kinetic motion of the heart into power for an implantable device (flexibility, high piezoelectric coefficient, multiple inputs, etc).

There are several advantages of using nanorods/wires over conventional bulk polycrystalline piezoelectrics for energy harvesting. The small size allows for better accommodation of strain without the initiation of fracture that can occur in bulk or micron-sized materials. This in turn enables more energy production per unit area through the direct piezoelectric effect. Another characteristic feature of nanostructures is their ability to buckle elastically, which makes them more mechanically tough. Additionally, piezoelectric nanostructures can be grown directly on flexible current collector substrates at relatively low temperatures (>80°C) with high densities. Since the nanowires can be grown directly on the current collector substrates, each can contribute to the capacity and provide numerous efficient pathways to generate energy. Moreover, single and highly-crystalline materials such as nanowires, generally have larger electro-mechanical coefficients than bulk polycrystalline counterparts due to the lack of defects and identical unit cell pattern and orientation throughout the material[33]. In the case of piezoelectric nanowires, which can be synthesized with near perfect domain alignment and with little to no grain boundaries, the crystallinity can facilitate more mobility in the domain walls and create even higher electro-mechanical coupling coefficients[41]. Thirdly and most critically, a nanowire array offers a potentially fail-safe technology because if one thousand or a million or more nanowires fracture, the generator will not short circuit and stop producing power as it would with a small number of planar inputs. Since there are a large number of active inputs that would be producing energy, the generator could theoretically last longer than macroscopic counterparts. Finally, the size reduction offers the potential to stack arrays on top of one another for three-dimensional architectures without significantly altering the overall dimensions or stiffness of the energy harvester.

## 1.5 PIEZOELECTRIC NANOWIRES

Nanowires are chemically synthesized single crystalline 1D nanomaterials with low defect density, and atomically smooth surface facets. The wide choice of nanowire materials brings a variety of unique functionalities that can impact numerous devices as well as new device architectures. Piezoelectric nanowires represent a class of nanowire that can be used for both efficient actuation and detection of mechanical motions. The generation of electrical charges from mechanical strains developed in piezoelectric nanowires also offers the potential to develop small-scale power generators.

The piezoelectric activity of individual nanowires has been studied where the mechanical excitation was induced by deflection of a single zinc oxide (ZnO) nanowire from a Pt-coated atomic force microscope (AFM) probe tip[42] and the resulted electric response was sensed through the probe tip. The output of the ZnO nanowire was $0.05 \times 10^{-15}$ J, in one discharge event. The piezoelectric response of a single barium titanate ($BaTiO_3$) nanowire has also been studied through a miniaturized flexure stage that applies a periodic tensile load[43] and an output 16 times higher than the ZnO nanowire was drained off into patterned contacts. Whether nanowire-based piezoelectrics can outperform their bulk counterparts is still unclear. Measurements of ensembles of nanowires actuated simultaneously and continuously need to be obtained, rather than at the single nanowire level, for incorporation into new, novel devices. In order to build a device incorporating piezoelectric nanowires that can each be accessed simultaneously, the nanowires must be grown with the same orientation or controllably placed directly into the device. Additionally, the device substrate on which the nanowires are grown and processed onto must be able to deflect with the heart's motion so as to remain innocuous.

## 1.6 SYNTHESIS OF NANOSTRUCTURES

The synthesis of one-dimensional nanostructures such as carbon nanotubes, semiconductor nanowires, metal-oxide and metallic nanowires have attracted wide attention since their inception. The high surface area architectures and potential quantum confinement effects have found use in a myriad of applications beyond piezoelectrics such as novel electronic devices[44], quantum computing[45], chemical and biological sensing[46], solar cells[47,48], thermoelectrics[49], nanolasers[50], photonics[51], and optoelectronics[52]. There are a variety of synthetic strategies that have been exploited to achieve 1D growth[53] and the most popular technique to produce nanostructures with controlled size, crystallinity and chemical composition has been through chemical vapor deposition (CVD). Of the various approaches that utilize CVD, the vapor-liquid-solid (VLS)[54] approach has been the most successful. VLS requires the diffusion of a gaseous reactant into nanometer-sized liquid droplets of a catalyst metal, immediately followed by the nucleation and growth of single-crystalline 1-D nanostructures (Fig 1.7). Various inorganic materials such as carbon nanotubes, classical semiconductors of silicon (Si) and germanium (Ge), III-V semiconductors of gallium arsenide (GaAs), gallium nitride (GaN), indium phosphide (InP), II-VI semiconductors of zinc selenide (ZnSe), cadmium telluride (CdTe), and metal-oxides of zinc oxide (ZnO), tin dioxide ($SnO_2$), have been produced with the VLS method. The high temperatures, expensive substrates and small growth chambers ultimately limit the VLS method from adoption into higher-production facilities and processing directly on organic substrates, which are necessary for energy scavenging devices from the heart.

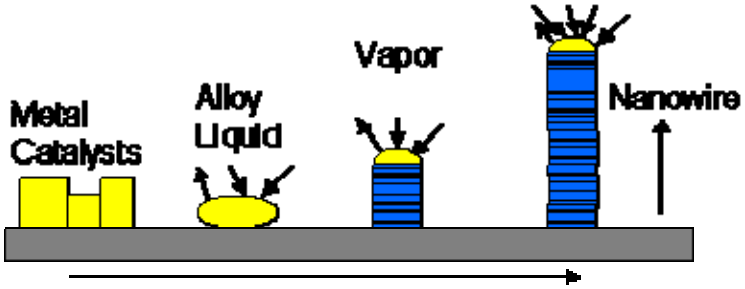


Figure 1.7: Vapor-Liquid-Solid (VLS) growth mechanism.

The solution-liquid-solid (SLS) approach was developed as an alternative to the VLS technique and offers more latitude for generating 1-D nanostructures in terms of throughput, cost and scaling to larger production volumes[55]. The basis of the SLS technique can be viewed from a controlled nucleation and growth process. The key to the hydrothermal process is the delivery and reaction of the precursors in solution rather than in the vapor phase (Fig. 1.8).

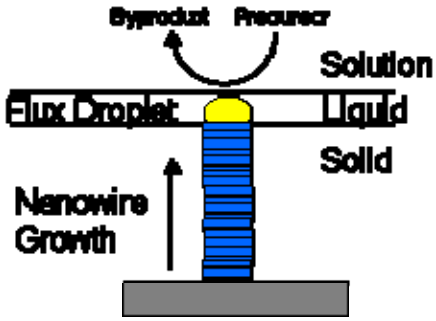


Figure 1.8: Idealized Diagram of Solution-Liquid-Solid Growth.

In this dissertation, we were interested in developing a synthetic strategy that could be used to reliably prepare highly oriented piezoelectric nanostructures onto plastic substrates. Several methodologies for growing oriented piezoelectric nanostructures of ZnO in solution have been created[56,57,58,59]. ZnO is a piezoelectric compound semiconductor with a wurtzite structure that is biocompatible and has a decent coupling

coefficient. If exposed to body fluids, ZnO nanowires have been shown to degrade into mineral ions in several hours[60]. Thus, our method of isolating nanowires by housing them inside pre-existing dead spaces of commercial AICD leads protects them from body fluids and subsequent degradation[21]. While other biocompatible nanowires with better piezoelectric properties than ZnO such as $BaTiO_3$[61] and $KNbO_3$[62] have been produced in solution, the temperatures needed for synthesis are beyond the thermal-degradation temperature of a flexible plastic substrate. Moreover, the necessary precursors for nanowire growth of such perovskite structures are toxic and the synthetic methods have failed produce an ordered array. Therefore, this dissertation concentrated on producing nanowire arrays comprised of ZnO with high orientation on plastic substrates and optimizing the piezoelectric properties.

The developed approach is based on a controlled nucleation and growth process. The synthetic platform avoids any processing or registry to individual nanowires and is able to produce arrays of ZnO nanowires with high densities ($>10^{10}$ per $cm^2$), large aspect ratios and high orientation directly on a device that can be integrated with an AICD lead. The details of the growth procedure are described further in chapter 2.

## 1.7 DEVICE DEVELOPMENT

Since the nanostructured generator is located inside a lead, the generator must be able to deform with the lead and not present additional resistance. This dissertation focused on creating active piezoelectric nanoelements on flexible organic substrates that could be interfaced with leads. Electronic systems on bendable supports have received increasing attention within recent years because of the applications that can be produced through them such as flexible displays, electronic textiles or wearable hardware, and

sensory skins for structural health monitoring[63]. While several innovative techniques have been developed to process nanomaterials from the growth substrate to a flexible support such as printing-type techniques, use of lithography and wet chemical etching[64], roll-printing[65], and transfer using adhesives such as elastomeric stamps[66], there are still issues such as yields. Other unique approaches such as flow-assisted assembly[67], blowing bubbles from suspensions of nanomaterials[68], and compilation through a Langmuir-Blodgett[69] trough continue to improve the assembly of micro and nano building blocks in a parallel, scalable, and highly reproducible manner, independent of the specific materials. However, for some bendable systems instead of following the "bottom-up" synthesis first, assembly and "top-down" fabrication next, it is desirable to grow micro and nanostructures into the device architecture. Herein a plastic-based device was batch fabricated and highly oriented, crystalline ZnO nanowires were grown directly onto it; combining the growth and assembly of nanowires into one step. Since the substrate is plastic, it is bendable and can be rolled into a cylindrical or spiral shape inside an AICD lead. The devices were integrated to a testing apparatus that consisted of an optically monitored loading platform connected to two pre-amplifiers to sense the current and voltage outputs. The loading stage consisted of two parts: (1) a curved rigid strut attached firmly to a moveable stage to provide the approximate bending radius actuation felt during systole within an AICD lead, and (2) a grounded test sample mounted perpendicular to the loading stage. A sensor within the stage and CCD camera monitor the displacement of the stage. Voltage and current outputs of the generator were recorded on an oscilloscope coupled to the amplifiers. Chapter 3 further details the construction and testing of the nanostructured generator.

## 1.8 OPTIMIZATION OF GENERATOR FOR ENHANCED RESPONSE AND LIFETIME

Ultimately, piezoelectricity at any scale is an intrinsic material property that is extremely sensitive to crystallinity, polarization, material-electrode interface, strain condition, surface chemistry, and surface roughness. In low dimensional materials such as nanowires, the impact of one of the aforementioned factors is enhanced due to the miniaturization. The approach to optimizing the nanoscale piezoelectric structures here concentrated on three levels: 1) at the material level, by synthesizing the strongest piezoelectric compound that is currently amenable to oriented growth on plastic; 2) at the geometric level, by precisely controlling the size of the nanowire and nature of deformation to maximize the effective piezoelectric response, and 3) at the interface level, by changing the surface landscape of the nanowire with different molecules to affect the resistivity and piezoelectric coefficient[70] and change the size of the electronic contact between the metal and nanowires.

The first optimization thrust focused on building an electro-mechanical model of a single nanowire during systole to investigate the influence of geometrical properties on the piezoelectric response. Using analysis of X-Ray images of a lead in systole, the approximate the force a nanowire would experience inside an AICD lead was determined. The force was then translated into an experienced strain and the influence of the nanowire aspect ratio on the strain was also calculated. The strain was then converted into a pseudo-strain rate by coupling the frequency of loading and unloading of the nanowire (1Hz for a heartbeat) and the current output was then derived. From the model output, insight was gained as to how to structure the nanowire array to boost the energy production. With the latitude of the synthetic technique, the reaction conditions were

optimized to produce nanowires that would return the highest power output. The model and conclusions are described further in chapter 3.

Next, as an effort to improve the output and create a longer device lifetime, the bottom electrode/metal film was buckled as it was deposited onto the substrate. The stiff thin electrode on a soft support is similar to that of animal skin, where a stiff epidermis is rigidly attached to a soft dermis[71]. The hierarchical pattern of micro-buckles changes their shape from 'wrinkled' waves to a flat surface during the cardiac cycle. The details of the procedure are also outlined further in chapter 3.

Commercial piezoelectric polymeric films were also tested as a comparison to the energy production of the nanowire device. The films were actuated by a system driven to accurately simulate the motion of a failing human RV and a simple integrated circuit to collect the generated charge was also developed. The results demonstrate the need for development of advanced piezoelectrics for energy harvesting from the RV and are reported in more detail in chapter 3.

## 1.9 DEVELOPMENT OF SINGLE NANOWIRE PHOTOELECTRON SPECTROSCOPY TOOL

The last optimization thrust involved passivating the nanowires with organic molecules to change the barrier height of the Schottky contact and resistivity of the material. Before testing the piezoelectric effects of molecular-augmented nanowires, experiments were first conducted to study the effect of the molecules on single nanowire properties. A novel low photon energy photoelectron spectroscopy tool was developed to measure individual nanowire properties that dominate transport across the interface and piezoelectric response, namely the effective work function. Native nanowires were first

probed and then the nanowire surface was perturbed to highlight the influence of several adsorbate molecules on the measured properties. The changes in the electronic structure of the measured nanowires were correlated to adsorption and desorption dynamic events. The photoemission technique was then coupled to synthetic studies of various self assembled monolayers (SAMs) of phosphonic acids with different dipole moments adsorbed onto the nanowire surfaces to test their respected influences on the nanowire properties. For the first time, quantitative measurements of changes in the work function of molecular modified nanowires were measured. The molecule-induced modification of the nanowire electronic properties measured here provides an effective platform to study how other molecular adsorption events will affect the energy output of nanowire-based energy generators. The design, development, testing and results of the photoemission experiment are explained in further detail in chapter 4. Conclusions and future work are reported in Chapter 5.

# Chapter 2 - Optimized Synthesis of Piezoelectric Nanostructures on Plastics

This chapter details the production of highly ordered nanowire (NW) arrays comprised of zinc oxide (ZnO) on flexible plastic substrates. The ZnO nanowires were grown using a two-step 'wet' strategy, whereby each step was systematically optimized. In the first step, substrate surfaces were prepared with ZnO nanocrystals of various shapes and sizes. In the second step, oriented nanowire growth from the catalyst seeds was accomplished in a diluted aqueous solution at low temperature. By separating the nanoparticle film nucleation and oriented growth into two separate steps, the architecture of the nanowire array could be controlled. Ensembles of the nanowire arrays were characterized using Scanning Electron Microscopy, X-Ray Diffraction, and Energy-Dispersive Spectroscopy. Individual nanowires were characterized using Transmission Electron Microscopy, Selected Area Electron Diffraction and Low Energy Photoelectron Spectroscopy (chapter 4).

ZnO is a nontoxic *n*-type semiconductor that can be grown as crystalline nanowire arrays in a variety of facile conditions[72]. The developed approaches for growing oriented nanostructures of ZnO in solution are all based on a controlled nucleation and growth process. According to the fundamental theory of nucleation and growth, the free energy of forming stable nuclei on a substrate can be roughly controlled by four factors according to the equation:

$$\Delta G = -RT*\ln S + \sigma_{p\text{-}l} + (\sigma_{p\text{-}s} - \sigma_{s\text{-}l}) * A_{p\text{-}s} \qquad (2.1)$$

where 'S' is the degree of supersaturation, '$\sigma_{p-l}$' is the interfacial energy between the particle (p) and the liquid (l), '$\sigma_{p-s}$' is the interfacial energy between the particle and the substrate (s), '$\sigma_{s-l}$' is the interfacial energy between the substrate and the liquid '$\sigma_{s-l}$', and $A_{p-s}$ is the surface area of the particle. If the number of nuclei (N) is plotted as a function of the degree of supersaturation, a window where nucleation is favoured for oriented nanostructures can be seen (Fig. 2.1).

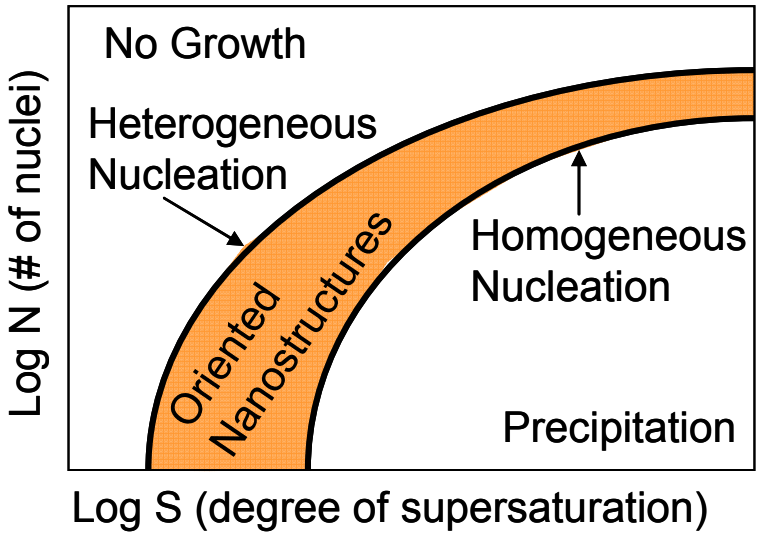


Figure 2.1: Diagram of Nucleation and Growth (adapted from [72]).

Usually, oriented nanostructures are difficult to grow in solution because most syntheses are conducted at high precursor concentrations where massive precipitation dominates the reaction. Using equation 1 and figure 2.1, a comprehensive synthetic method was designed and relied on the following factors:

1) The narrow window of the diagram dictates that the precursor concentration must be sufficiently high to ensure nucleation and growth can occur but low enough to limit the degree of precipitation. In order to restrain the degree of supersaturation,

the precursor concentration was kept low and the reaction temperature was reduced as much as possible.

2) In order to ensure nucleation is favoured on the substrate rather than in solution, the surface was functionalized. Surface functionalization has been a widely adopted method to decrease the interfacial energy between the substrate and the particle and readily presents an efficient technique to aid in oriented growth. The functionalization also enabled a degree of latitude to separately form stable nuclei and deposit them on the substrate. Accordingly, various nuclei were produced in separate reactions and deposited onto a substrate to gauge which produced the best nanowire array.

3) The orientation of nanostructures grown on substrates in solution can be achieved through several techniques. First, the crystal structure of the as-grown nanowire must permit anisotropic growth. For ZnO, the thermodynamically stable crystal structure is hexagonal wurtzite (6*mm*), which can be viewed as hexagonal close packing of oxygen and zinc atoms in space group $P6_3mc$ with the zinc atoms in tetrahedral sites (point group 3m). The occupancy of four of the eight tetrahedral sites of the hexagonal lattice controls the structure, with a hexagonal wurtzite ZnO crystal exhibiting a basal polar oxygen plane $(000\bar{1})$, a top tetrahedron corner-exposed polar zinc face (0001) and six low index nonpolar faces $\{10\bar{1}0\}$ parallel to the c-axis (Figure 2.2). Since the polar faces are metastable and the nonpolar faces are very stable, an inherent asymmetry exists along the c-axis, which allows for anisotropic growth of the crystal along the [0001] direction.

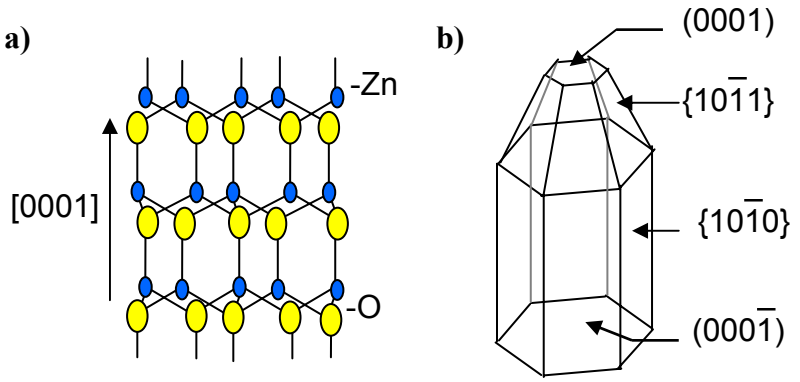


Figure 2.2: Structural model of ZnO. a) Schematic of ZnO crystal structure along polar axis. b) Schematic of crystal faces of wurtzite ZnO.

4) Next, the kinetic growth of the nanostructures must be augmented so oriented structures grow rather than non-oriented structures. Oriented growth can be achieved through the addition of organic growth factors that regulate the growth and orientation of specific crystalline planes. Growth factors that selectively bind to the nonpolar {10$\bar{1}$0} crystal faces and inhibit radial growth permit an effective medium to tweak the aspect ratio of the nanostructure as well as shape its orientation. An additional technique to encourage orientation is through 'competitive growth,' whereby neighbouring growing crystals impede unaligned growth and only allow oriented nanowires to grow. The orientation of the growing nanostructures can also be influenced by the manner in which the catalyst seed lays on the substrate. A combination of these techniques was employed, textured nuclei were first formed in situ on a substrate to promote growth along the c-axis and an amine-rich polymer (low molecular-weight polyethylenimine) was introduced to the solution to impede radial growth of the nanowires.

Utilizing the guidelines above, a synthetic strategy for growing piezoelectric nanowires of ZnO with high orientation on plastic substrates was developed. The synthetic platform is able to produce dense, ($>10^{10}$ per $cm^2$) ordered arrays of highly crystalline nanowires directly on a variety of flexible organic substrates.

## 2.1 OPTIMIZED SYNTHESIS OF PIEZOELECTRIC NANOSTRUCTURES

Size and shape provide important control over many of the physical and chemical properties of nanoscale materials. As such, one of the critical aspects of this research was to develop a robust method to reproducibly create highly oriented piezoelectric nanowires with large aspect ratios on flexible substrates. While there are several approaches to synthesize crystalline nanowires such as metal-organic chemical vapor deposition[73] and chemical vapor transport[74], these processes require elevated temperatures (450-900°C), which would melt an organic or flexible substrate. In contrast, hydrothermal approaches utilizing the solution-liquid-solid (SLS) technique described in Chapter 1 offer lower growth temperatures (<350°C) as well as potential to scaling to larger production volumes. Herein the SLS method was utilized for growing aligned 1-D nanowires on a series of flexible devices.

The process began with the preparation of nanocrystals (NCs) with various morphologies to serve as nucleation sites. The NCs are either deposited or formed in-situ on a patterned substrate and immersed in an aqueous solution to grow highly oriented nanowires. The highly crystalline nanowires are characterized and growth conditions are optimized to produce epitaxial growth with aspect ratios above 75.

## 2.2 ZnO NANOCRYSTAL SYNTHESIS

In contrast to particles with amorphous or polycrystalline morphology, NCs allow exploitation of the inherent crystal anisotropy to precisely engineer NC shape. The ability to control particle morphology was an important objective for the optimized synthesis of oriented nanowires, as the size, structure and orientation of the NC seed can directly determine the size and orientation of the nanowire[75]. The NC shape can in turn be used as a powerful tool to engineer the size and orientation of the nanowire growing from it.

The hydrolysis of zinc salts has been an effective route to form ZnO colloids and NCs with different shapes[76,77,78,79,80]. Several of these approaches were used to build catalyst seeds of ZnO with various sizes and morphologies such as spheres, prisms, quasi-spherical platelets and c-axis textured platelets.

### 2.2.1 SPHERICAL ZnO NANOPARTICLE SYNTHESIS

The first step in the optimized synthesis began with the preparation of spherical nanoparticles. ZnO spherical nanoparticles were synthesized by addition of a precursor: zinc acetate dihydrate ($ZnAc_2 \cdot 2H_2O$), capping agent: oleic acid (1:1 ratio) and solvent: (1-octadecene (OD)). The mixture was stirred and heated to 180°C and then degassed for 1 hour to remove any water from the system. The solution was then heated again under nitrogen to 300°C and when the solution turned cloudy or whitish, the nanocrystals were formed. After which, the solution was subsequently cooled to room temperature and the nanocrystals were centrifuged, washed repeatedly and redispersed in hexane. Since OD is not a coordinating solvent, no single crystal plane was favored, leading to a spherical shape[81]. Interestingly, the polarity of the solvent was found to have a significant influence

on the morphology of the resulting NC, which will be discussed further in the chapter. Figure 2.3a shows a representative transmission electron microscope image of the spherical nanoparticles dropped onto a 400 mesh lacey carbon grid and figure 2.3b shows the Energy Dispersive X-ray Spectroscopy (EDX) of the ZnO nanoparticles. The oxygen peak at 0.53 keV and zinc peaks at 1.01, 8.63, and 9.58 keV correspond to pure zinc oxide.

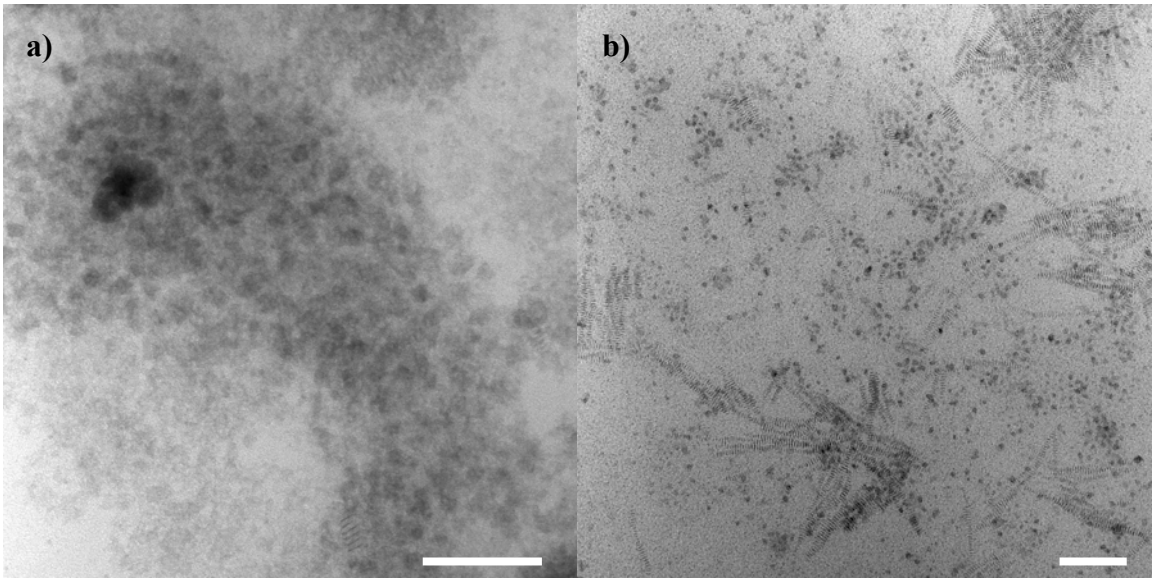


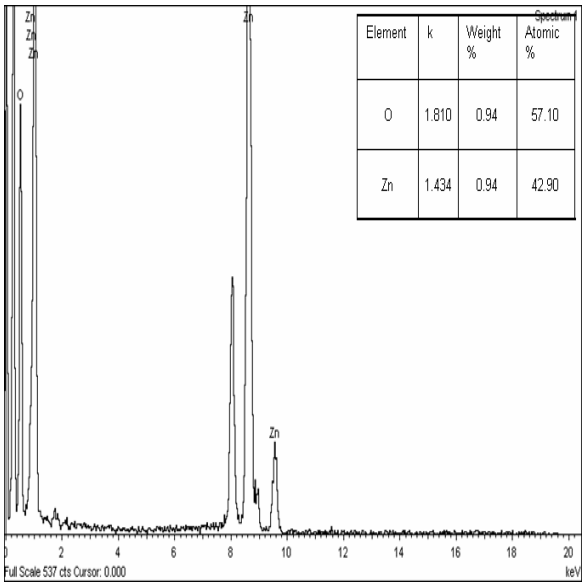

Figure 2.3: Spherical ZnO nanoparticles. a) TEM images of spherical ZnO nanoparticles. Nanoparticles are average size of 25-30nm in diameter. Scale bar is 100nm for both a) and b). c) EDX of ZnO nanoparticles depicting only traces of Zn and O.

### 2.2.2 QUASI-SPHERICAL ZnO NANOPLATELETS SYNTHESIS

In order to increase the surface area of the particle ($A_{p\text{-}s}$) and decrease the energy barrier between the particle and substrate ($\sigma_{p\text{-}s}$), quasi-spherical nanoplatelets were created. Quasi-spherical nanoplatelets offer higher surface to volume ratios than spherical particles and can create very favorable surface energies for epitaxial growth by maximizing their area ($A_{p\text{-}s}$) with the substrate and minimizing their thickness. ZnO quasi-spherical nanoplatelets were prepared from zinc acetate dihydrate in alcoholic solution under basic conditions. A solution of sodium hydroxide (NaOH) (0.03M) in methanol was slowly added to a solution of zinc acetate dihydrate (0.01M) in methanol at 60°C and stirred for approximately two hours[79]. Figures 2.4a-d shows several representative TEM images of the quasi-spherical nanoplatelets dropped onto a 400 mesh lacey carbon grid. An assembly of quasispherical nanoplatelets, which are partially agglomerated owing to the absence of surface-stabilizing ligands, is shown in Figures 2.4a-d. A TEM image of apparent single-crystalline particles is displayed in Figure 2.4b, where the nanoplatelets have a mean diameter of 6 nm (Fig 2.4b), and lattice fringes can be delineated.

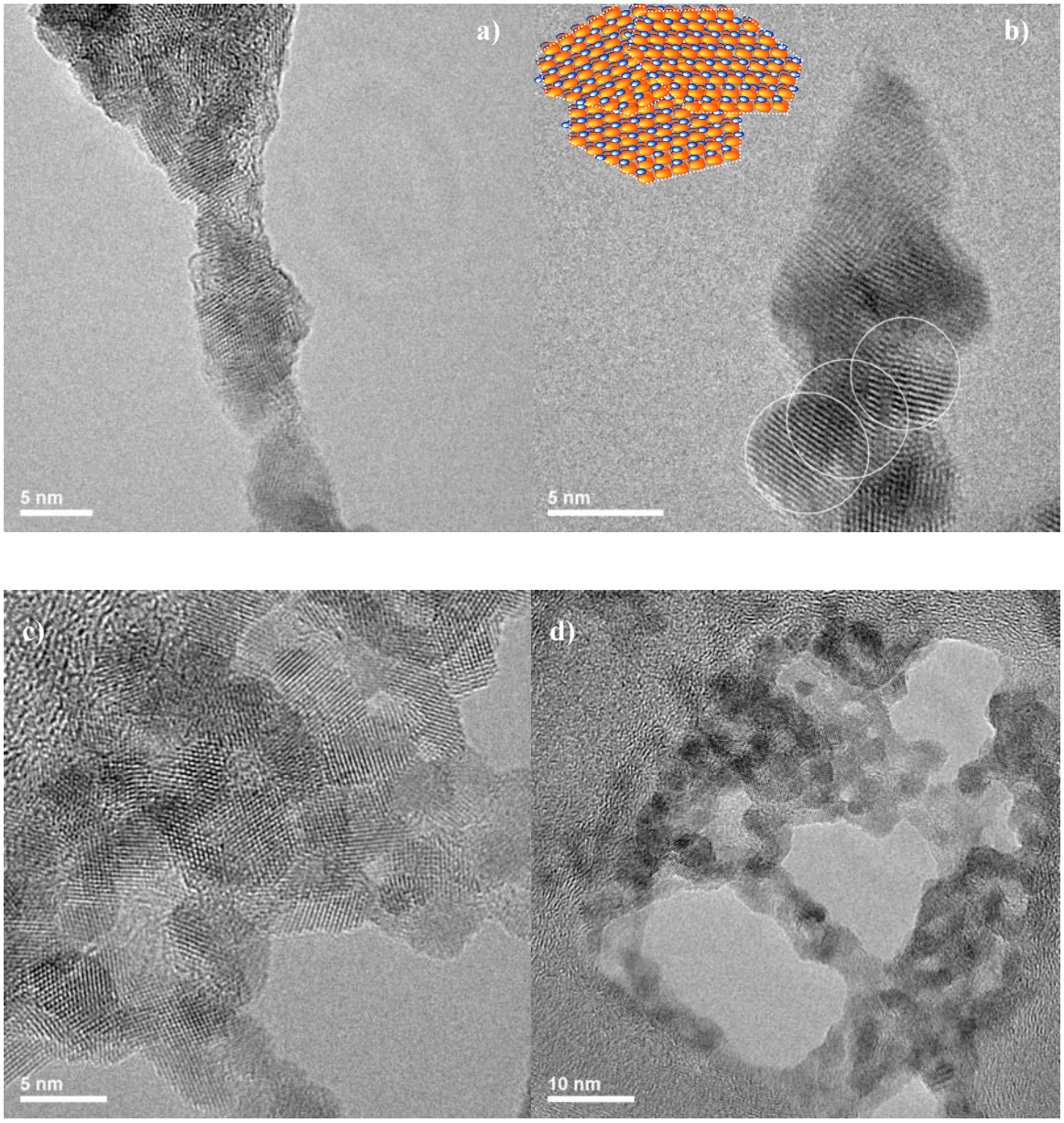
a)
b)
5 nm
5 nm
c)
d)
5 nm
10 nm

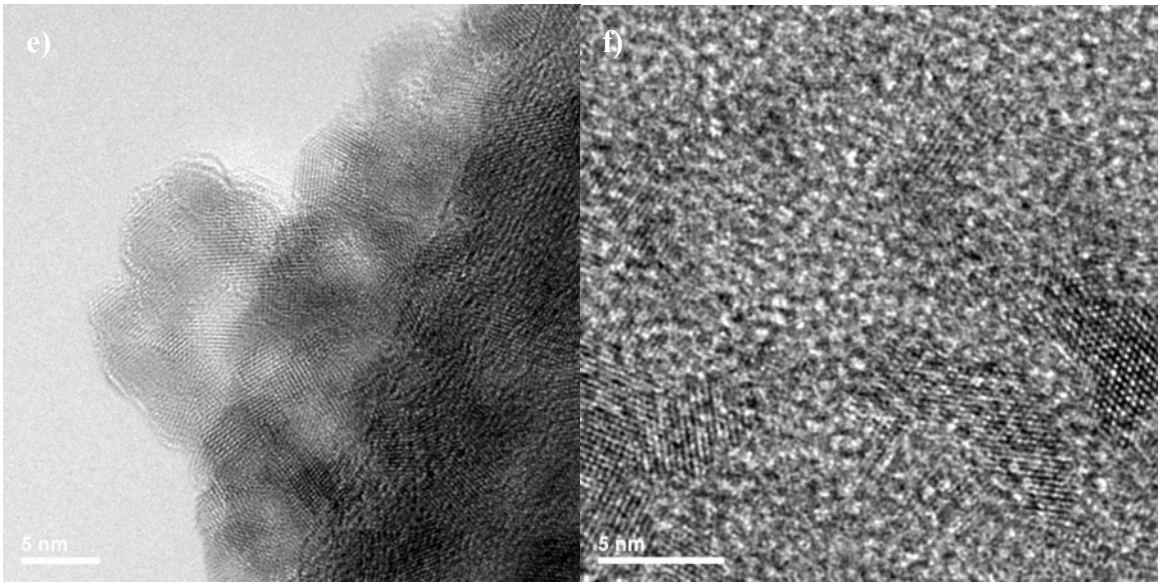


Figure 2.4: Quasi-spherical ZnO nanoplatelets. a) TEM image of quasi-spherical ZnO nanoparticles. Nanoparticles are average size of 5-8nm in diameter. a) Far-field view of quasi-spherical nanoplatelets, b) Magnified view of nanoplatelets. Lattice fringes can be delineated on circled nanoplatelets indicating highly crystalline structures. Inset is schematic of assembled nanoplatelets stacking on top of one another like a 'pancake stack'. c) Aggregated nanoplatelets stacked on top of each other at edge of grid. d) Far-field view of quasi-spherical nanoplatelets. e) High-resolution TEM (HRTEM) of crystalline nanoplatelets aggregated on top of another. f) HRTEM image of isolated nanoplatelets showing diameter of 5nm.

### 2.2.3 TRIANGULAR ZnO NANOPRISM SYNTHESIS

One of the limitations the quasi-spherical nanoplatelets suffered from was heavy agglomeration. Since no capping ligand was employed, the thin platelets would often assemble into "pancake stacks" (Fig. 2.4b inset), which would form large nucleation sites for thicker or multiple wires to stem from. To improve the dispersity of the nanocrystals and maintain the interfacial energy ($\sigma_{p\text{-}s}$) with a high surface area, triangular nanopyramids were created[80]. The pyramidal shape offered a better tendency to self-assemble than the nanoplatelet geometry and still maintained a high surface to volume

ratio. Moreover, maximization of the nanoparticle packing density could be achieved by creating more concentrated solutions.

ZnO triangular nanoprisms were synthesized in a similar fashion to the spherical particles but OD was substituted with a different coordinating solvent, 1-hexadecanol (HD). Since the coordinating nature of the solvent was relatively mild, HD functioned as a weak ligand in this synthesis. The HD in combination with the capping ligand oleic acid, gave rise to the faceting of the nanotriangle. Figures 2.5a-d are representative TEM images of the triangular nanoprisms dropped onto a 400 mesh lacey carbon grid. The inset to Figure 2.5d shows the corresponding representative model of the triangular nanoprism.

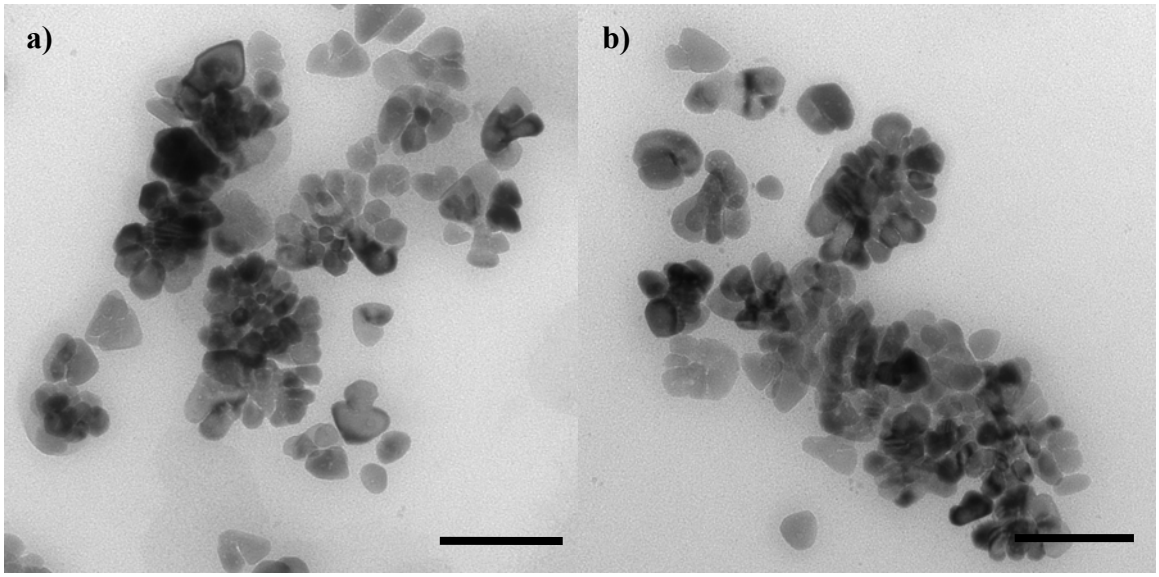

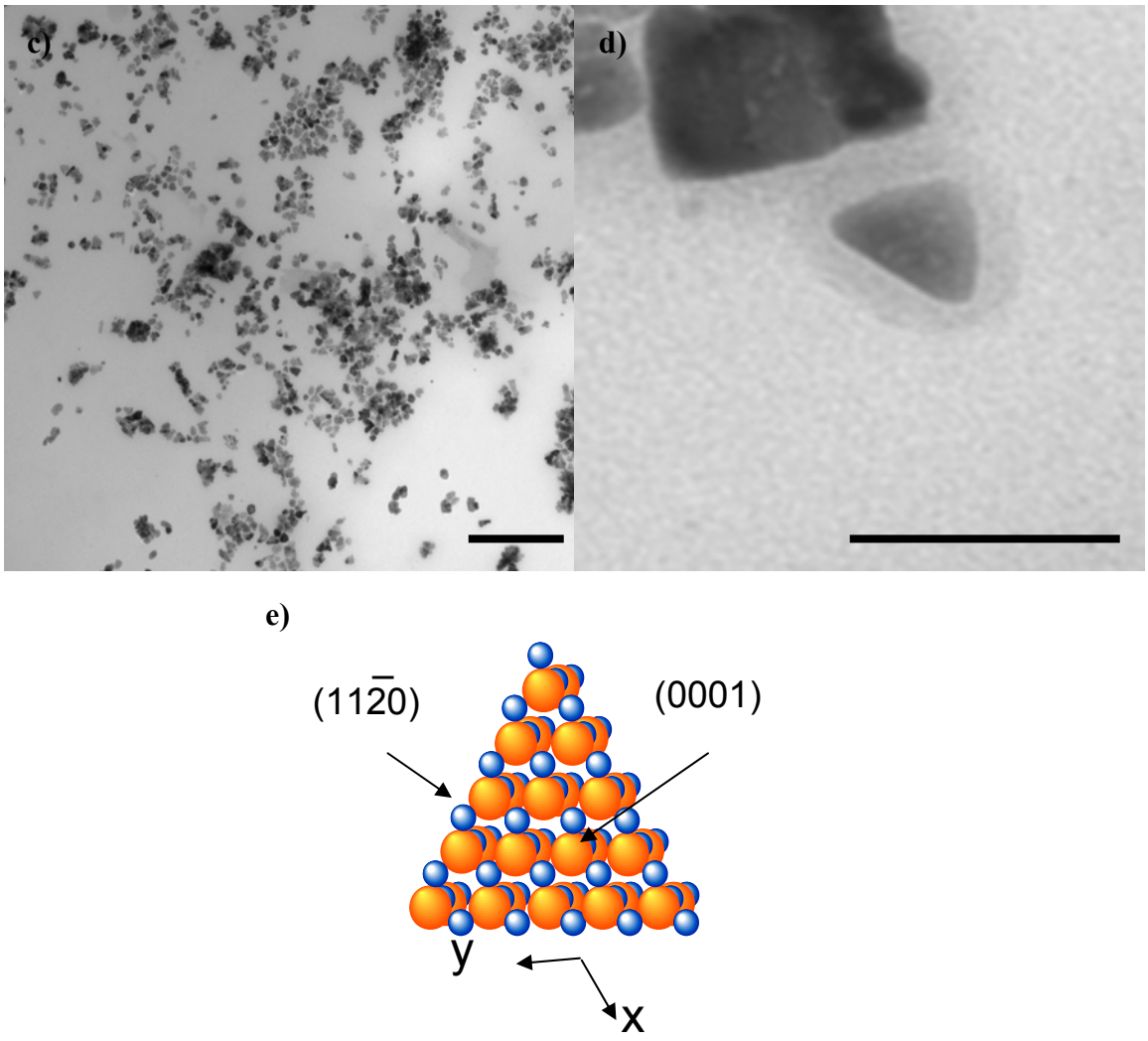


Figure 2.5: Triangular nanoprisms of ZnO. a) TEM image of triangular ZnO nanoprisms. Nanoprisms range in size between 25-40nm in area. b) TEM image of pyramidal nanocrystals packed into near monolayer. c) Far-field TEM image of ZnO triangular nanoprisms showing monodisperse over broad range. d) Magnified TEM image of triangular nanoprism showing well defined facets. The scale bar in each image is 100nm. e) Schematic of triangular nanoprism.

### 2.2.4 'C-AXIS' TEXTURED ZnO NANOPLATELET SYNTHESIS

Owing to their larger size, triangular nanoprisms would stem larger diameter nanowires which would consequently reduce their aspect ratios. The larger seed would also stem multiple wires from the same seed that would grow at various angles rather than perpendicular to the substrate. Since the aspect ratio of a piezoelectric nanowire directly influences the amount of energy that can be extracted using the direct piezoelectric effect, smaller diameter nanowires and larger aspect ratios were sought. To improve both the seed size and its morphology, c-axis textured nuclei were prepared in situ on a flexible substrate. By preparing the catalyst seeds directly on the substrate, a natural electrical junction with the substrate can be formed if the substrate was coated with an electrode. Moreover, seed agglomeration from deposition was circumvented as the formed seeds are created in situ. C-axis textured nuclei were created with their (0001) planes perpendicular to the substrate by thermally decomposing zinc acetate dihydrate directly on the substrate. While the exact mechanism of seed formation and alignment are not adequately understood yet, several arguments have been proposed of which only one will be discussed here. Since the {0001} surface energy depends on thickness, very thin isolated crystals adopt a (0001) morphology, which would then kinetically lock-in growth of that orientation as the crystal continues to grow[56].

To create c-axis textured nuclei, the substrate was first coated with zinc acetate dihydrate crystallites (0.005M) dissolved in ethanol and rinsed with a solution of 95% ethanol and 5% (v/v) deionized water. The small fraction of water is necessary to hydrolyze the products in the seed layer that are insoluble to a pure ethanol rinse[82]. The clean ethanol/water wash is to remove any undissolved zinc acetate crystallites from the surface. The wash may also help to provide a monolayer or several monolayers thick

zinc acetate layer by removing any impurities that have been deposited on the surface. To make sure the crystallite solution was well mixed and the crystallites were dissolved, the solution was ultra-sonicated until optically clear or for roughly fifteen minutes. If the solution became cloudy during sonication, zinc hydroxide was assumed to form and the solution was discarded. Once the crystallite solution was deposited, the surface was viewed under an optical microscope to see if large impurities (i.e. aggregates or large chunks) had been deposited or sometimes bare spots, which also occurred from a cloudy solution. If the surface still looked relatively clean, it was then blown dry with nitrogen and the process was repeated again four more times to ensure complete coverage. The substrate was then annealed at 200°C in air for twenty minutes. The tempering of the crystallites yielded individual ZnO islands with their (0001) planes parallel to the substrate. The c-axis alignment of the acetate-derived ZnO seeds is not sufficiently understood at this point but several arguments for the texturing have been proposed. First, the polar {0001} faces of wurtzite ZnO are electrostatically unstable Tasker type III surfaces, which can be stabilized by (i) surface reconstruction or faceting, (ii) charge transfer between surfaces (electronic relaxation) or (iii) surface nonstoichiometry. If surface reconstruction was solely responsible for alignment, the molecules present during the decomposition of zinc acetate (primarily hydroxyl groups) would adsorb onto the growing {0001} surfaces and stabilize them relative to the nonpolar {1010} and {1120} faces. Since none of the crystal surfaces reconstruct to stabilize an individual surface first[83], the adsorbed molecules may neutralize surface charge. However, surface-sensitive spectroscopic findings show no evidence for substantial charge transfer on ZnO {0001} faces.[84] STM has shown clean (0001)-Zn faces roughen over two layers to stabilize themselves by nonstoichiometry but the (0001)-O facet is flat and stoichiometric. The texturing could be an intrinsic thermodynamic feature of the growth of ZnO crystals.

Since ZnO lacks cubic symmetry, there is an anisotropy that permits growth along the c-axis, making it the fastest growth direction. Since the {0001} surface energy depends on thickness, thin crystals could adopt the {0001} orientation, which is kinetically locked-in as the growth extends. A schematic of the nanocrystal is displayed in (Fig. 2.6a). The c-axis texturing was confirmed through x-ray diffraction (XRD), where the textured seeds show only an enhanced (0002) reflection, indicating their c-axis is perpendicular to the substrate (Fig. 2.6a).

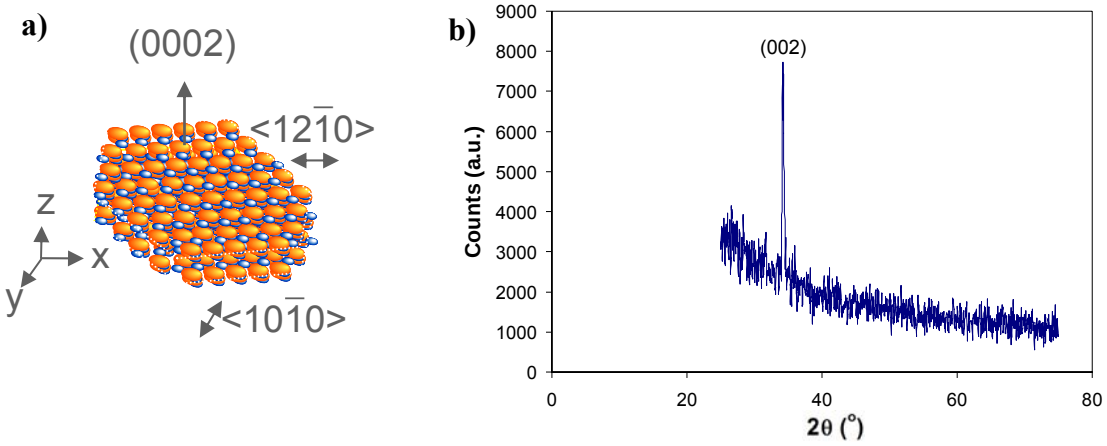


Figure 2.6: 'C-axis' textured ZnO nanoplatelets. a) Schematic of textured nanoplatelet with (0001) plane aligned perpendicular to the substrate. b) X-ray Diffraction of textured ZnO seeds.

Once the seed layer is formed, oriented growth of the nanostructured crystal follows in a second separate step. The fundamental advantage of seeded growth is the enhanced control imparted by separating nanowire nucleation and oriented growth into two steps. In each step, the experimental conditions can be optimized to control the size, orientation and population density. Further extension of the optimization may lead to further enhancements of the energy generator.

## 2.3 HYDROTHERMAL ZnO NANOWIRE GROWTH

Using the structural metastability of ZnO and creating a precipitation and aging medium that can coordinate to the (0001) face of hexagonal wurtzite ZnO, which contains a corner of the coordination tetrahedron of $Zn–O_4^{-6}$ and can interact strongly with solvated Zn species, an oriented array of 1-D ZnO can be grown. In aqueous solution, zinc(II) is solvated by $H_2O$, giving rise to aquo ions. In diluted solutions, zinc(II) can exist as several stable monomeric hydroxyl species that depend on the pH and temperature of the solution[85]. The aquo ions can include $ZnOH^+(aq)$, $Zn\text{-}(OH)_2(aq)$, $Zn(OH)_2(s)$, $Zn(OH)_3^-(aq)$, and $Zn(OH)_4^{2-}(aq)$. Solid ZnO nuclei are formed by the dehydration of these various hydroxyl species and can continue to grow by the condensation of the surface hydroxyl groups with zinc hydroxyl complexes[86].

Basic conditions are normally used to grow 1-D ZnO crystals because divalent metal ions do not readily hydrolyze in acidic media. In basic environments, additives that can coordinate to the solvated zinc complexes and help promote one-dimensional growth need to be added to the solution. One of the more studied additives is hexamethylenetetramine (HMTA), which is a biocompatible nonionic cyclic tertiary amine that can act as a Lewis base to metal ions when hydrolyzed. Though its exact role is still controversial, it is believed HMTA acts as a pH buffer by slowly decomposing to provide a gradual and controlled supply of ammonia[59], which can form ammonium hydroxide and complex zinc(II) to form $Zn(NH_3)_4^{2+}$. Since zinc hydroxide intermediates dictate the growth of ZnO, the gradual hydroxide release can control the available zinc(II) species in solution by coordinating to the available complex and keeping the free zinc ion concentration low. The Zn precursor, Zinc Nitrate Hexahydrate (ZnNH, $Zn(NO_3)_2{\cdot}2H_2O$)

thermally decomposes and gives a steady supply of zinc(II) species. Both HMTA and ZnNH can permit anisotropic crystal growth until the rods/wires eventually begin to coalesce and form a thin film. Reducing the concentration of the reactants can effectively reduce the diameter of the nanowires to prevent fusing but a reduction in length is also seen[87]. To obtain nanowires with high aspect ratios (>50) and prevent the nanowires from forming into a thin film, an additional molecule can be introduced which prohibits radial growth but permits axial growth. Several organic molecules such as citrates[88], amines[47] and diblock copolymers[89] can alter the surface chemistry of a growing rod/wire in solution by selectively adsorbing onto specific surfaces to promote or inhibit the growth of crystalline planes. Low molecular weight polyethylenimine (PEI), a cationic polyelectrolyte rich in amine groups, was used to selectively bind to the nonpolar $\{10\bar{1}0\}$ crystal faces and inhibit radial growth and raise the aspect ratio of the nanowires above 75.

Vertical nanowire arrays were grown hydrothermally from each type of ZnO nuclei in diluted aqueous solution of ZnNH (0.025M), HMTA (0.025M) and branched low-molecular weight PEI (0.005M) for 36 hours. The preformed nuclei were dip-coated onto a pre-cleaned Cr/Au-coated polyester or polyimide substrate 3-4x, heated to 100°C for ten minutes and suspended upside down in the growth solution at 90°C. Each growth solution was identical in precursor concentration, temperature, and pH to ensure the resulting nanowire array was solely influenced by the catalyst seeds. Further optimization of the solution conditions will be discussed later in the chapter. After removal from the growth solution, the nanowire arrays were rinsed thoroughly with deionized water several times, dried with a nitrogen gun, cleaned with UV/Ozone for 30 minutes to remove any residual organics and baked in vacuum at 120°C overnight. Figure 2.7 shows nanowire

arrays grown from each type of catalyst seed (schematic inset). Nanowires grown from the spherical nanoparticles were sparsely located on the substrate indicating a low density of nucleation sites (Figure 2.7a). A more concentrated solution of particles was used to raise the population density of the nanowire arrays, but the diameter of the resulting nanowires increased and the alignment of the nanowires was still poor (Figure 2.7b). To improve the orientation of the nanowire array, smaller quasi-spherical nanoplatelets with higher surface to volume ratios were used. Figure 2.7c shows a representative SEM image of nanowires grown from the quasi-spherical nanoplatelets. The nanowires are smaller in diameter owing to the smaller seeds, and denser than the arrays grown from the spherical catalysts owing to more nucleation sites from the more densely packed seeds. However, since no capping ligand was used for the nanoplatelets, the seeds tended to aggregate and form large nucleation sites, which would stem multiple nanowires that would grow at various angles (Fig 2.7d). To abate the effect of multiple wires stemming from a large group of nuclei, triangular nanoprisms capped with oleic acid were used. Figures 2.7e-f show representative SEM images of nanowire arrays grown from these isolated nuclei. The arrays are as dense as the quasi-spherical nanoplatelet derived nanowire array but with higher orientation. We confirmed the orientation using XRD (Figure 2.7g) and retrieved lattice constants for hexagonal wurtzite ZnO (a=3.249 Å, c=5.205Å) with a slightly enhanced (002) reflection. However, the strong presence of the other peaks indicates the nanowires still grow at various angles. As the unaligned crystals continued to grow along their favored crystal planes, the crystals growing aligned to the substrate are soon intersected by the growing unaligned neighboring crystals and eventually fuse or undergo 'Ostwald ripening', forming a larger diameter single nanowire. This effect explains why the nanowires grown from triangular nanoprisms were larger in diameter. The increased diameter would reduce the aspect ratio and in turn

amount of energy that can be generated through the direct piezoelectric effect. In order to improve the orientation and reduce the diameter of the nanowires, textured nanoplatelets prepared in situ were used. Figures 2.7h-i show representative SEM images of nanowires grown from the textured nanoplatelets. The nanowire arrays are extremely dense (~$10^{10}$ wires/$cm^2$) with epitaxial orientation. The orientation was quantified using XRD (Figures 2.7j) and shows only a (002) reflection, indicating the high degree of alignment. TEM images of single nanowires (Figure 2.7k) show the highly crystalline nature and several planar defects in the basal plane. High-resolution TEM (Figure 2.7l) along the nanowire c-axis illustrates these disruptions in the periodicity of the crystal lattice. The density of these defects varies from nanowire to nanowire, which would contribute to differences in piezoelectricity and resistivity between nanowires.

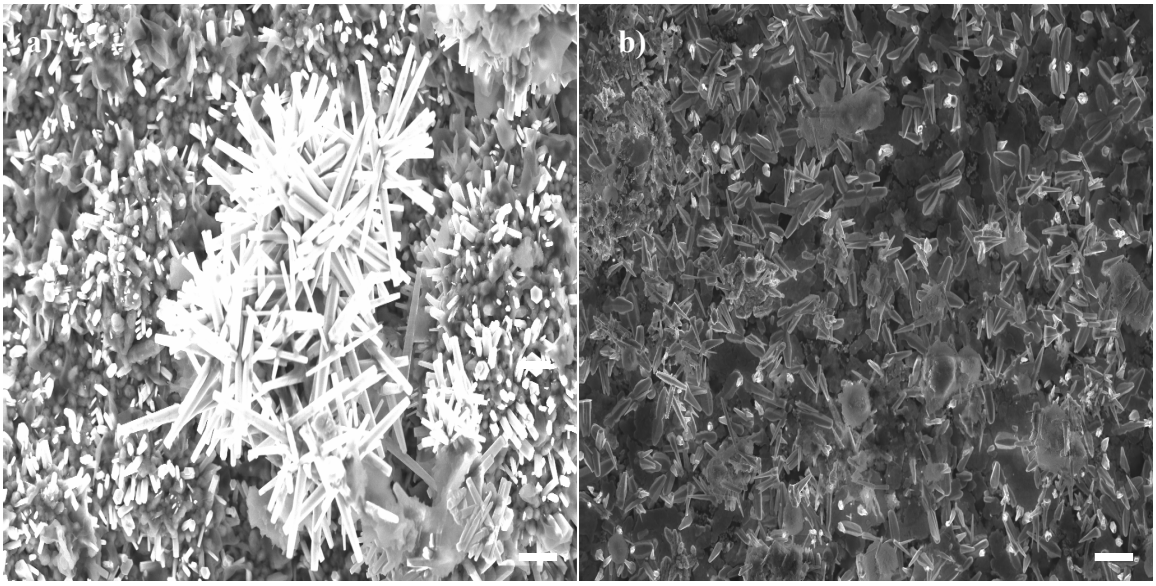

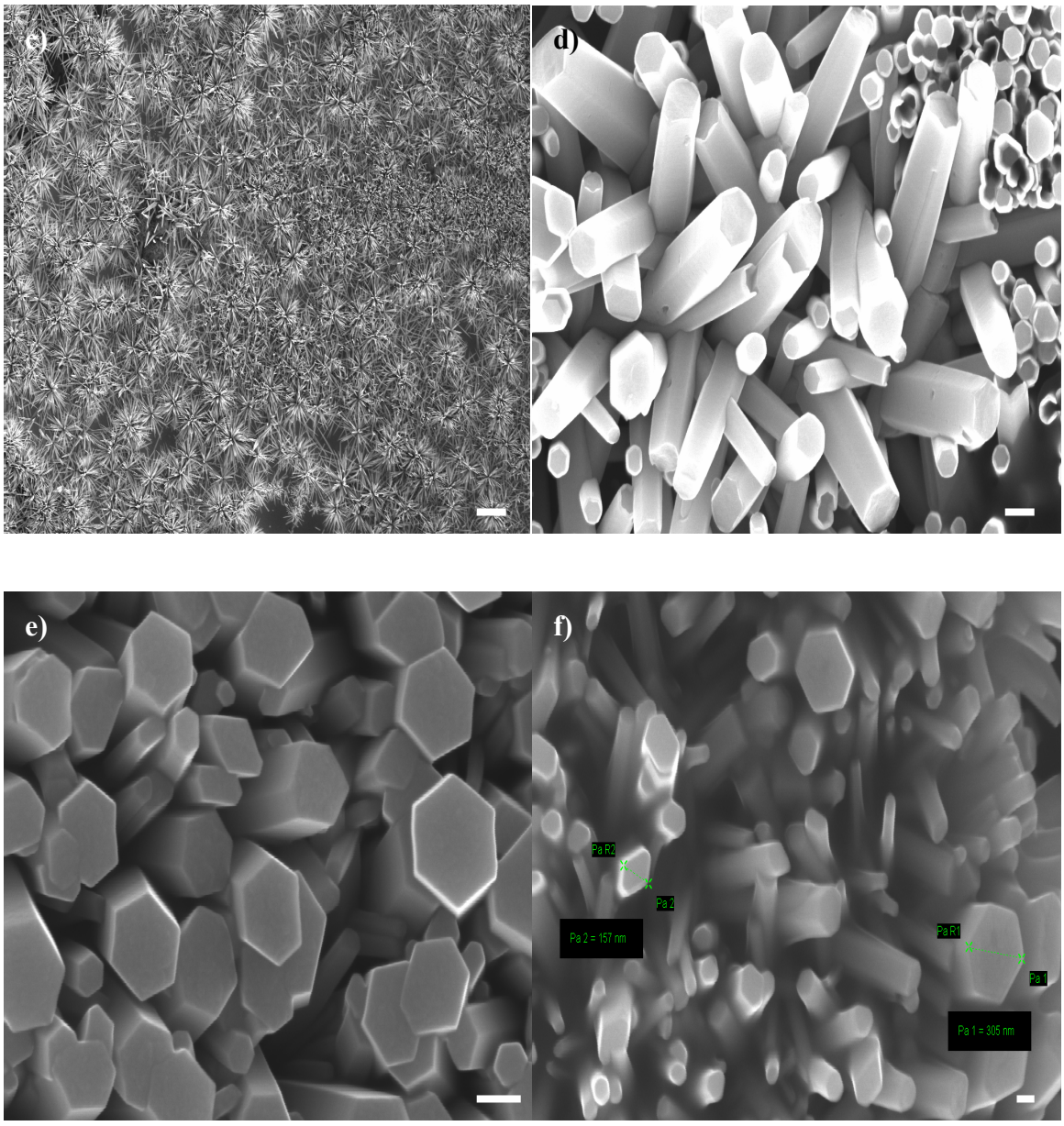
c)
d)
e)
f)
Pa R2
Pa 2
Pa 2 = 157 nm
Pa R1
Pa 1
Pa 1 = 305 nm

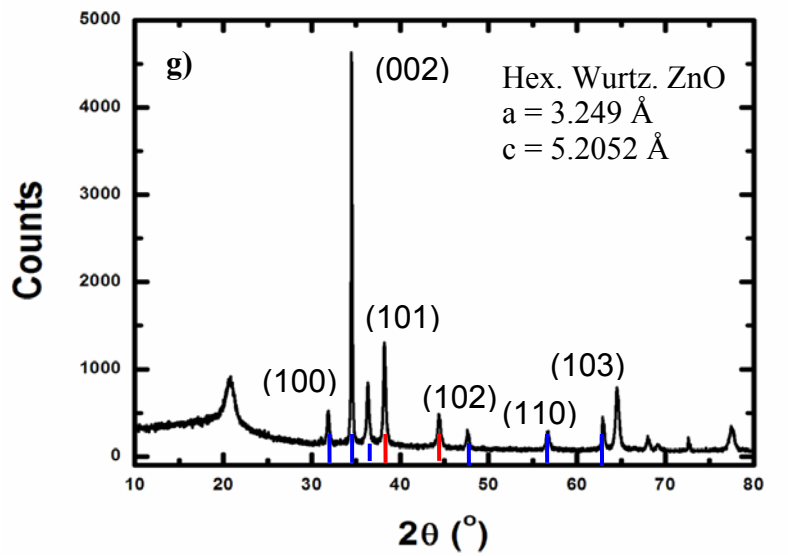
g)
(002)
Hex. Wurtz. ZnO
a = 3.249 Å
c = 5.2052 Å
(101)
(100)
(102)
(110)
(103)
Counts
2θ (°)
5000
4000
3000
2000
1000
0
10
20
30
40
50
60
70
80

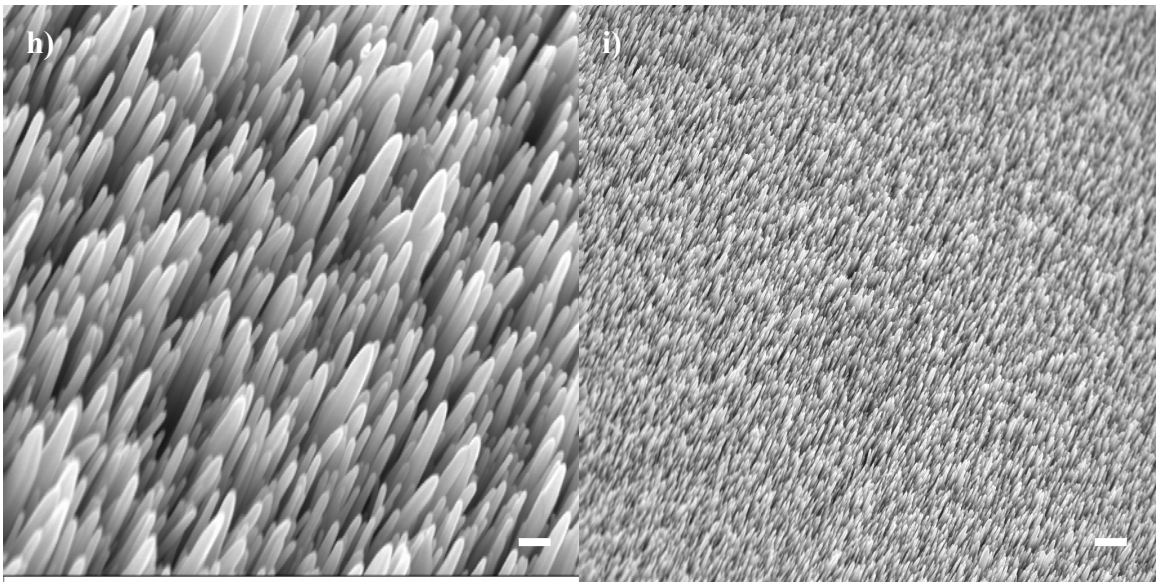
h)
i)

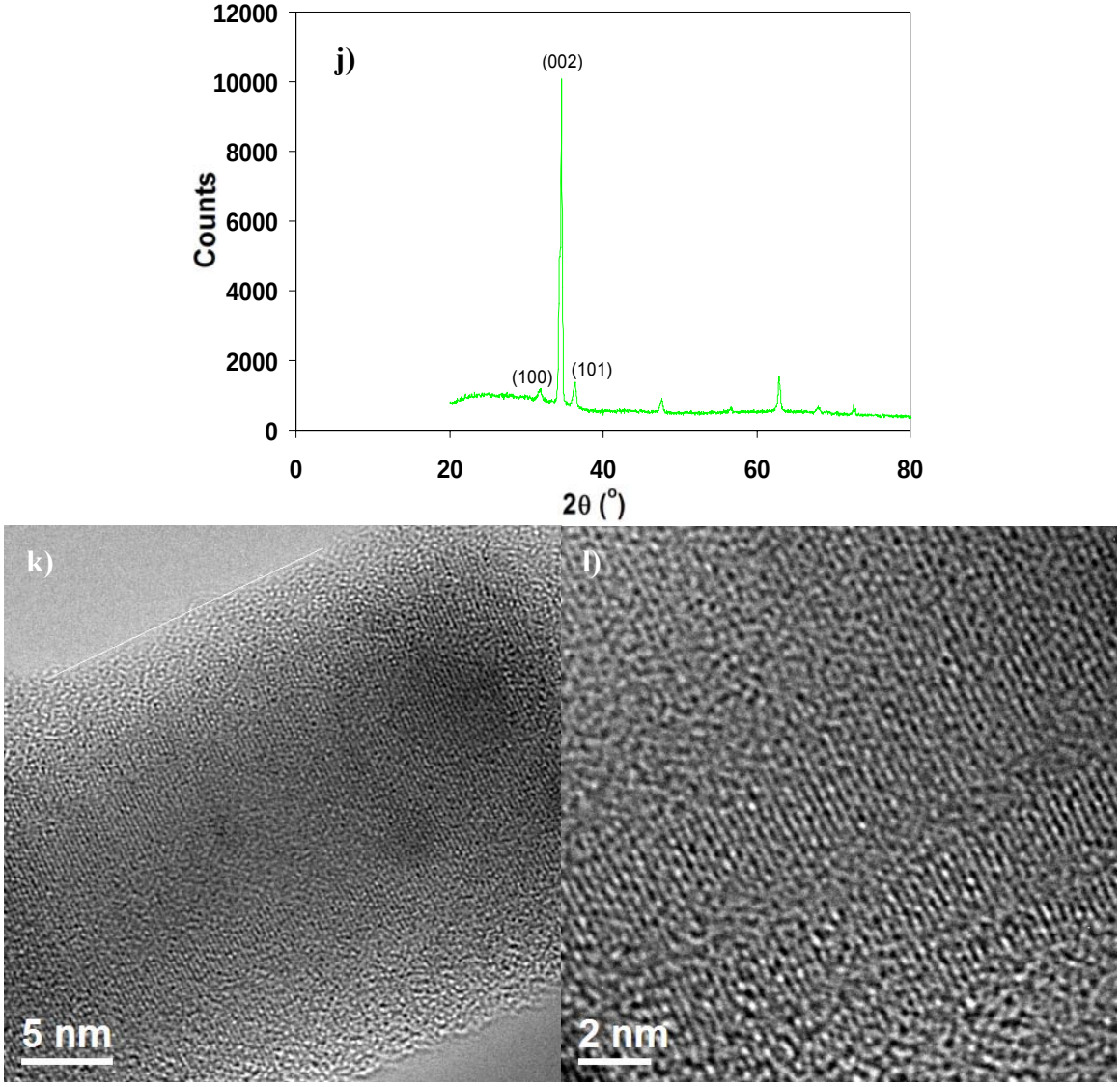
j)
(002)
(100)
(101)
Counts
12000
10000
8000
6000
4000
2000
0
0
20
40
60
80
2θ (°)
k)
5 nm
l)
2 nm

Figure 2.7: Nanowire arrays grown from each type of catalyst seed. a) SEM image of nanowires grown from the spherical nanoparticles. Scale bar is 2µm. b) SEM image of nanowires grown from the spherical nanoparticles using more concentrated solution. Scale bar is 10µm. c) SEM image of nanowires grown from the quasi-spherical nanoplatelets. Scale bar is 10µm. d) High-magnification SEM image of nanowires grown from the quasi-spherical nanoplatelets on same device at different location. nanowires grow at various angles stemming from larger catalyst site. Scale bar is 200nm. e) SEM image of nanowires grown from triangular nanoprisms. Scale bar is 200nm. f) SEM image of nanowires grown from triangular nanoprisms. Scale bar is 100nm. g) XRD of nanowires grown from pyramidal nanocrystals and corresponding ZnO peaks (Blue lines) to crystal planes (numbered above peaks). h) Tilted high magnification SEM image of nanowires grown from the textured nanoplatelets. Scale bar is 200nm. i) Tilted far-field SEM image of nanowires grown from textured nanoplatelets. Scale bar is 1µm. j) XRD of nanowire array grown from textured nanoplatelets. The (002) reflection is clearly enhanced over the other peaks demonstrating the high degree of orientation. k) High-resolution TEM image of single nanowire. l) High-resolution TEM image along the nanowire demonstrating crystalline nature.

### 2.3.1 OPTIMIZATION OF POINT OF ENTRY OF SUBSTRATE INTO GROWTH SOLUTION

The optimal point at which the substrate supporting the nanowire array was introduced into the reaction bath was empirically determined. (Fig. 2.8a) shows an SEM image of a substrate that was immersed into the reaction bath at ambient temperature before the bath had begun to heat up. At room temperature, the preformed nanocrystals dissolved and no nanowires were grown on the substrate. (Fig. 2.8b) shows an SEM image of a substrate that was immersed just after the temperature of the bath reached ~90°C. Heavy precipitates from the solution decorate the surface and effectively bury the nanowire array, rendering the device useless. (Fig. 2.8c) shows an SEM image of a substrate that was immersed when the reaction bath reached a stable temperature and turned from clear to cloudy (whitish), or approximately 90 minutes after the bath reached the appropriate temperature. The prolonged time reduced the density of free-floating

particulates capable of short-circuiting the device or shielding the nanowires from making a connection to the top electrode. To further reduce the number of reaction products from adsorbing on the nanowires, the growth solution was first pre-heated to 65°C in a separate intermediate bath. The warm solution was then pumped and filtered through filter paper before being fed into the reaction bath and heated to 90°C. The lowered concentration of the filtrate was ideally suited for anisotropic growth of the nanowire array.

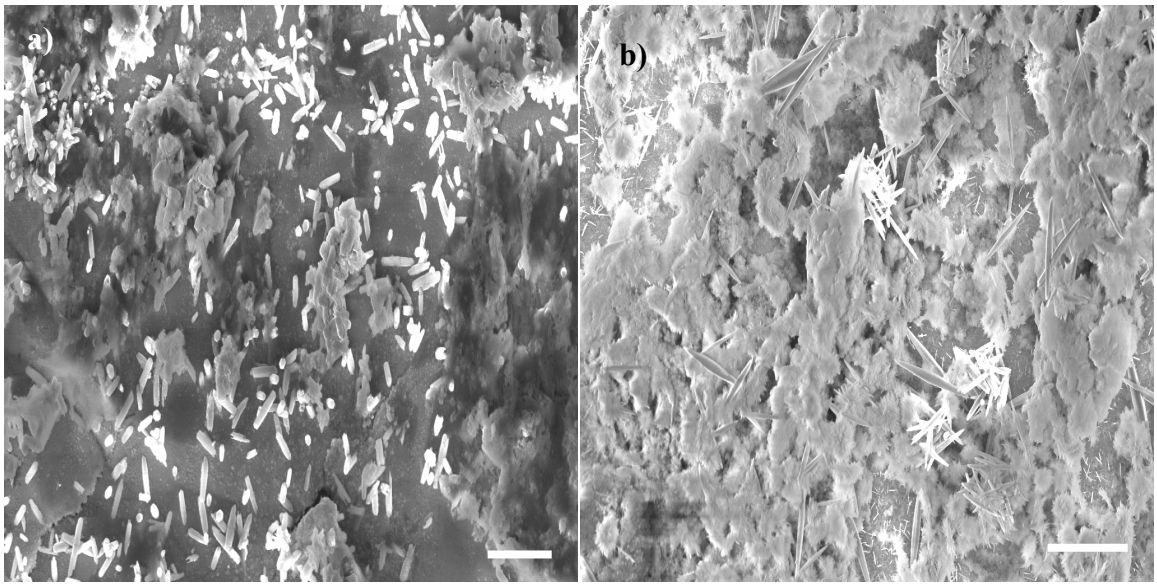

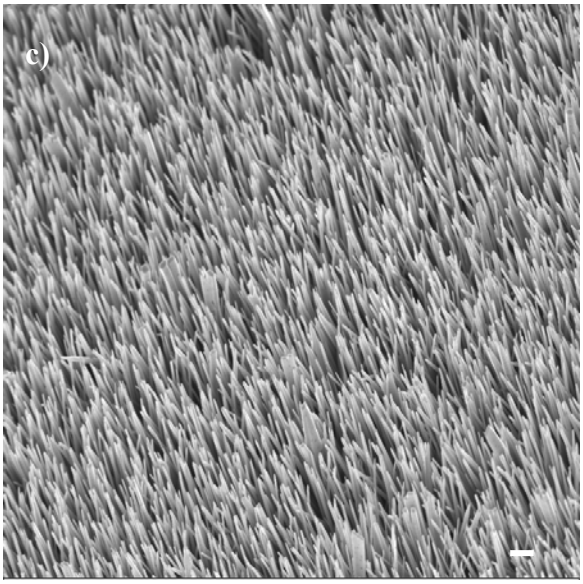


Figure 2.8: Optimized point of entry for the substrate into the reaction bath. a) SEM image of substrate immersed at room temperature. b) SEM image of substrate immersed just after reaction bath reached 90°C. Scale bar for a & b is 10 μm. c) Tilted SEM image of substrate immersed after solution was pre-heated, filtered and then heated at 90°C for ninety minutes. Scale bar for is 2 μm

### 2.3.2 GROWTH OF HIGH ASPECT RATIO NANOWIRES

To grow nanowires with aspect ratios above 50, the substrate supporting the nanowire array had to be introduced into fresh, hot solution every 2 hours. After 2 hours in solution, the substrate was removed from the reaction bath, cleansed thoroughly with DI water, cleaned with Reactive Ion Etching (RIE, 30W, 20sccm $O_2$, 30 seconds) and baked in vacuum for 1 hour to remove moisture. After annealing, the substrates were immersed back into the growth solution for 2 hours. The process was repeated until 36 hours of growth time was achieved. Figure 2.9a shows a magnified SEM image of nanowires grown by repeated removal and reentry into fresh solution baths. The length of the nanowires is near 12 microns (Figure 2.9b).

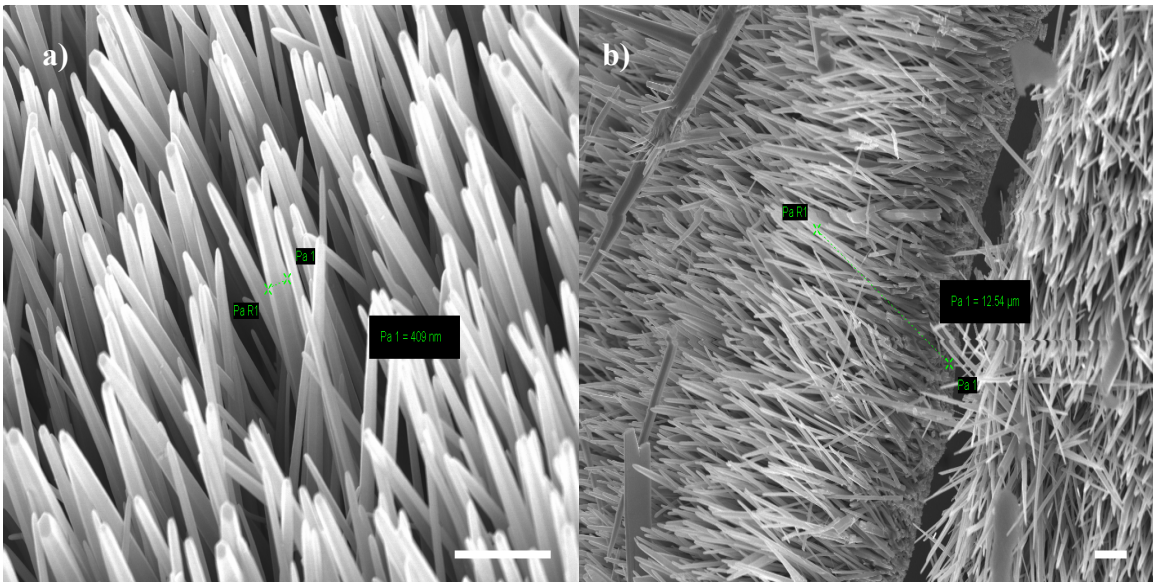


Figure 2.9: Growth of high aspect ratio nanowires. a) Tilted high magnification SEM image of nanowires grown from repeated entry into fresh solutions. Nanowires are highly aligned and average diameter is near 0.5 µm. Scale bar is 2µm. b) Tilted SEM image of fractured array of nanowires grown in optimized conditions. Scale bar is 2µm.

Rather than constantly placing the substrate into fresh solution baths, two peristaltic pumps were employed where one pump flows in fresh solution at 75mL/hour and the other pump extracts solution at 25 mL/hour (Figure 2.10). The constant influx of fresh solution delivers a steady supply of the precursors while the efflux maintains the pH of the bath and helps to remove reaction products floating in solution. Since the reaction vessel is open to ambient, ammonia in the reaction bath evaporates and decreases the base concentration. After approximately 20 hours, the pH of the reaction bath was adjusted from 6.1 to 8 with slight additions of ammonium hydroxide. Since nanowire

growth needs ammonia to coordinate with zinc nitrate, the extra ammonia ensured growth could be maintained for prolonged periods.

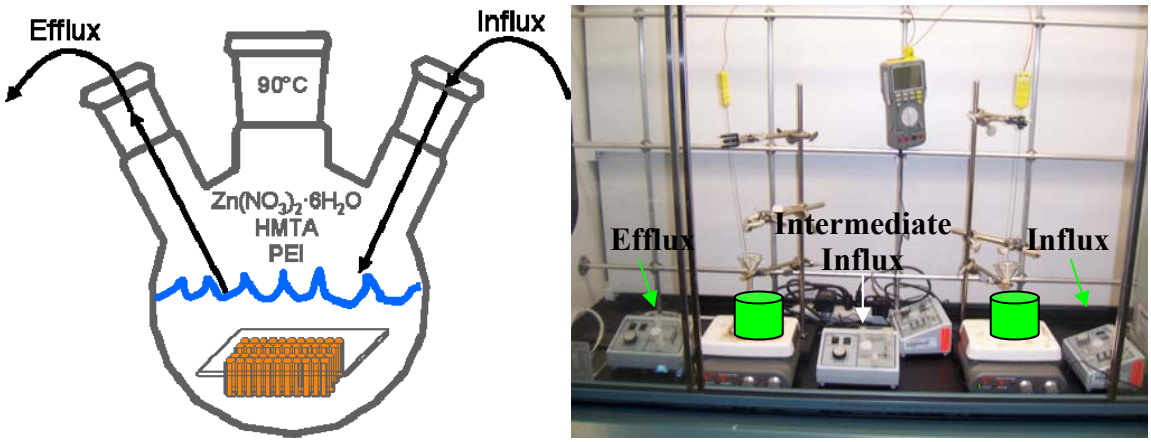


Figure 2.10: Automated system to produce high-aspect ratio nanowires. A peristaltic pump delivers a flux of fresh solution and maintains the pH of solution by evacuating aged solution. a) Schematic of reaction bath for growing oriented nanowires with large aspect ratios. b) Photograph of workbench for growing oriented nanowires.

As the length of the nanowires increased, the diameter also tended to increase proportionally. To arrest the radial growth of the nanowires, the concentration of PEI was increased from 0.005M to 0.007M. The increase in the concentration of the cationic polyelectrolyte was very effective at keeping the average nanowire diameter under 200nm (Figure 2.11a), while still allowing the length to grow upwards of 15 microns (Figure 2.11b). The resulting arrays were densely packed and highly oriented.

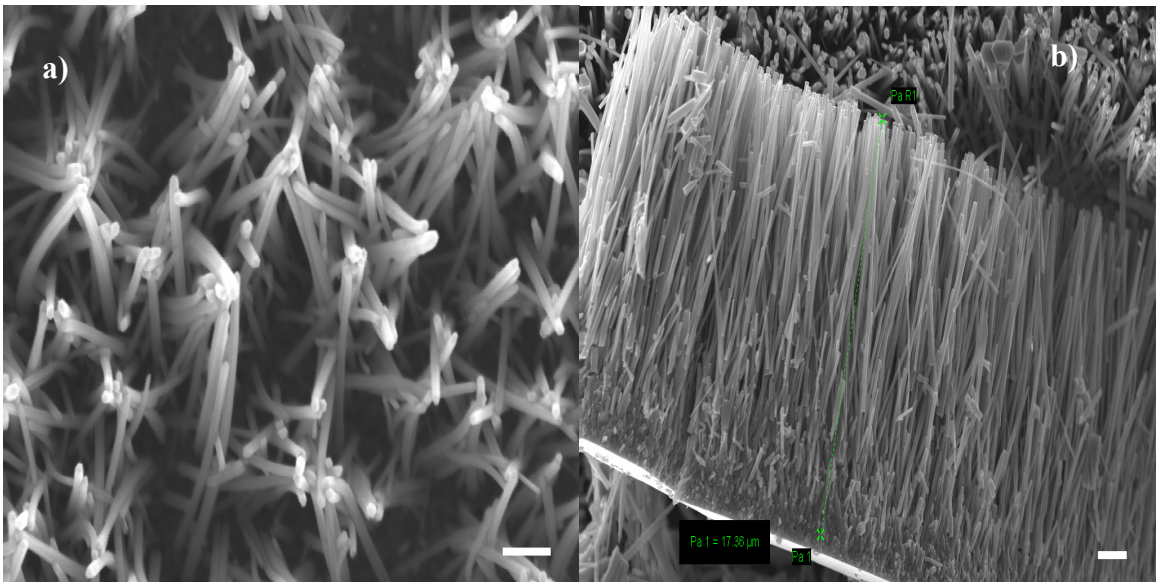


Figure 2.11: Optimized extended growth of nanowires. After increase in the concentration of the cationic polyelectrolyte (PEI), the average nanowire aspect ratio increased considerably. a) SEM image of nanowires grown from optimized conditions. Scale bar for is 200nm. b) SEM image of cleaved array of nanowires grown in optimized conditions. Scale bar is 2µm.

### 2.3.3 FURTHER ENHANCEMENT OF ASPECT RATIO OF ZnO NANOWIRES

Chapter 3 of this dissertation will demonstrate how increasing the aspect ratio returns higher piezoelectric outputs. In an effort to grow nanowires with aspect ratios over 75, the precursor concentration of both ZnNH and HMTA was adjusted from 0.025M to 0.02M. The slight decrease in the concentration of precursors has been argued to decrease the size of the nanowires in both length and diameter. Since there are fewer precursors in the solution to react with the surface of the growing nanowires, the growth rate is restricted. The average diameter of nanowires decreased with the slightly lower concentration of precursors to 90±40nm. The nanowires tended to bend towards other

nanowires to keep upright and share the load of their weight. Figure 2.12a shows an SEM image of several nanowire "bunches" that have buckled and synergistically supported themselves by "sharing each other's load." Figure 2.12b is a far-field SEM image of hundreds of wire bunches showing how the "synergistic load sharing" effect is extended over the entire array (inset is magnified view of several bunches). The flexibility of the nanowires is striking considering how far they can be flexed without breaking to support themselves. Figure 2.12c displays an SEM image of a bundle of nanowires that form an 'S' shape and are still rigidly attached to the bottom electrode (Figure 2.12d). Accompanying the decrease in the diameter was a decrease in the average length. Figure 2.12e shows an SEM image of the length of the same array of nanowires to be around average 6-7 microns, and figure 2.12f shows an average nanowire diameter which gives an average aspect ratio of 72.

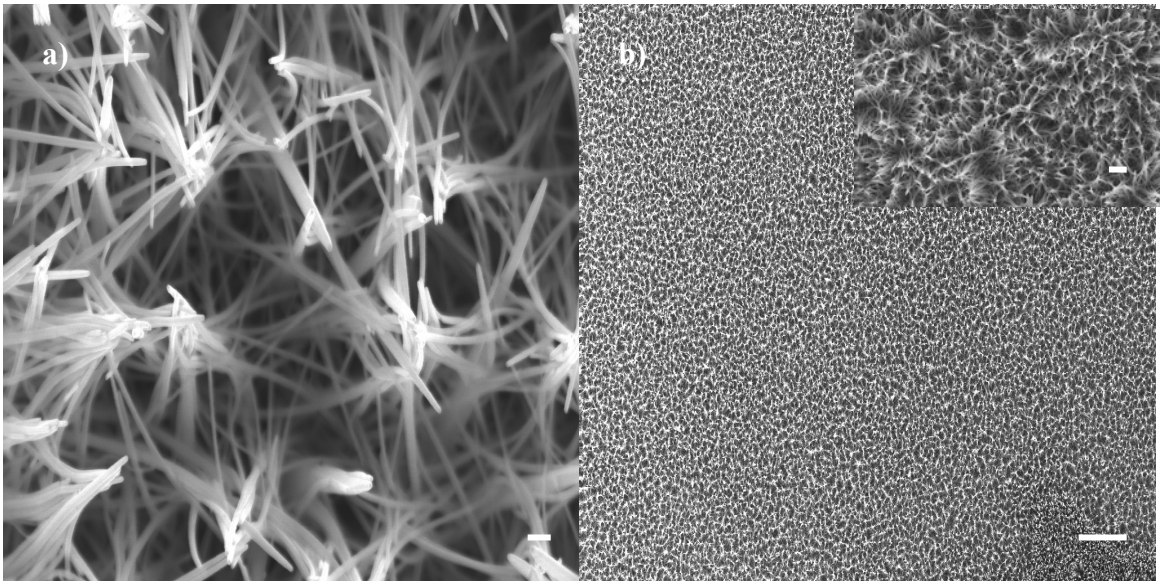

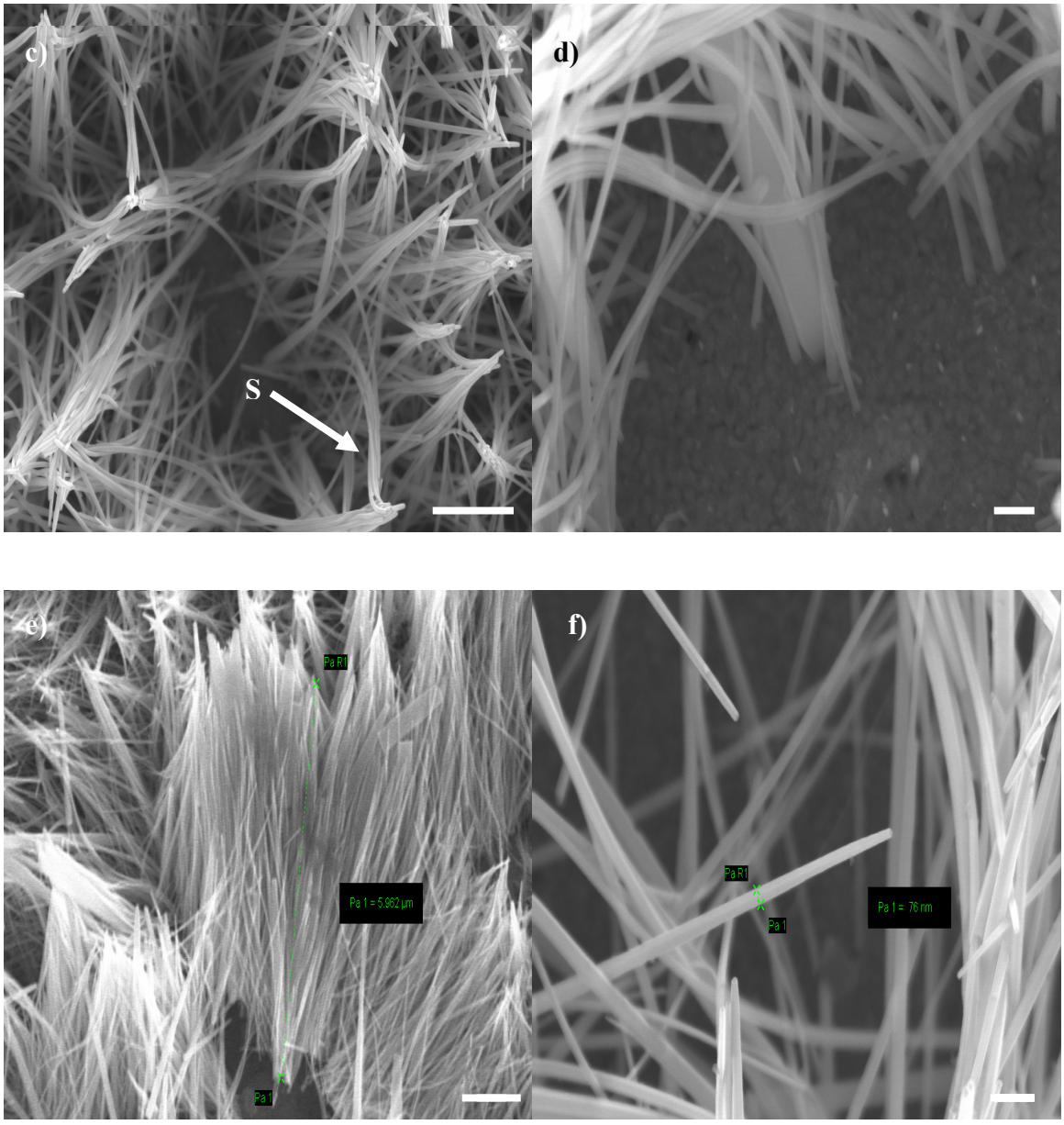
c)
S
d)
e)
Pa R1
Pa 1 = 5.962 µm
Pa 1
f)
Pa R1
Pa 1
Pa 1 = 76 nm

Figure 2.12: Further enhancement of aspect ratio of ZnO nanowires. The decrease in the concentration of precursors further increased the nanowire aspect ratio. a) SEM image of nanowires grown from decreased precursor concentration. Scale bar is 200nm. b) Far field SEM image of higher aspect ratio nanowires showing synergistic load sharing effect extends over large array. Scale bar is 10μm. Inset is magnified view of one area of array, scale bar is 1μm. c) SEM image of highly flexible nanowires. Nanowires can form 'S' shape and still be rigidly attached at the base, indicating high degree of mechanical flexibility. Scale bar is 1 μm. d) Magnified SEM image of nanowires attached at the base / electrode. Scale bar is 200nm. e) SEM image of nanowire length. Scale bar is 1 μm. f) Magnified SEM image of nanowire diameter. Nanowire diameters range from 20nm-200nm. Scale bar is 100nm.

### 2.3.4 LIMIT TO ASPECT RATIO OF NANOWIRES

In an effort to further increase the aspect ratio of the nanowires, the precursor concentration of ZnNH and HMTA was further decreased from 20mM to 10mM. Figure 2.13a shows a sample of nanowires grown for 33 hours in decreased precursor concentrations. The nanowires tended to 'bundle' together again and were slightly smaller in diameter (45±20nm) with approximately the same length (6-7μm). However, the decrease in diameter also accompanied a 'buckling' effect, where a substantial portion of the nanowire array would fold over or bend severely rather than stand perpendicular to the substrate (Figure 2.13b-c). This effect was expected, as the nanowires have an average aspect ratio over 150. Since the goal of the synthetic approach was to build a nanowire array with high orientation perpendicular to a substrate, nanowires with such a high aspect ratio would be ineffective at producing energy through the direct piezoelectric effect. Rather, the nanowires would plastically deform or bend and not be able to recover their shape, effectively stopping the generator from working.

This ‘buckling effect’ seen at lower precursor concentrations and low seeding densities, put a limit on the aspect ratio of the nanowires.

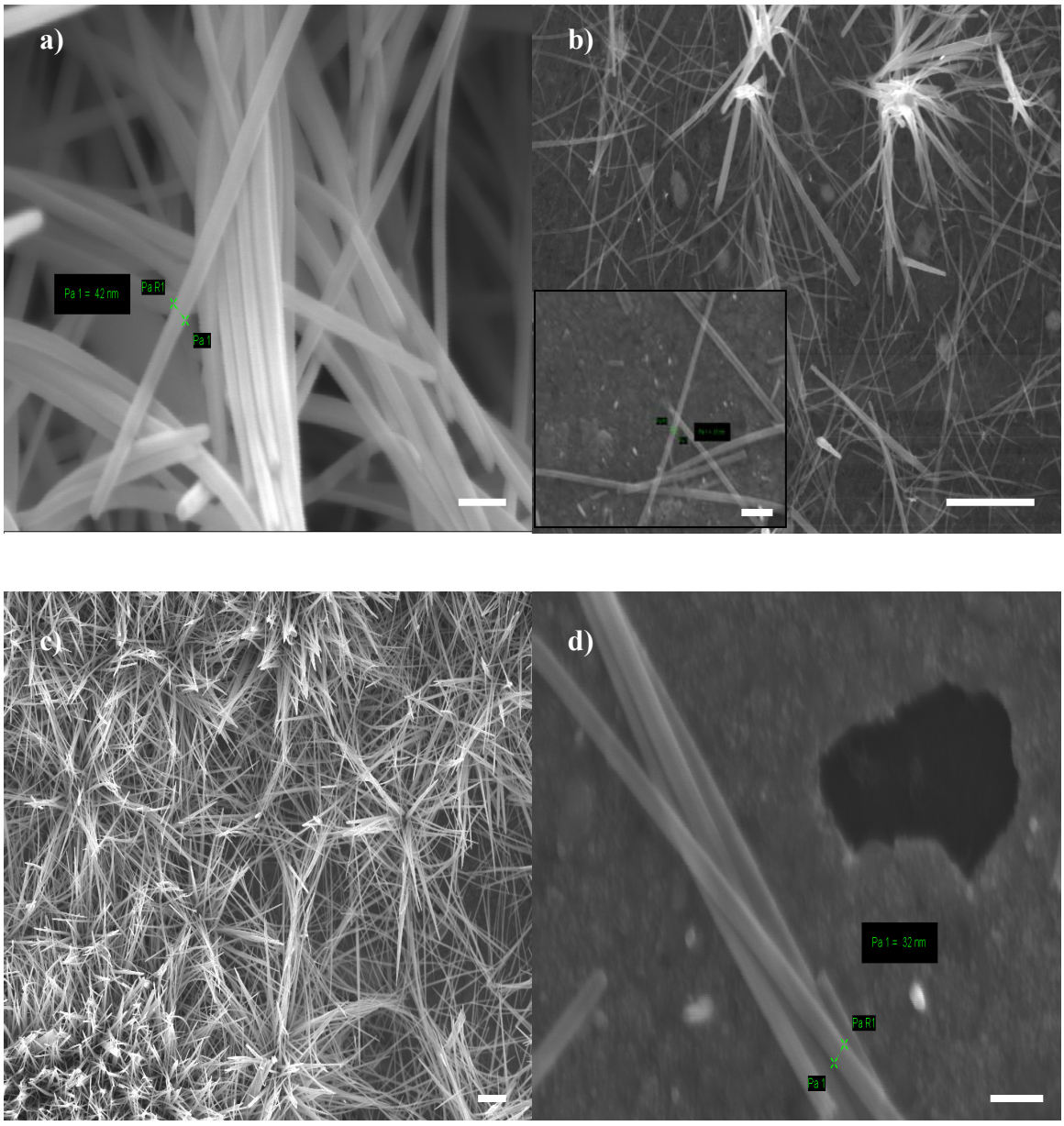

Figure 2.13: Limit to nanowire aspect ratio. The decrease in the concentration of precursors increased aspect ratio of nanowires by decreasing average nanowire diameter. a) High magnification SEM image of nanowires grown from decreased precursor concentration. Scale bar is 100nm. b) SEM image of thin nanowires buckling. Scale bar is 2μm. Inset is high magnification image of buckled nanowires laying flat on substrate. Scale bar is 100nm. c) SEM image of array of thin nanowires with majority of nanowires curled or bent over. Scale bar is 2μm. d) High magnification SEM image of thin nanowires that have buckled and rest flat on the electrode. Scale bar is 200nm.

To abate the buckling effect of higher aspect ratio nanowires, a higher density of textured seeds was created on the substrate. By increasing the population density of seeds and in turn nanowires, neighboring nanowires could effectively support one another and synergistically share each other's load, preventing the buckling effect. This was accomplished by using a higher concentration of zinc acetate dihydrate (ZnAcD) crystallites; 0.01M rather than 0.005M. Figures 2.14a-c display an array of nanowires grown for 36 hours in decreased precursor concentrations (0.01M ZnNH & HMTA) with a higher seeding density (10mM ZnAcD). The increase in the density of the nanowire array is a direct result of the increased density of nucleation sites. Accompanying the increase in population density of nanowires was also an increase in the average diameter and a much more broad distribution of nanowire sizes. Interestingly, the smallest diameter nanowires were almost always located near the largest diameter nanowires as depicted in Figures 2.14b-c. The increase in the average diameter can be viewed from two perspectives: 1) the increased density of catalyst sites could form bigger nucleation sites for larger diameter nanowires to nucleate and grow or 2) growing nanowires have buckled or grown into one another during kinetic growth and fused to form larger diameter nanowires. This effect is also known as Ostwald Ripening.

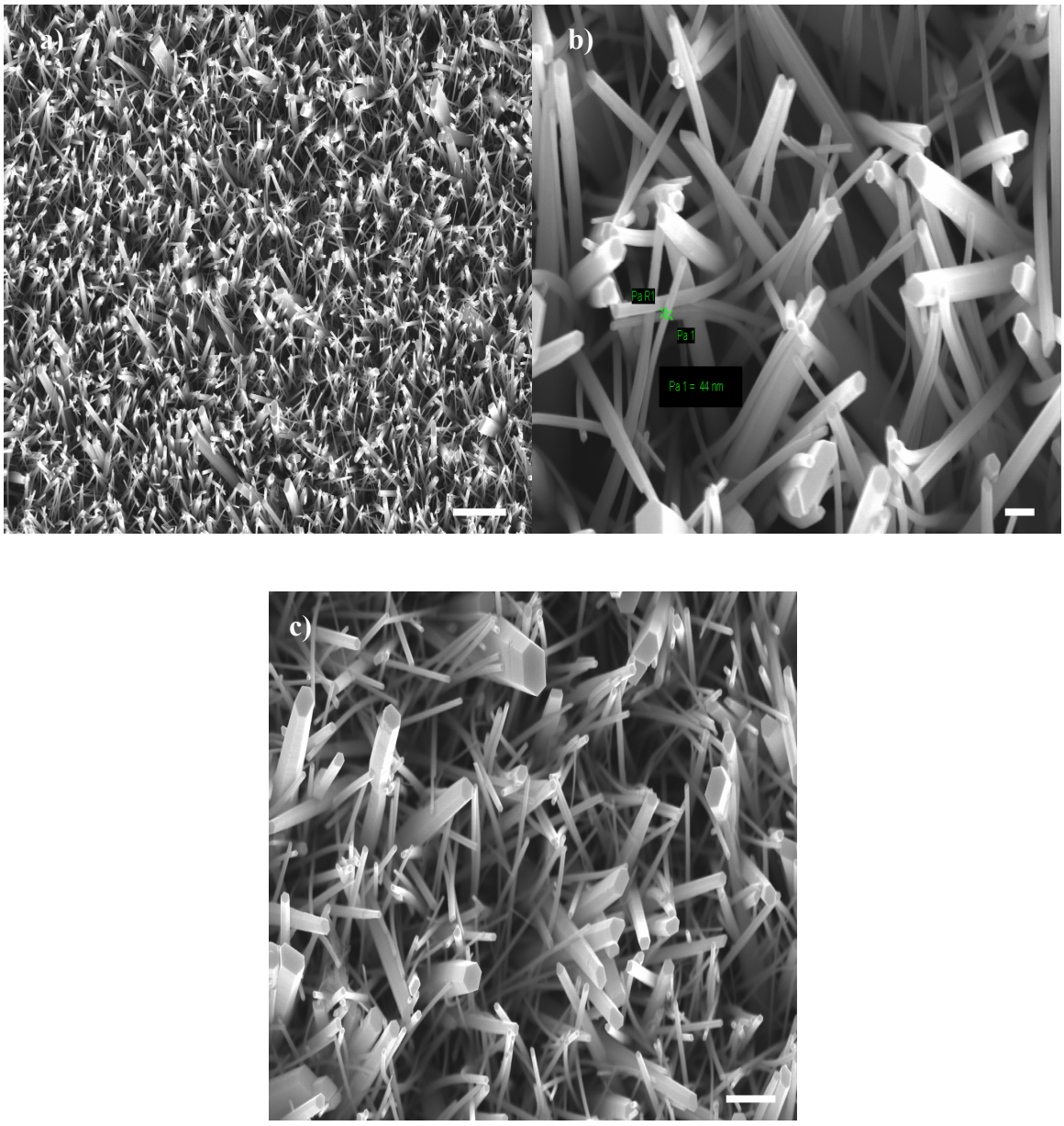


Figure 2.14: Higher density of catalyst seeds induced Ostwald ripening. The increased population density of seeds did aid the nanowires from buckling but it also increased the average nanowire diameter and size distribution. a) SEM image of nanowires grown from increased seed density. Scale bar is 3µm. b) SEM image of thin nanowires next to larger diameter nanowires. Scale bar is 200nm. c) SEM image of different area of thin nanowires neighboring with thicker nanowires. Scale bar is 1µm.

### 2.3.5 OSTWALD RIPENING OF NANOWIRES AFTER EXTENDED GROWTH

To investigate whether the nanowire arrays underwent Ostwald ripening, substrates seeded with a higher density (0.01M) were grown for 48 hours total growth time. Figure 2.15a displays an array of nanowires grown for 48 hours in decreased precursor concentrations (0.01M ZnNH & HMTA) and seeded with a higher concentration (10mM ZnAcD). There are several microrods extending from the nanowire array that are thicker in diameter and again are near the smallest diameter nanowires. Figure 2.15b portrays an SEM image of several smaller diameter nanowires as they are about to fuse with a larger diameter nanowire. This substrate was removed after 34 hours of growth to investigate whether the smaller diameter nanowires were fusing or beginning to feed into the larger diameter nanowires and undergoing 'Ostwald ripening'. Figure 2.15c shows a magnified SEM image of a small diameter nanowire on the same substrate in a different area, as it is in the process of fusing into a larger diameter nanowire and two smaller diameter nanowires already fusing into a larger diameter nanowire. Ostwald ripening is further confirmed upon viewing the atomic structure of the nanowires with TEM (Figure 2.15d). Nanowires were sonicated off from the sample and drop casted onto lacey carbon mesh TEM grids. It is evident from Figure 2.15d that the outer layer of the nanowire is composed of randomly oriented nanoparticles. Sorption of ions or anisotropic nanoparticles on the (0001) face during growth is expected, possibly undergoing a dissolution-reprecipitation process and promoting growth along the polar axis. However, growth of the non-polar axes encouraged by the presence of such ions and nanoparticles is also present in Figure 2.15e. This effect of one nanowire dissolving and reprecipitating into another nanowire was also seen by Govender[85]. As the smaller diameter nanowires age in solution, neighboring larger nanowires will begin to draw material in the form of ions and anisotropic

nanoparticles from the smaller nanowires, which have to shrink and/or fuse with larger diameter nanowires. This stems from the fact that molecules on the surface of a smaller nanowire are energetically less stable than the ones already well ordered and packed in the interior of a larger diameter nanowire[90]. As the reaction bath tries to lower its overall energy, molecules on the surface of a small (energetically unfavorable) nanowire will tend to dissolve and diffuse through solution towards the larger nanowire and add to the surface. Also apparent from TEM is the lattice configuration and planar defects in the basal plane (Figure 2.15f). The disorder of the periodicity of the crystal lattice varied between nanowires where some did not include any defects and were single-crystalline nanowires. The selected area electron diffraction (SAED) pattern was also taken along the polar axis (inset to Figure 2.15f). The TEM images indicate that the as-grown nanowires are rich in atomic defects, which is consistent with photoluminescence measurements taken on as grown hydrothermally grown nanowires[91]. It should be noted here that the density of the nanowire defects can be quenched by annealing in various environments such as hydrogen. This effect will be studied more in Chapter 4 of this dissertation using low energy photoelectron spectroscopy.

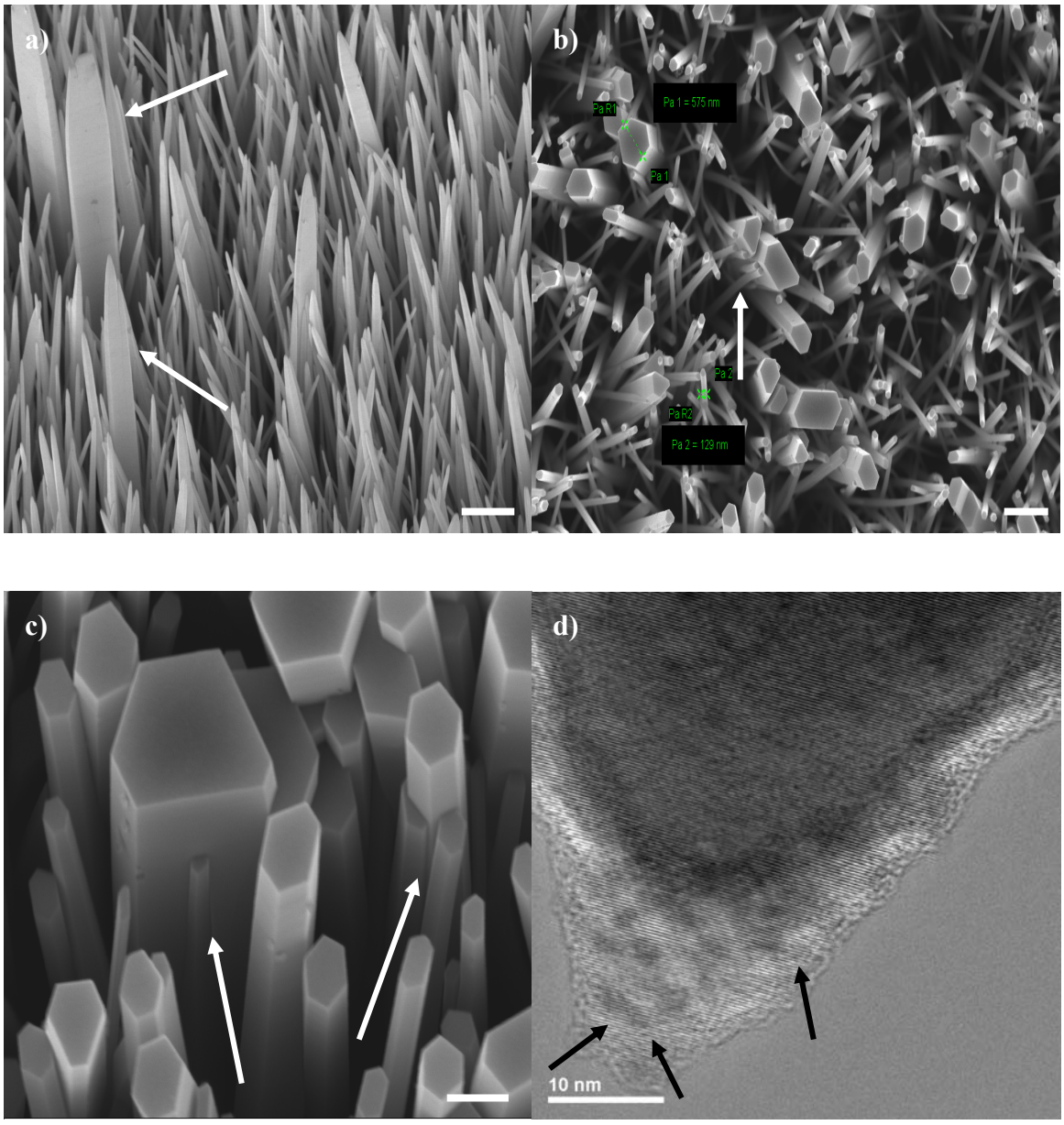
a)
b)
Pa 1 = 575 nm
Pa R1
Pa 1
Pa 2
Pa R2
Pa 2 = 129 nm
c)
d)
10 nm

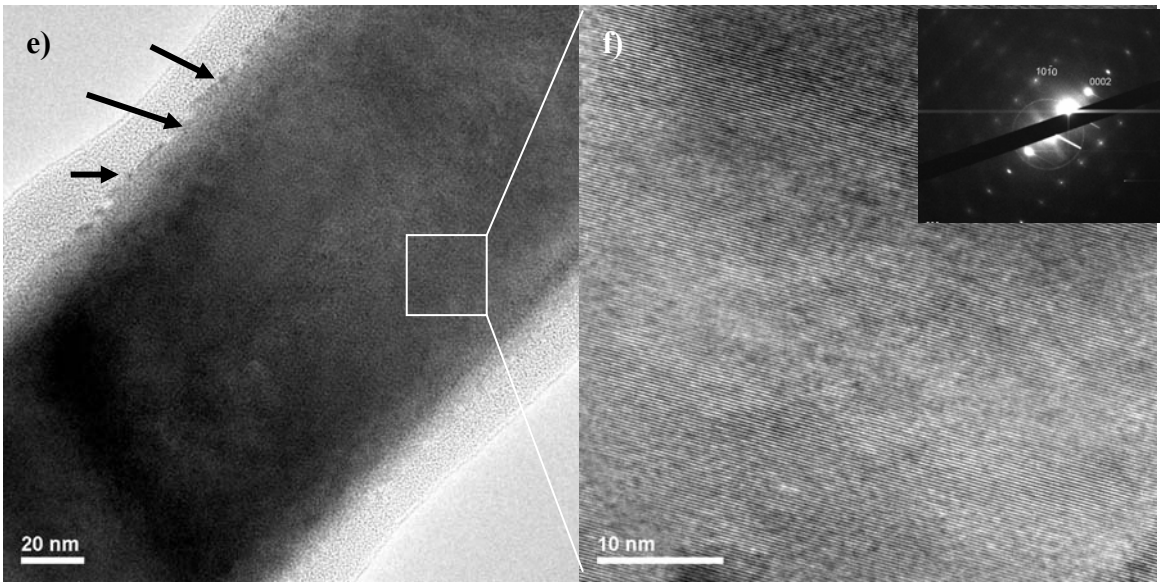


Figure 2.15: Ostwald ripening of nanowires grown for extended periods. a) SEM image of fused nanowires at 45° tilt. Arrows point to larger diameter nanowires that are taller and 'thicker'. Scale bar is 1 μm. b) Bird's eye image of nanowire array showing how smaller diameter wires have fused together to form larger diameter nanowires. Arrows point to smaller diameter nanowires beginning to fuse with larger diameter nanowires. Scale bar is 1 μm. c) Magnified SEM image of larger diameter nanowires being fused with smaller diameter nanowires. Scale bar is 200nm. d) HR-TEM image of tip of nanowire showing randomly oriented nanoparticles decorating surface. e) HR-TEM image of non-polar face of nanowire showing randomly oriented nanoparticles decorating surface. f) HR-TEM image of nanowire showing lattice structure. Inset is SAED recorded for nanowire along the (002) axis.

### 2.3.6 EFFECT OF SUBSTRATE ON NANOWIRE ASPECT RATIO AND ORIENTATION

The underlying growth substrate supporting the nanowire array was also found to play a critical role in both the orientation and aspect ratio. The alignment of the nanowire array was primarily influenced by the surface topography of the substrate rather than the surface chemistry or crystallographic orientation. While the previous syntheses were on atomically flat Si substrates with a small oxidized layer, growth on other amorphous oxides such as glass (Figures 2.16a-b), and metals (gold, titanium, chromium, nickel, silver, aluminum, indium-tin-oxide) (Figures 2.16c-d) all supported epitaxial growth.

This suggests that the alignment of the textured ZnO nanocrystals is substrate-independent and can occur on any type of flat surface that can withstand temperatures of at least 200°C. The aspect ratio of the nanowires grown on various other flat surfaces was roughly the same as nanowires grown on oxidized Si.

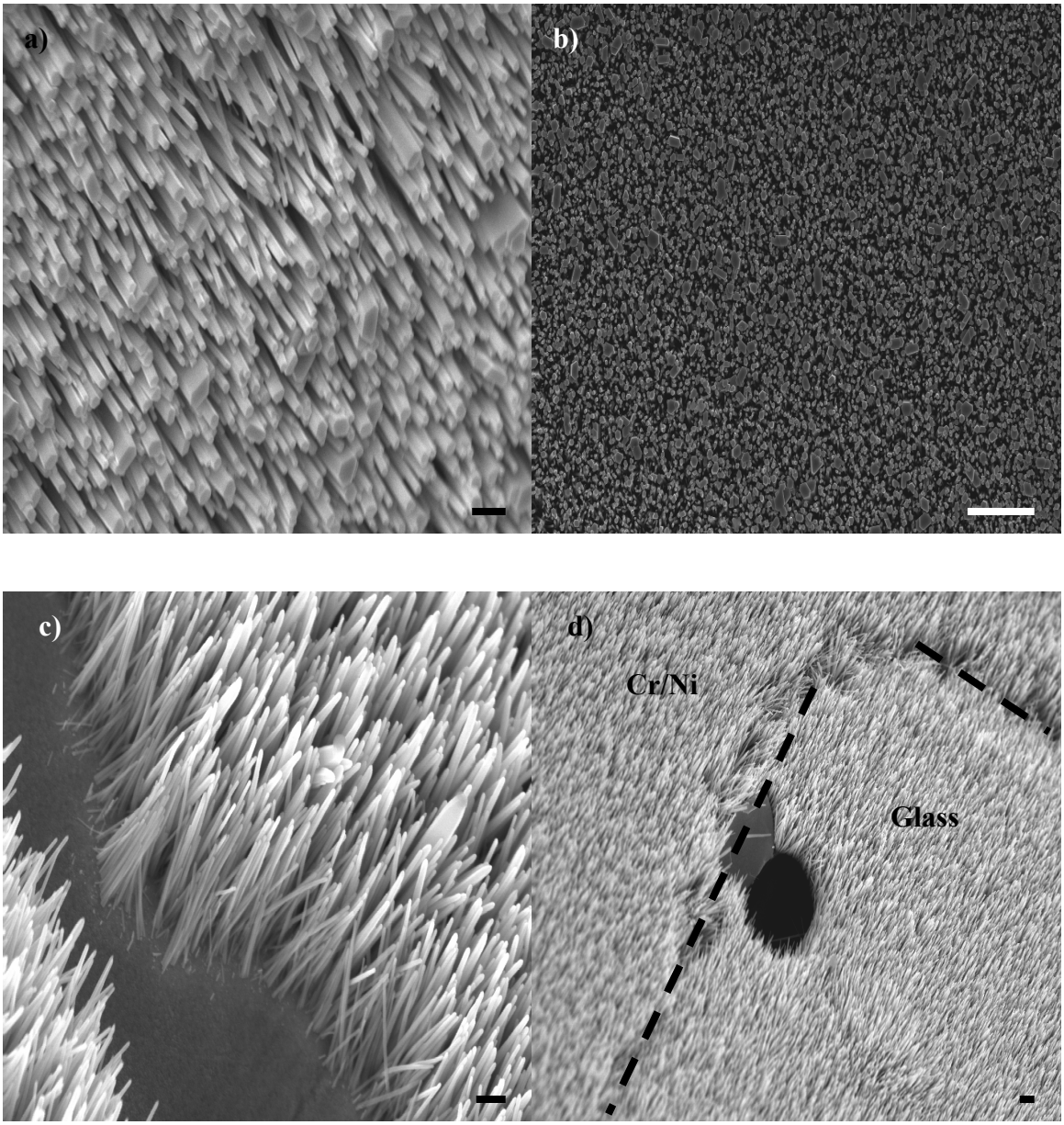

Figure 2.16: Effect of substrate on nanowire aspect ratio and orientation. a) SEM image of nanowires at 45° tilt grown on glass. The high orientation of the array is a result of the seeding strategy and flat surface for epitaxial growth. Scale bar is 1μm. b) Bird's eye image of nanowire array demonstrating high degree of orientation. Scale bar is 10μm. c) SEM image of nanowires at 45° tilt grown on Ti/Au coated Si. Scale bar is 300nm. d) SEM image of nanowires at 45° tilt grown on Cr/Ni coated Si. Scale bar is 1μm.

Growth on aluminum foil and flexible polymers coated with metals such as Cr/Au and Ti/Au-coated polydimethylsiloxane (PDMS) (Figure 2.17a-b), polyethylene terephthalate (Mylar), and polyimide (Kapton) (Figure 2.17c-d) permitted growth of highly oriented nanowire arrays but the orientation was slightly less than those grown on flat surfaces. The poorer alignment of the nanowire array is a result of the increased surface roughness of the underlying plastic substrate. Atomic Force Microscopy (AFM) of the plastic surface after seeding shows a high degree of surface roughness, with large aggregates of seeds that would act as nucleation sites for multiple wires to stem in various directions. The nanowire arrays in Figures 2.17c-d depict such a case, where multiple nanowires are growing from the same seed in 'firecracker' shapes. The average diameter of the nanowires grown on flexible substrates also increased, reducing the aspect ratio.

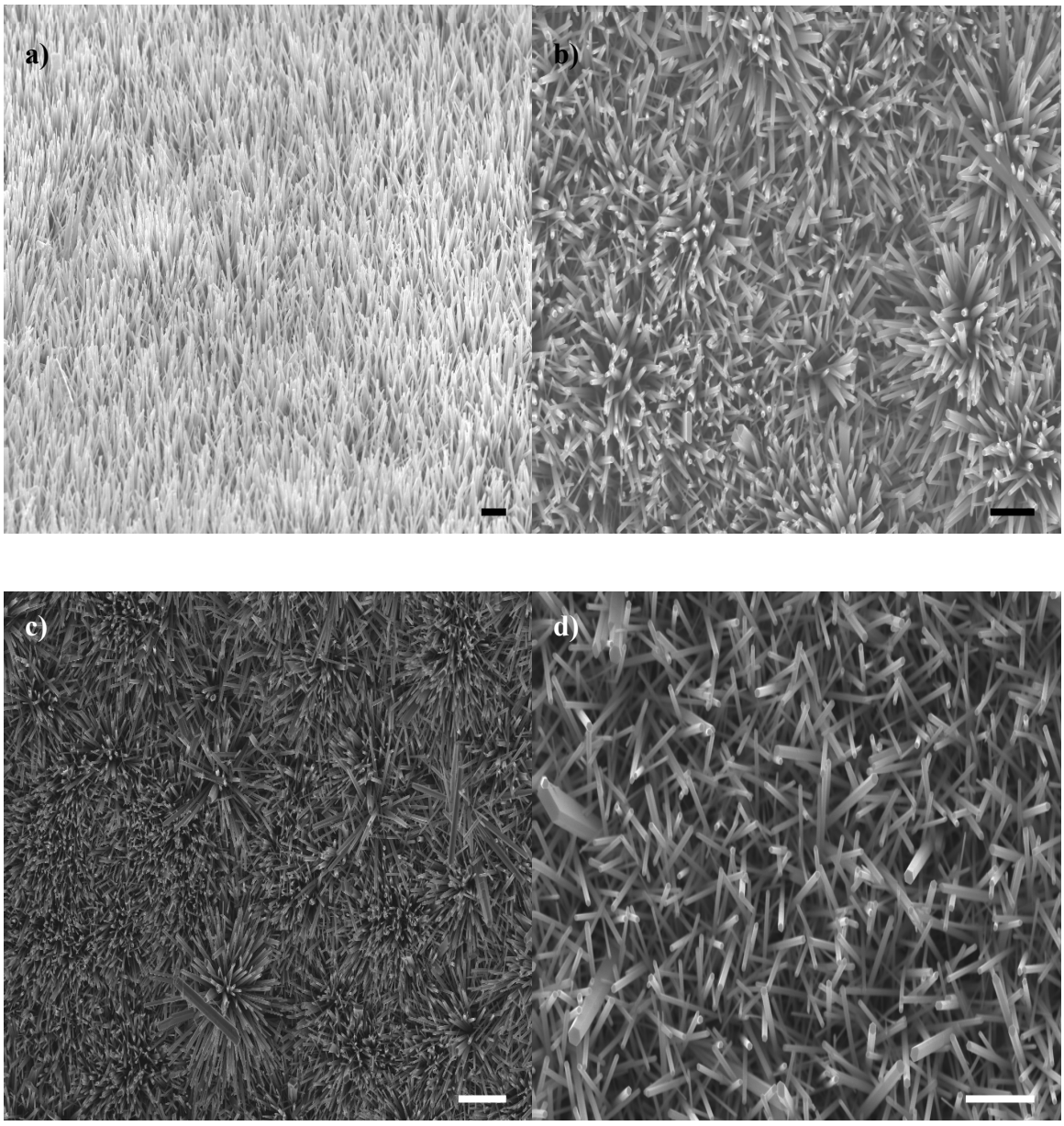
a)
b)
c)
d)

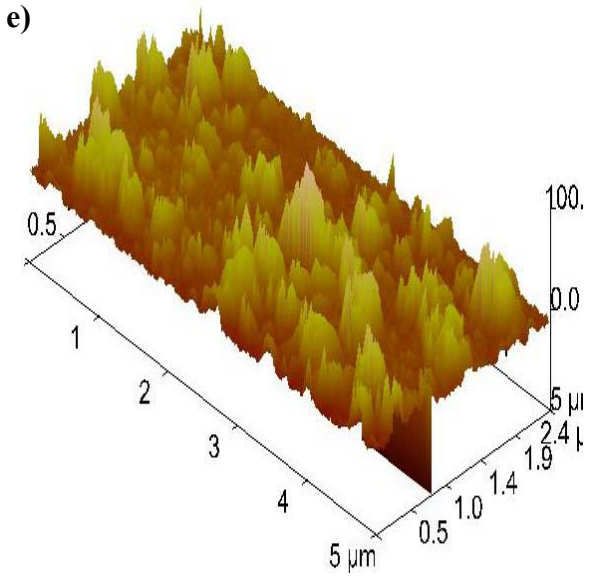


Figure 2.17: Effect of polymer substrate on orientation of nanowire array. a) SEM image of nanowires at 45° tilt showing high orientation is maintained on Cr/Au coated PDMS substrate. Scale bar is 2µm. b) Bird's eye image of nanowire array showing how the array is not as well aligned as the flatter substrates and how the nanowires are growing at different angles. Scale bar is 2µm. c) Far-field SEM image of nanowire array on Cr/Au coated Kapton H film showing how the nanowires tend to grow in 'firecracker' shapes, with several emanating from the same seed (arrows pointing). Scale bar is 10µm. d) Higher magnification SEM image of nanowire array on Cr/Au coated Kapton H film depicting the nanowires grown at various angles. Scale bar is 2µm. e) AFM image of Cr/Au coated Kapton H film after seeding. The surface roughness of the film is very high, demonstrating various aggregates and large nucleation sites for wires to stem in multiple directions.

### 2.3.7 OPTIMIZED ORIENTED GROWTH ON FLEXIBLE SUBSTRATES

To abate the decrease in alignment by substituting a plastic substrate, an alternate seeding strategy was employed. Rather than drop-casting the crystallite solution of ZnAcD and rinsing with ethanol, the substrates were programmably dip-coated into the concentrated ethanolic solution. The substrates were integrated into a controlled vertical displacement stage that slowly immersed the substrate into the aqeuous solution. After letting the solution settle for 3 minutes, the substrates were slowly pulled out at a dipping

speed of 5 mm·min¯1. Dip-coating was performed five times total after which the substrates were annealed at 210°C for 20 minutes in air and submerged into the nanowire-growth solution for 36 hours. The resulting nanowire arrays were highly oriented (Fig.2.18) and the average diameter of the nanowires was 170nm±40 with average lengths of 11μm. The alternate seeding strategy produced similar results with metal-coated Kapton (PI) and Mylar (PET).

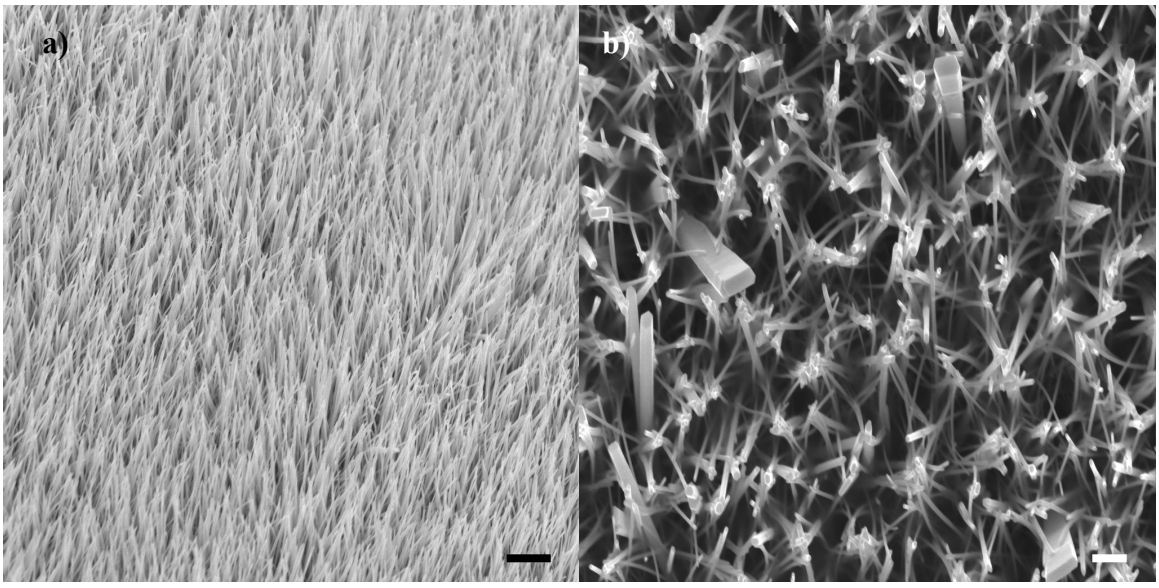


Figure 2.18: Optimized oriented growth on flexible substrates. a) SEM image of nanowires at 45° tilt showing improvement in orientation on Cr/Au coated PDMS substrate by alternate seeding strategy. Scale bar is 2μm. b) Bird's eye SEM image of nanowires grown from dip-coated seeds on Cr/Au coated PDMS substrate. Scale bar is 1μm.

### 2.3.8 ORIENTED GROWTH ON RELIEF PATTERNED FLEXIBLE SUBSTRATES

Chapter 3 of this dissertation will further detail the rationale for producing nanowire arrays on wavy thin metal films on a soft substrate. Herein the method for producing wrinkled thin metal films—typically 50-70nm-thick layers of gold or nickel with a 3-10nm adhesion interlayer of titanium or chromium—is described as well as a

strategy for growing oriented nanowires on them. Thin metal films were deposited onto PDMS by electron beam (e-beam) evaporation (Fig.2.19a). The e-beam heated the metal sources and the heat reached the PDMS, causing it to expand. The metals were deposited on the expanded PDMS; where a typical film comprised 50Å of titanium or chromium evaporated at 0.1-0.5Å·$s^{-1}$, followed by 500Å of gold or nickel evaporated at 3Å·$s^{-1}$. After evaporation of the metal, the PDMS cooled and contracted; inducing waves to form on the surface. The 'waves' or 'wrinkles' result from redistribution, by buckling, of compressive stresses that develop in the surface of the sample on cooling from the evaporator temperature to ambient.

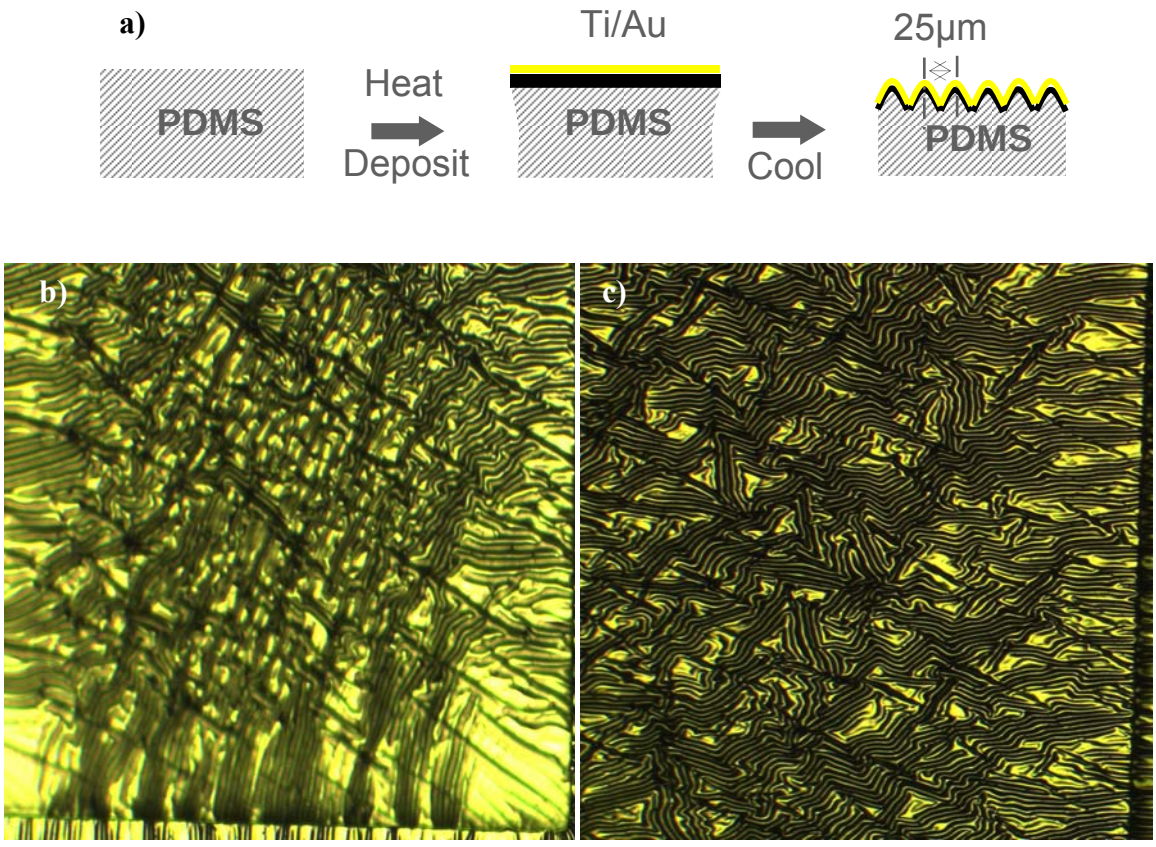

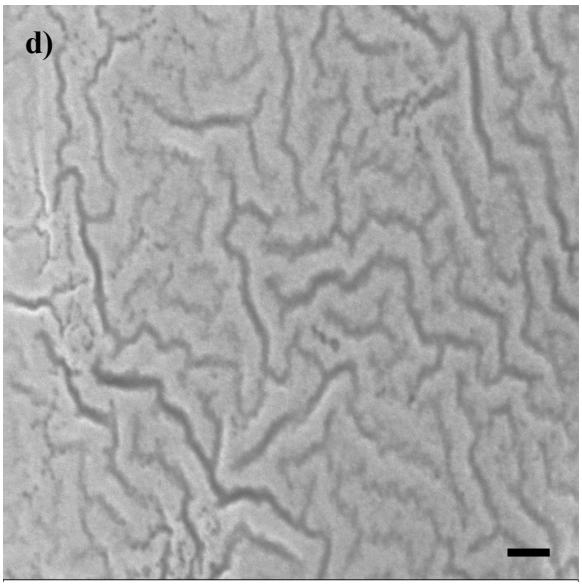


Figure 2.19: Preparation of disordered metal films on PDMS. a) A slab of PDMS was adhered to a glass slide and loaded into an electron beam evaporator. The e-beam heated the metal sources and the heat reached the PDMS, causing it to expand. The metals were deposited on the expanded PDMS; a typical film comprised 50Å of titanium or chromium evaporated at 0.1-0.5Å·$s^{-1}$, followed by 500Å of gold or nickel evaporated at 3Å·$s^{-1}$. After evaporation of the metal, the PDMS cooled and contracted; inducing disordered wrinkles to form on the surface. b) & c) Optical micrographs of disordered wavy films of Ti/Au on PDMS slabs. d) SEM image of disordered waves on PDMS slab. Scale bar is 1μm.

The spontaneously formed disordered wavy films generally have an array of periods and amplitudes that is defined by the moduli of the materials and thicknesses of the metal films, which offers little control over the geometries or phases of the waves. The orientation and amplitude of the waves was controlled by evaporating the metal film onto PDMS that has a bas-relief pattern on its surface[92]; which were created by cast-moulding PDMS against a 2–20μm thick patterned photoresist layer (Fig.2.20a). After patterning a clean Si wafer with optical lithography, the Si wafer was treated with a silanizing agent to prevent sticking by exposure to the vapor of $CF_3(CF_2)_6(CH_2)_2SiCl_3$ for ~30 min. Once the silicon rubber base (vinyl-terminated PDMS, Sylgard Dow 184) was

mixed with the curing agent in a 10:1 ratio, poured over the master, degassed and heated to elevated temperatures (110°C), the liquid mixture becomes a solid, cross-linked elastomer in an hour. The substrates are then further annealed above 100°C for one hour to thermally expand the material before loading into the e-beam evaporator chamber. The metal is then deposited as before, which after removal from the chamber the surface looks 'frosted'. Figure 2.20c-d demonstrate how patterned rectangular ridges (150μm wide x 2cm long x 10–40μm high) aligned the waves parallel to the direction of the raised portions of the PDMS. Generally, the ordered waves have amplitudes of 5μm for 50nm films (10μm for 70nm films) and ~30μm periods. On the recessed regions between the ridges, disordered wrinkles were commonly found as there were no edges or steps to induce directional buckling. However, the waves began to exhibit ordering near the edge or near the ridge. Films with thicknesses greater than 100nm cracked rather than buckled due to elevated stresses from higher degrees of thermal expansion. When two relief patterns intersect, the wrinkles become slightly disoriented (Figure 2.20e-f circled regions), similar to regions on flat PDMS, where the waves are disordered. However, the ordering is reformed less than ten microns away from the disorganized areas. The wavy structures deposited with chromium as the adhesion layer were similar to those formed in the wrinkling of skin[93] because the metal film remains firmly attached to the PDMS, as to where films deposited with Ti as the adhesion layer do not remain in conformal contact everywhere with the PDMS (Fig.2.20h). Chromium tends to be more malleable than titanium, and in turn offer better adhesion and less likelihood to initiate fracture.

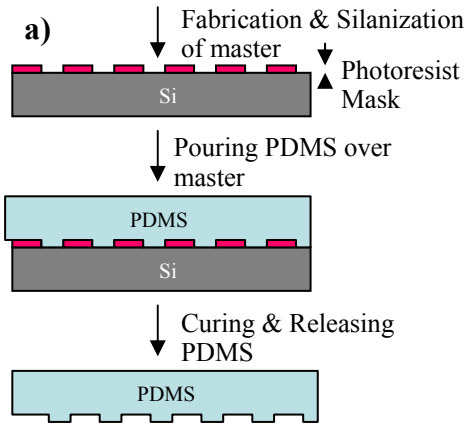
a)
Fabrication & Silanization of master
Photoresist Mask
Si
Pouring PDMS over master
PDMS
Si
Curing & Releasing PDMS
PDMS

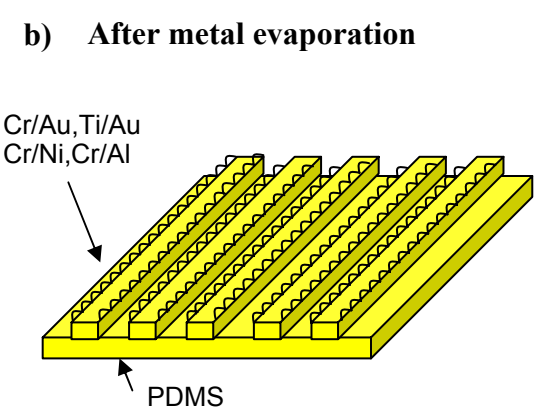
b) After metal evaporation
Cr/Au,Ti/Au
Cr/Ni,Cr/Al
PDMS

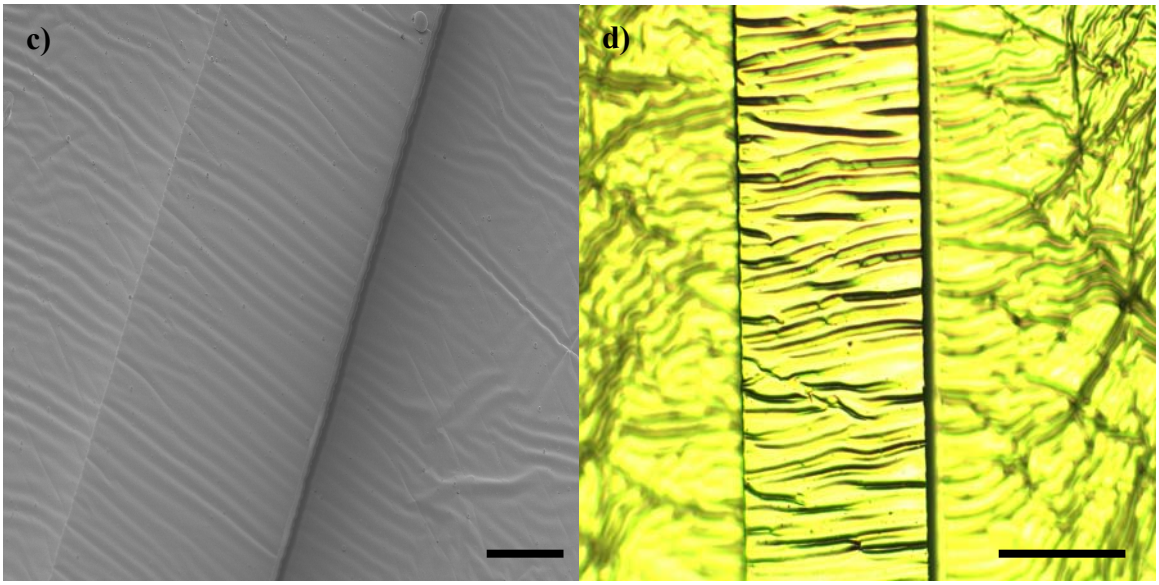
c)
d)

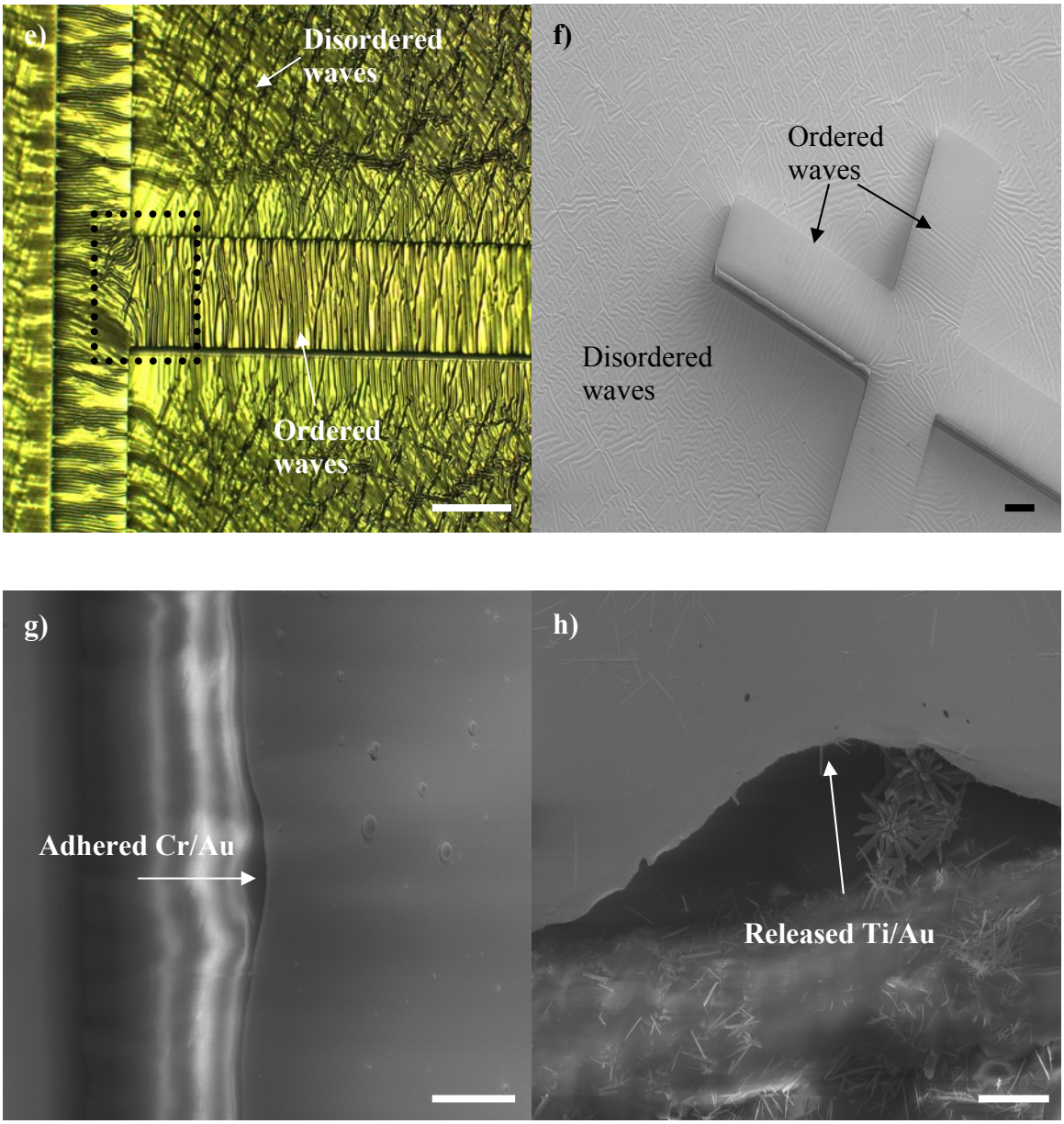
e)
Disordered waves
Ordered waves
f)
Ordered waves
Disordered waves
g)
Adhered Cr/Au
h)
Released Ti/Au

Figure 2.20: Preparation of wrinkled metal films on patterned PDMS. a) Process flow for creating bas-relief patterns on a PDMS surface. The thickness of the relief could be varied by tuning the thickness of the resist (SU-8, Microchem). The Si wafer was typically treated with a silanizing agent, after which the silicone was casted, cured and removed. After the fabricated stamp was created, the slab was annealed at 100°C for one hour and loaded into the e-beam chamber, where metals were deposited. Upon removal and cooling, the waves on the relief were highly ordered with similar wave amplitudes and periodicity. b) Schematic of waves deposited on bas relief-patterned PDMS. c) Magnified SEM image at 45° tilt of metal wrinkles showing ordered periodicity on relief and disorder on flat metal. Scale bar is 100μm. d) Magnified optical micrograph of Ti/Au on PDMS with relief pattern. The scale bar is 100μm. e) Optical micrograph of ordered waves of Ti/Au on PDMS where two relief patterns intersect. The waves on the raised regions are highly oriented as to where the flat regions are disordered. The scale bar is 150μm. f) SEM image at 45° tilt of wrinkles where two relief patterns meet (cross). The wrinkles on the cross are oriented perpendicular to the edge everywhere except the middle region. Scale bar is 100μm. g) Magnified SEM image at 45° tilt of metal wrinkle firmly attached to PDMS. The scale bar is 10μm. h) Magnified SEM image at 45° tilt of buckled metal wrinkle detached from underlying PDMS substrate. The scale bar is 10μm.

The wavy metal-coated substrates were then seeded using the procedure outlined in 2.3.7. However, annealing the substrates at 210°C caused too much thermal expansion of the underlying PDMS substrate and the wavy metal films to crack. Since 'cracking' would isolate arrays of nanowires (Figure 2.21a) or prevent them from contributing to the energy generated, a slightly different seeding strategy was employed. Preformed nanoplatelets produced using the procedure outlined in section 2.2.2 were diluted (5-10%) and dispersed into ethanol. Patterned substrates were programmably dip-coated into the solution using the same parameters as 2.3.7. Between subsequent coatings, the substrates were blown dry and after five coatings, the substrates were annealed at 125°C for 5 minutes in air. After seeding, the substrates were submerged into the growth solution for 36 hours, and cleaned thoroughly. Figure 2.21a depicts a substrate with e-

beam evaporated Ti/Au (5nm/55nm) that was dip-coated with preformed nanoplatelets and immersed in growth solution for 36 hours. The wrinkles remained in tact after the tempered growth and washing cycles and the nanowires were extremely dense and oriented perpendicular to the waves. The coverage of the nanowire array on the side walls where PDMS was not coated with metal was poor, primarily because of the increased surface energy of pristine PDMS.

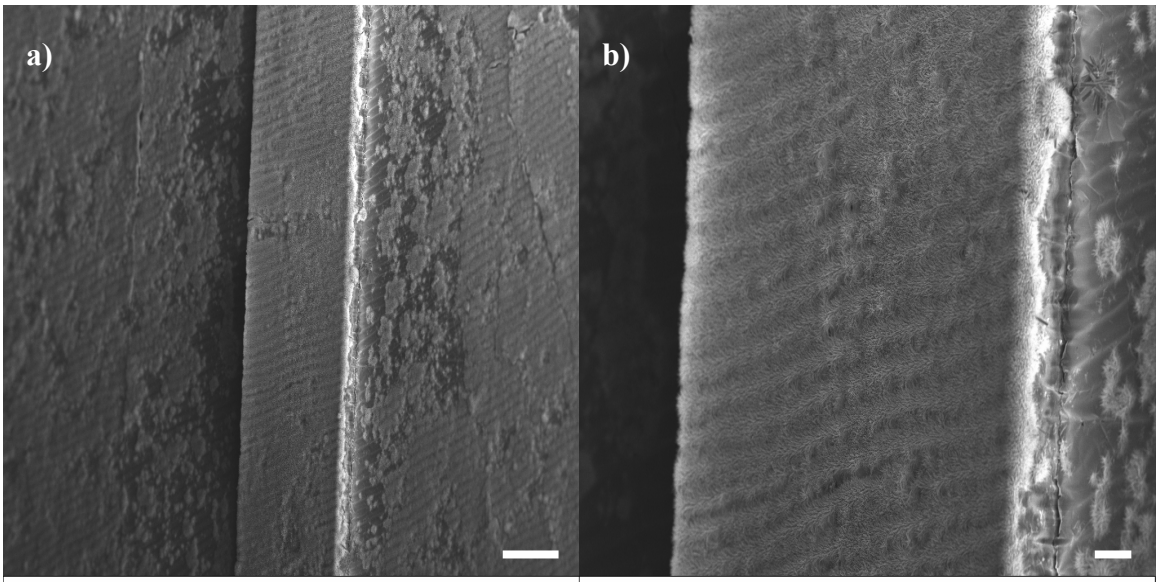

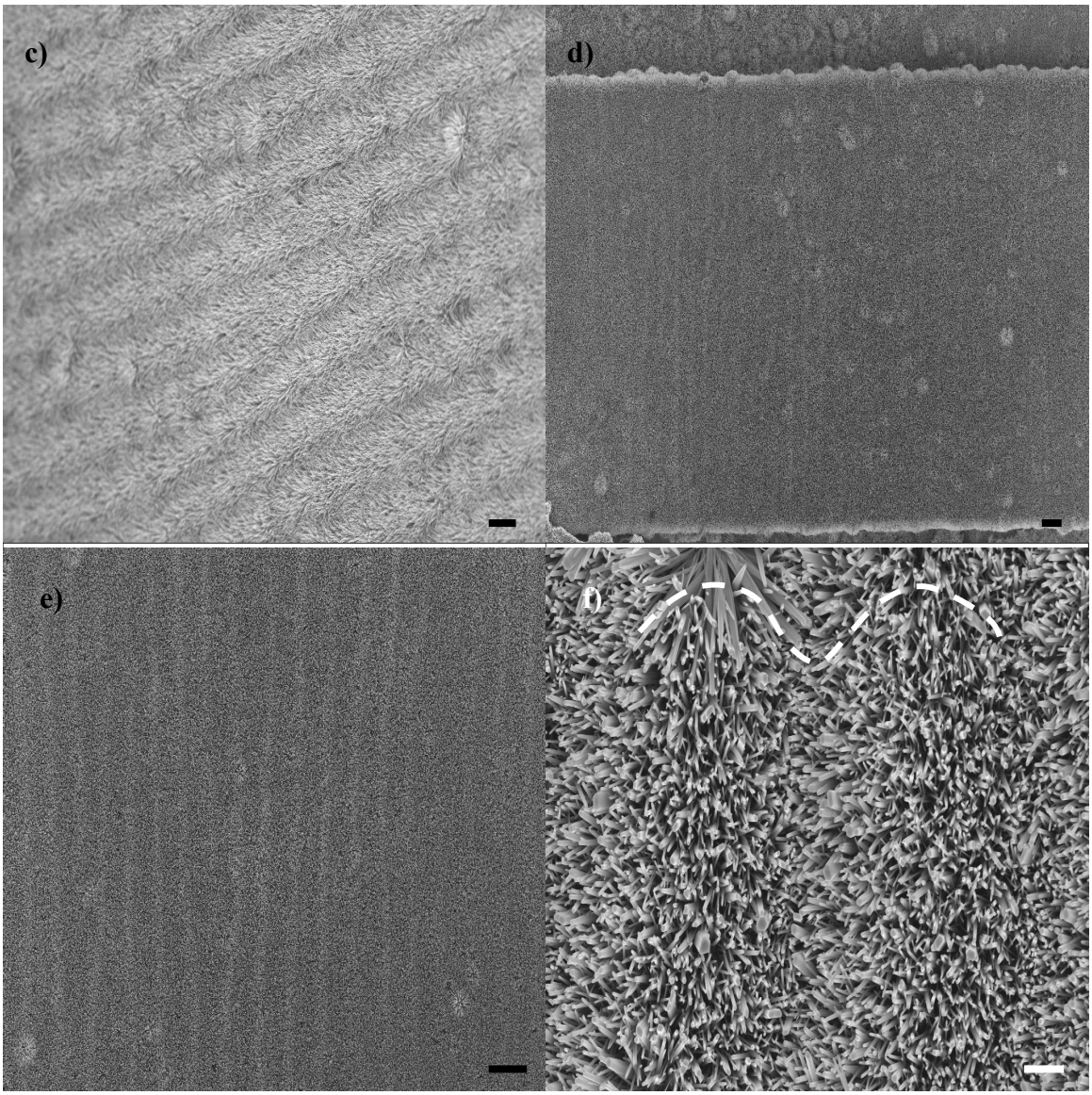
c)
d)
e)
f)

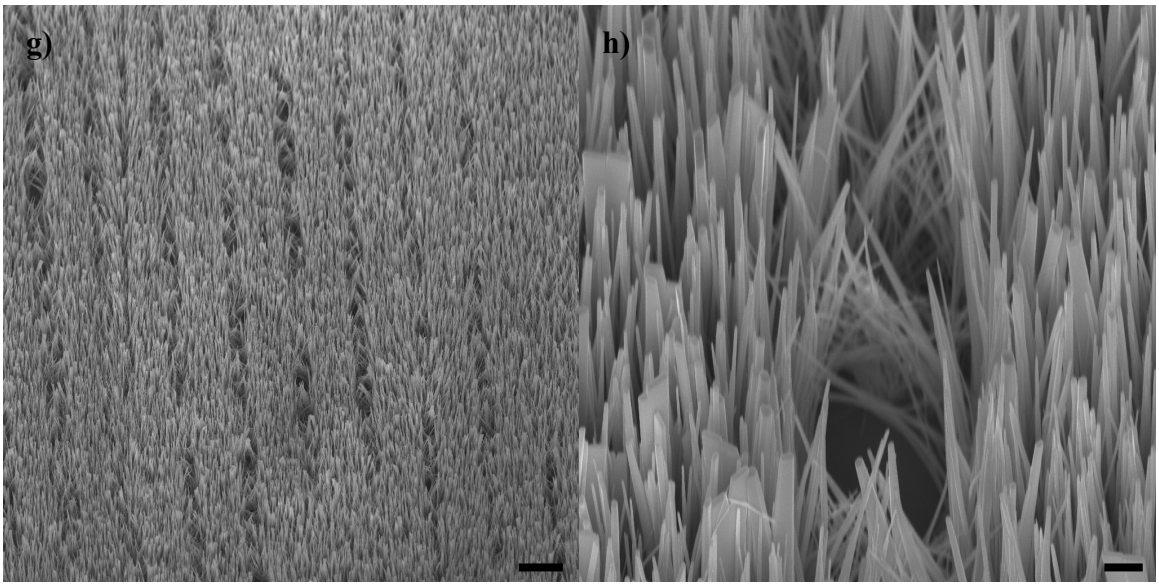


Figure 2.21: Growth of highly oriented nanowire arrays on wavy metal films. a) SEM image at 45° tilt of nanowire arrays grown on a wavy metal film. The array is dense and highly oriented perpendicular to the waves on the relief pattern. The scale bar is 100μm. b) Magnified SEM image at 45° tilt of nanowire arrays grown on a wavy metal film. Note how the array is incomplete near the wall where no metal is evaporated. The scale bar is 20μm. c) Higher magnification SEM image at 45° tilt of nanowire arrays grown on a wavy metal film. The periodicity of the underlying wavy metal film can clearly be seen. The scale bar is 10μm. d) Far-field SEM image of nanowires grown on relief pattern, showing how few 'firecracker' shapes are present, indicating little to no stacking of the nanoplatelets seeds. The scale bar is 20μm. e) Higher magnification SEM image of nanowire arrays grown on a wavy metal film, clearly demonstrating metal film has retained its shape during growth and washing. The scale bar is 20μm. f) High magnification SEM image of nanowire arrays grown on a wavy metal film. The nanowires are strongly oriented perpendicular to the wavy metal film and densely packed. Wavy guidelines are indicated to help identify the nature of the film underneath. The scale bar is 2μm. g) SEM image at 40° tilt of nanowire arrays grown on a wavy Cr/Ni metal film. The scale bar is 10μm. h) Magnified SEM image at 40° tilt of area between neighboring waves and how nanowires grown perpendicular to the surface, even on a wavy metal film. The scale bar is 1μm.

## 2.4 CONCLUSIONS

A general two-step 'wet' synthetic strategy for producing highly oriented nanowire arrays of ZnO on various substrates was developed. In each step, the experimental conditions were optimized to control the size, orientation and population density for a nanowire array that would produce the max amount of energy. The developed approach was based on a controlled nucleation and growth process where the influence of the catalyst (shape, size and orientation), substrate (inorganic (Si, glass) or organic (PI, PET, PDMS) and surface topography) and reaction conditions (precursor type and concentration, point of insertion, temperature, growth time, pH) were systematically optimized. The primary advantage of the approach over other types of growth is the enhanced control imparted by separating nanowire nucleation and oriented growth into two single steps. Characterization of the nanowire arrays with SEM and XRD illustrate the high degree of orientation and high-aspect ratio. TEM images of individual nanowires and Electron Diffraction corroborate lattice constants measured by XRD for hexagonal-wurtzite ZnO. It should be noted that several TEM images showed defects populated the surface and core indicating a highly-crystalline nanowire and not a mono-crystal. The defects found on several nanowires also substantiate some of the results in Chapter 4, where surface defects were discovered using low photon energy Photoelectron Spectroscopy.

Further extension of the growth optimization may lead to even further enhancements of the energy generator. For example, by extending the developed procedure (seed deposition, growth time, solution composition, etc) the oriented nanowires may act as efficient templates for growth of more complex hierarchical architectures such as branched crystallites[94]. Such higher-order crystal structures

produced in multi-stage chemical reactions could yield more deflection and energy production without compromising additions to volume or AICD lead stiffness. Moreover, such a step-wise synthesis could extend to mixed-material systems such as cadmium-sulfide (CdS) or titanium-dioxide ($TiO_2$) nanorods/wires on ZnO crystal cores. Such mixed material super-structures offer both the potential to extract even higher piezoelectric responses and more resistance to fatigue. Additionally, core-shell structures[95] may also offer higher piezoelectric potentials by inducing mismatch strains between the core and shell and also add stiffness to the wires, increasing their lifetimes. Lastly, augmenting solely the growth time may yield hollow microtubes[96] or nanotubes[97], which would act as efficient pathways for higher capacity nanocomposites or templates for composite materials with other piezoelectric nanoparticles adsorbed onto the surface.

# Chapter 3: Integration & Performance of ZnO Nanowires

The piezoelectric activity of individual nanowires has been studied where an atomic force microscope (AFM) probe tip mechanically deflected a single zinc oxide (ZnO) nanowire[42] and the resulted electric response was sensed through the probe tip. The output of the nanowire was ~0.05 fJ in one discharge event. The piezoelectric response of a single barium titanate ($BaTiO_3$) nanowire has also been studied through a miniaturized flexure stage that applies a periodic tensile load[43] and the generated output, which was sixteen times higher than that for ZnO nanowire, was drained off into patterned contacts. Whether nanowire-based piezoelectrics can outperform their bulk counterparts is still unclear. Measurements of ensembles of nanowires actuated simultaneously and continuously need to be obtained, rather than at the single nanowire level, for incorporation of such next generation materials into new, novel energy harvesting devices.

In this chapter both piezoelectric polymeric films and flexible devices incorporating oriented piezoelectric nanowires were studied for use as energy generating devices. The devices were tested on a testbed mimicking the input a failing right ventricle (RV) and the results demonstrate progress towards energy harvesting respectable power outputs from the cardiovascular system. A model was developed to gain insight as to how to structure the nanowire array within the latitude of the synthesis outlined in Chapter 2 to boost the energy production and enhance the lifetime of the device.

## 3.1 COST OF HARVESTING METRIC

The human body stores as much energy in fat as a 1000kg battery, and when the energy is converted into mechanical work via muscle contraction such as running, 100W can be sustained[15,98]. Devices that capture energy from such human movement can be aptly characterized by a cost of harvesting (COH) coefficient, which is a dimensionless quantity that refers to the ratio of the metabolic cost between an exercise with energy harvesting and an exercise in the exact same conditions but without energy harvesting. As an example, devices such as hand crank generators and wind-up flashlights have a large COH because the power generated requires substantial amounts of additional metabolic energy. On the contrary, a piezoelectric insert within the sole of a shoe that harnesses energy from gait[99], or surgically stapled insert to the thorax to harness respiratory expansions[17], has a low COH because little to no extra user effort is required to extract energy. Obtaining a quantitative prediction of the COH from an energy generator in the heart can be measured in two ways, (1) globally as a change in the cardiac output (stroke volume * heart rate) and (2) locally as a change in function of the surface of the heart wall using imaging (MRI or CT), albeit, the volumes and pressures of the cardiac chambers would vary from person to person and over time based on disease. Nevertheless, if an efficient generator can scavenge a fraction of the power output, remove it imperceptibly for a low COH and efficiently store the energy over time, a significant amount of energy can be extracted from the cardiovascular system.

### 3.1.1 GENERATOR LOCATION AND INITIAL MATERIALS SELECTION

The optimal location to couple a generator to the cardiovascular system would be one that would undergo a large deformation and add little to no resistance. The systolic

ventricular mechanics of a failing heart were studied using tagged MRI and showed that the greatest total, longitudinal and tangential displacement of entire cardiac system was found for the RV free wall of the right ventricle (RV)[100]. Since the distribution of strain is relatively uniform for the RV[20], the ideal location to place an energy generator would be the free wall where the max displacement is, which significantly is the site of attachment for an AICD lead. A generator located within a lead can be directly integrated into existing AICD technology without obtrusive interconnects and harness the local RV free wall displacements[21]. Another striking advantage of using the interior of an AICD lead as a location for an energy generator is the device can be protected from body fluids and macrophages, which could potentially degrade or break down the device. Additionally, if the generator or array of generators is small and flexible enough to remain innocuous during systole, the COH would be low. If it becomes practical to further map out an individual's heart fiber directions, the relationship between the strain of the lead and the muscle fiber orientation may be optimized for each individual, which would both increase the power output from the generator and further reduce the COH.

To maintain a low COH, miniature or flexible devices with highly efficient energy conversion factors must be implemented into the AICD lead. Since the most efficient piezoelectric energy conversion devices outlined in Chapter 1 are extremely brittle and rigid, it would take an incredible force to compress the material a small amount. Since energy is defined as force through distance over time, the effective energy generated through cardiac compression would essentially be vanishingly small, even with perfect conversion. In contrast, bending a piece of piezoelectric material like a cantilever to take advantage of its '31' mode is much easier. Because of their brittle nature, piezoceramics such as lead-zirconate-titanate ($Pb(ZrTi)O_3$ or PZT) do not have much

range of motion in this direction and would fracture easily. Thus, such materials are unsuitable for incorporation into an AICD lead, where flexibility is not only necessary but life-critical. Piezoelectric polymers, such as Polyvinylidene Fluoride (PVDF), in contrast, are very flexible, relatively easy to manufacture, and can be subjected to large strain fields without cracking or losing polarization. The cost, however, is that the electromechanical coupling coefficient for PVDF is substantially lower than that for materials such as $BaTiO_3$ or PZT. In order to increase the piezoelectric activity of such a material, multiple layers stacked in parallel must be employed. However, the limited dimension (<1mm) of the interior of an AICD lead restricts the number of layers that can be stacked.

### 3.1.2 PERFORMANCE OF POLYMERIC PIEZOELECTRIC GENERATOR

We conducted an initial experiment using a single film of PVDF (t=28μm) with silver printed electrodes (t=8μm each) and a mylar coating on the upper and lower surfaces of the film (Measurement Specialties Inc.). A test bed was constructed (Figure 3.1) to create a contraction/relaxation motion similar to that of a failing RV[20]. The apparatus includes a servo-motor, a set of transmitting gears, a 4-bar linkage system, and other necessary parts. The frequency of the motion was set to 60 beats per minute and the amplitude of the motion was set to 10mm, the approximate displacement of the apex of a diseased RV[100]. A function generator in the driving system provided a speed profile of the servo-motor to accurately simulate the motion of a failing human RV.

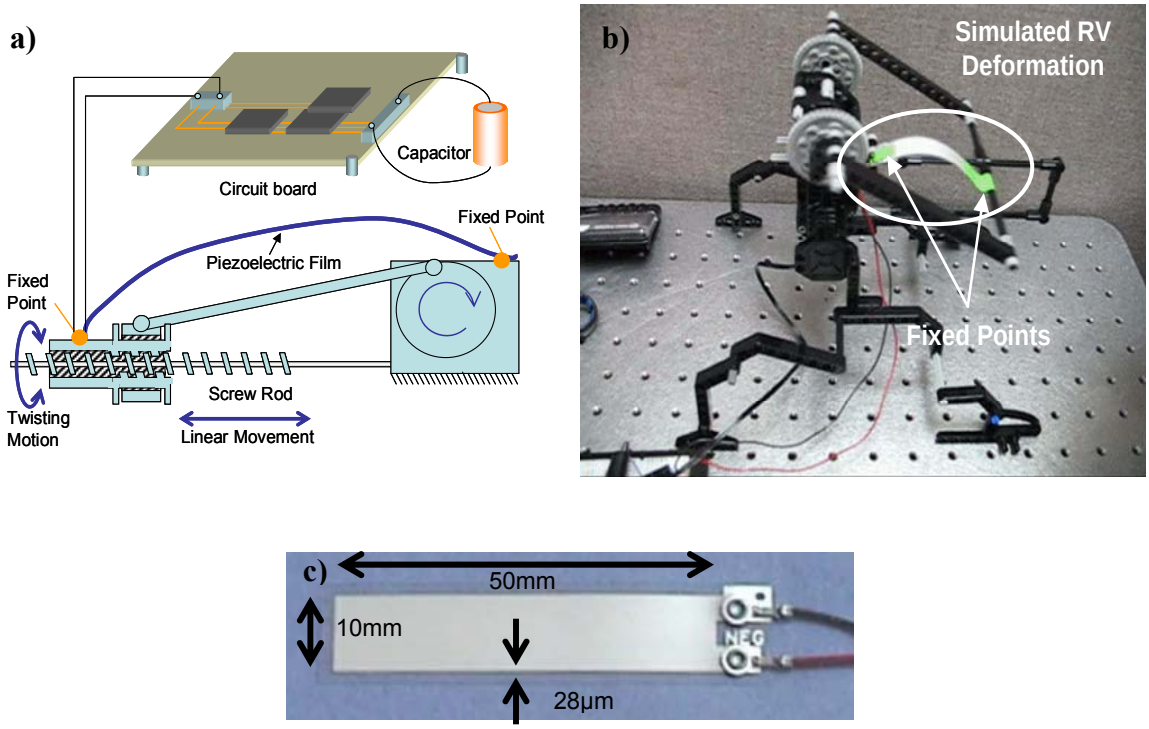


Figure 3.1: Initial experimentation with PVDF. a) Schematic of test-bed mimicking failing RV. The ends of the PVDF film are anchored down to both ends and compressed and twisted just as it would be in systole. b) Photograph of developed testbed showing sliding linkage system and deformed PVDF film. c) Optical image of PVDF film showing dimensions.

A simple integrated circuit was also developed and connected to the printed electrodes to collect the generated charge (Figure 3.2). As the film was stressed through simulated systole, the produced electrical signal was drained off the electrodes into a full wave rectifier. The rectifier transforms the signal from an alternating current (AC) into a direct current (DC). The DC signal was stored on an electrolytic capacitor (33µF), and the potential difference across the capacitor was quantified using an ohmmeter every minute. The voltage difference was converted to a charge via the relation (q=CV) and plotted as a charging rate.

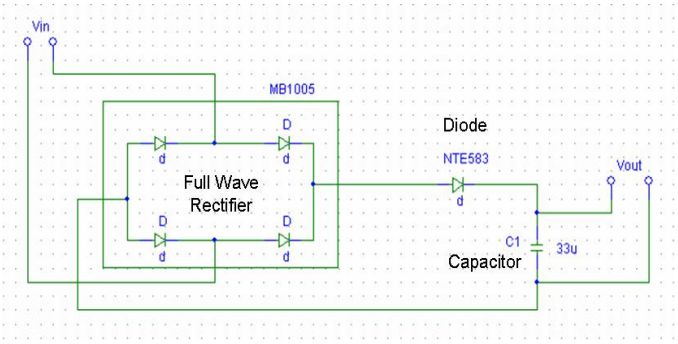


Figure 3.2: Schematic of integrated circuit. The circuit collects, conditions and stores the produced charge from the PVDF film.

As can be seen in Figure 3.3, the rate of charging the capacitor is low. Assuming no losses from the associated circuitry and storage capacitor, it would take a period of ~80 years for a single PVDF film (green curve) to fully charge an AICD battery with approximately 1.0 Amp*Hrs, or 3600 coulombs using the heart's motion. The long charging time can be attributed to the low energy density and the strain developed in the PVDF film. Using larger films (2x length – red curve) or multiple layers in parallel (2 layers bonded together – blue curve) increases the charging rate and reduces the time to recharge a battery from 80 years to ~50 years.

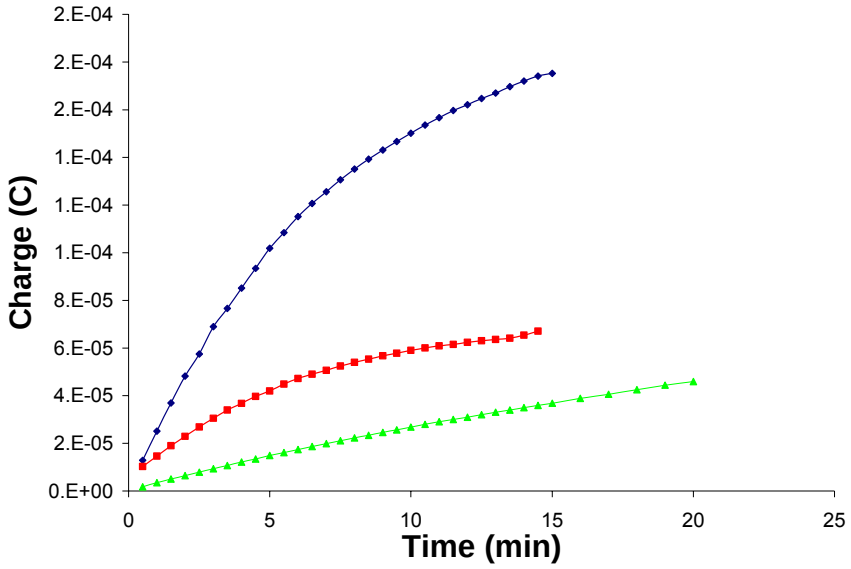


Figure 3.3: Charging rate of PVDF film(s) in simulated systole. The y-axis is the approximate time to fully recharge an AICD battery. The green curve is charge produced from a single film, red is film twice the length and blue is two films in parallel.

### 3.2 METHODS TO IMPROVE PERFORMANCE OF PIEZOELECTRIC GENERATOR

To increase the energy generated from the piezoelectric, several approaches could be taken. The most direct method would be to exchange the PVDF with piezoelectric ceramics that possess larger conversion coefficients. However, as illustrated previously and in Chapter 1 in further detail, thin films of such materials are extremely difficult to implement within an AICD/BVP. Moreover, for the application contemplated here, the mechanical strains needed to accomplish efficient energy generation from such ceramics would inherently have to be higher, indicating larger COH values and greater resistance in systole.

Another approach to increase the energy generated would be to increase the strain experienced by the PVDF and in turn raise the stress and charge density. Since the force and displacement of the RV are fixed variables, the strain on the PVDF can be increased by choosing a shape that would more oppose the bending distribution in the lead. To do so, the evolution of the RV in systole, which dictates the bending distribution in the lead, was studied in further detail. In systole, the RV undergoes a torsional rotation and a linear contraction[101]. Figures 3.4a-b depict x-ray images of an AICD lead in systole, resisting the deformation of the RV by undergoing a twist from the torsion and bending from contraction. The optimal shape to resist such an axial normal stress and cross-sectional shear stress would be a helical spring (similar to a telephone cord) in the lead, as depicted in Figure 3.4 both in c) diastole and in d) systole. A helical coil embedded in the AICD lead opposes the rotational torsion of the lead by a contraction stress (represented as (1) on Figure 3.4e), and resists the linear contraction by a torsional shear stress (represented as (2) on Figure 3.4e). There are two important advantages of a helical spring architecture: 1) the entire length of the active coil in the helix is subjected to torque rather than specific concentrations, and 2) there is an increase in the torsional stress because of the lead curvature (Wahl factor), which can be further increased by tuning the ratio of the coils to the thickness (spring constant)[102].

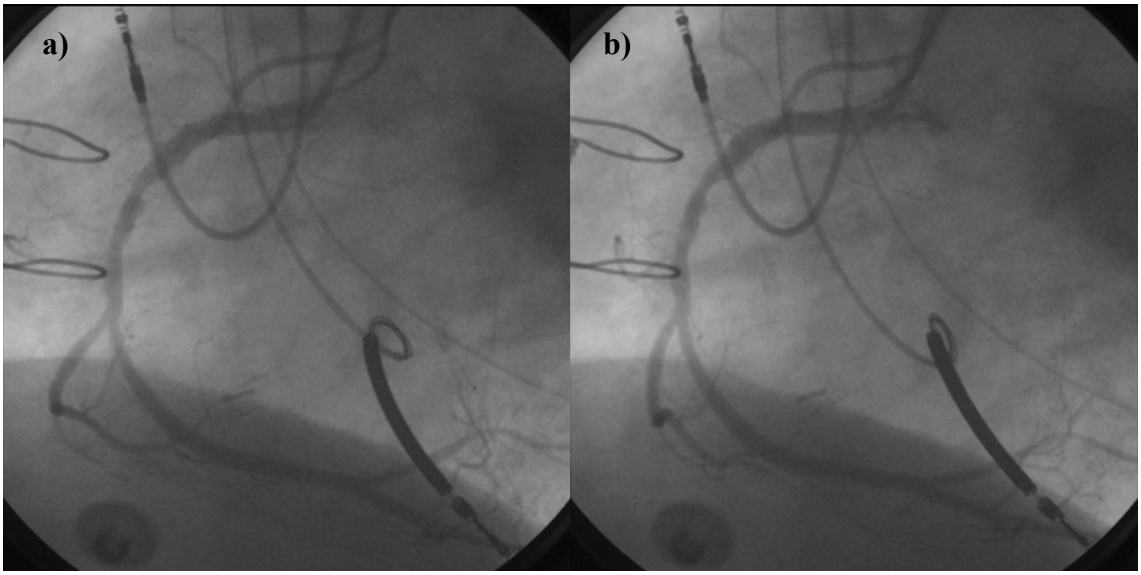
a)
b)

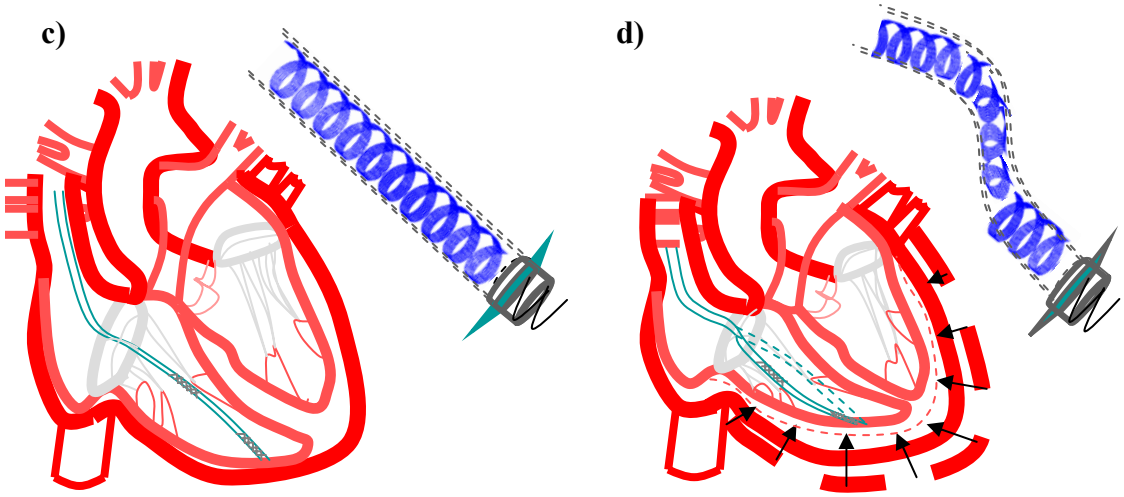
c)
d)

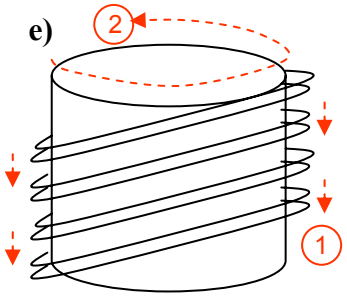
e)
2
1

Figure 3.4: Optimal shape to oppose RV deformation. a) X-Ray images of AICD and BVP leads moving through systole. The heart was injected with dye for clarity. (a) ICD and BVP lead in diastole. (b) ICD and BVP lead in systole. Schematic of optimized shape of PVDF within lead during c) diastole and d) systole. e) Stresses encountered within the coil structure during systole. The radial compression of the RV causes a compression of the coil (force 1), which is opposed by a rotational torsion in the material. The torsion of the lead during systole also induces a

The commercial AICD lead was dissected to choose the best possible location for the helical coil generator. A commercial AICD lead body contains one shocking conductor (diameter = 1 mm), which is made of drawn brazed strand cable, for defibrillation. The shocking conductor is coated with PTFE insulation and the PTFE is insulated with a thin layer of silicone, followed by another electrical isolation layer to protect the conductor from the rest of the lead body. Another insulation layer of silicone protects the electrical isolation for a total thickness of approximately 3mm. The thickness for each layer is: 0.4mm for the exterior silicone insulation layer; 0.02mm for the electrical isolation layer; and 0.25mm for the interior silicone insulation layer. Since the max tensile and compressive stresses occur at the outer surface in the exterior silicone insulation layer[103], it would be the optimal location to place the coil. Given the finite dimension of the insulation space (~400μm), and the thickness of a single electroded film of PVDF (~40μm), several layers of the material can be stacked together in parallel without large additions to the COH. According to Hooke's law, to further increase the stress on the coil, the pitch of the coil can also be increased.

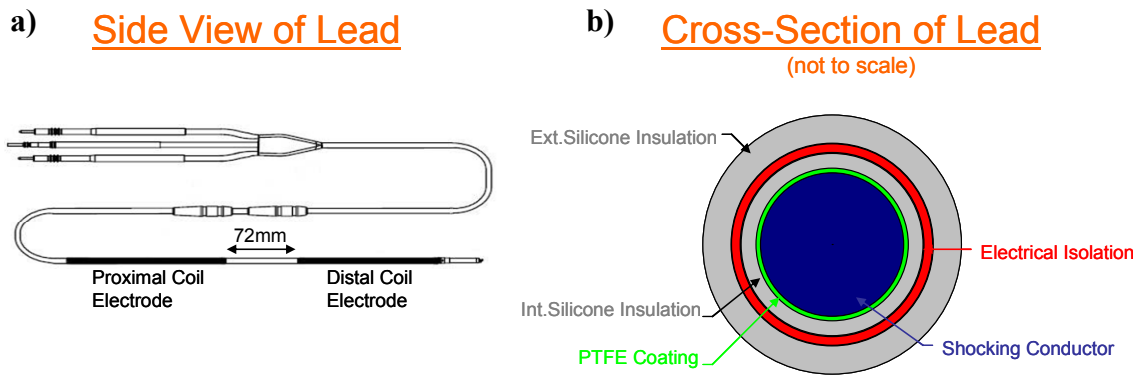


Figure 3.5: Proposed location for helical coiled generator. a) Side view schematic of a commercial AICD lead (image courtesy of Medtronic). b) Cross-sectional view of lead showing various layers and space in the external insulation for the proposed generator design.

Convolving the PVDF into a coil and optimizing its thickness and pitch would increase the energy production but the generator would still be limited by the low coupling factor of the material. Therefore, to raise the energy density without compromising the COH, inorganic piezoelectric nanowires were used in a flexible device and embedded in a polymer matrix. The strength and toughness properties of the nanowires are improved with a surrounding polymer[104] and provide a path for efficient load transfer through and around the wires, which aids to prevent a fracture in one area of the device from propagating to adjacent areas. Energy harvesters incorporating piezoelectric nanowires have been recently investigated but the design necessitated the use of inflexible sawtooth-shaped electrodes[19] as well as high frequency mechanical excitations. The sawtooth design limits the amount of energy that can be harvested because it focuses the energy output through a single point contact. This in turn increases the contact resistance as well as causes a "clamping" effect, which produces inhomogenous electric fields in the nanowires that are smaller and in turn less energy can

be scavenged[105]. Moreover, the frequencies needed for operation of this type of generator were too high and the size would be too big to incorporate into an AICD lead. This dissertation focused on using the energy generating mechanism of the ultrasonic nanogenerator[19] but in a different, novel platform that could simultaneously operate with a low COH and be integrated within a conventional AICD lead. Two generations of devices were fabricated on plastic and mechanically deflected using a testbed that mimicked a failing RV.

### 3.3 1ST GENERATION NANOSTRUCTURED PIEZOELECTRIC DEVICE

The first generation device was constructed on a thin polyimide (PI) substrate. A PI substrate (25 μm thickness, Kapton HN, Dupont) was treated with a short oxygen plasma (March Plasma CS1701F RIE etching system, 20sccm $O_2$, 50W, 20 seconds) to clean the surface. The plastic pieces were then sonicated in acetone and isopropanol, rinsed with deionized (DI) water thoroughly and dried with a stream of nitrogen. A positive photoresist (AZ5209E, Microchem) was spun-cast at 3000rpm (Spincoater, Laurell Technologies) onto the plastic substrate and soft-baked at 95°C to evaporate the solvent and densify the film. The substrate was then exposed to UV light for 3-5 seconds through a transparency mask on a mask aligner (Suss MA6 mask aligner). After exposure, the substrate was immersed in developer (AZ326MIF, Microchem) and gently agitated for 1 minute. The substrate was then rinsed with DI water, blown dry with nitrogen and hard-baked at 95°C for 1 minute to cross link the exposed resist. The substrate was then loaded into a thermal evaporation chamber (Denton) and 8nm of chromium (Cr) was deposited first as an adhesion layer at 0.1Å/s, followed by 50nm of gold (Au) at 1Å/s. After metal evaporation, the substrate tended to bow due to the offset of the neutral plane. To keep the substrate from bending, 40nm of silicon dioxide ($SiO_2$)

was deposited on the backside of the PI using plasma enhanced chemical vapour deposition (PECVD) (Oxford Instruments Plasma Lab 80+). After deposition, the substrate was immersed into warm acetone for fifty minutes and sonicated for 10 minutes in acetone to liftoff the resist. After liftoff, the device was cleansed with isopropanol, rinsed with DI water, dried with an air gun and cleaned with oxygen plasma (50W, 30sccm, 60 secs) to remove any residual resist. An individual device contains two sets of eight square base electrodes (Figure 3.6b), each of which is connected to a large interconnect that can be accessed externally. The device also contains two interconnects for the top electrode that are also connected to a large interconnect. Poly ethyleneterepthalate (PET or Mylar) substrates (100µm thickness, Grafix Plastics) and different grades of Kapton (VN, FPC, V, E, Dupont) have also been used as substrates.

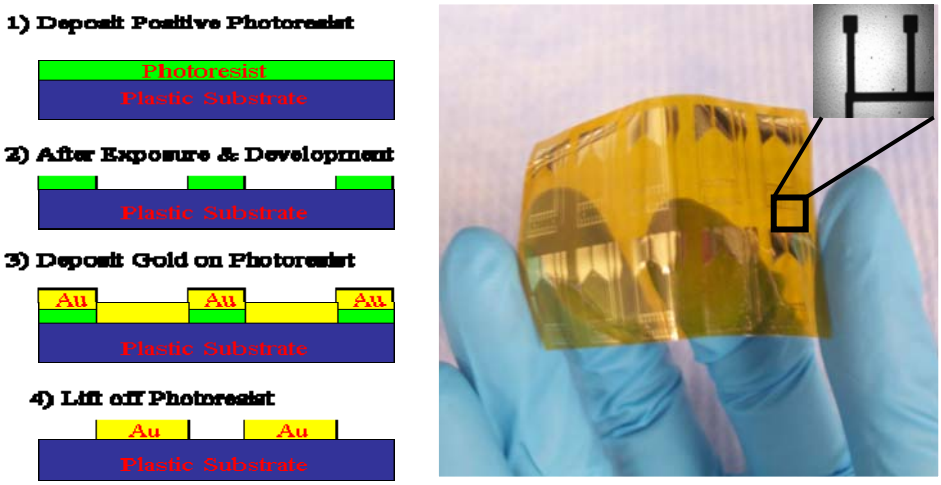


Figure 3.6: 1st-generation device substrate. a) Liftoff process for creating devices on plastic substrate. b) Devices batch fabricated on plastic PI substrates (inset is magnified optical image of internal Au contact pads).

Once the devices were cleaned after liftoff, the interconnects on the device were covered using scotch tape, and textured seeds created in-situ were formed on the exposed

contact pads and neighboring areas. After seeding, the tape masks were removed and oxygen plasma (30W, 30sccm $O_2$, 30 secs) was used to clean the device. Nanowires were grown from the catalyst sites using the procedure outlined in Chapter 2. After growth, the substrate was rinsed thoroughly with DI water, cleaned with UV/Ozone for five minutes and baked overnight in air at 125°C to remove residual organics deposited from solution. In order to anchor the nanowires to the contact pads and prevent potential short circuits due to pinholes in the nanowire array when the top electrode is introduced, a polymer layer was grafted onto the nanowires. The polymer layer secures the nanowires to the bottom contact electrodes and provides mechanical stability to the array. Since ZnO is a hydrophilic surface, mating a hydrophobic polymer required the use of an adhesion promoter. The molecular layer of the adhesion promoter adjusts the two surface energies to help form a stronger interface between the nanowires and surrounding polymer and assist in the distribution of the loads between the nanowires and polymer. An adhesion promoter (Hexamethyldisilazane (HMDS) or AP150, Silicon Resources Inc.) was applied to the nanowires by drop casting several drops onto the arrays, spin casting the liquid @ 1000rpm for 1 minute and annealing at 85°C for 1 minute. Scotch tape was then placed over the interconnects again and a solution of monomer (Methyl Methacrylate, Sigma-Aldrich) and photoinitiator (Irgacure 651, Ciba) was dropped onto the array. The device was then degassed to remove any trapped air and photopolymerized using ultraviolet light for 30 seconds. The device was heated again at 90°C for five minutes to fully cure the polymer and then etched with oxygen plasma (50W, 30sccm, 30 seconds) to expose the tops of the arrays (Fig. 3.7). The process was repeated until the gaps between the nanowires were filled with polymer and the nanowires were fully exposed and protruding several microns.

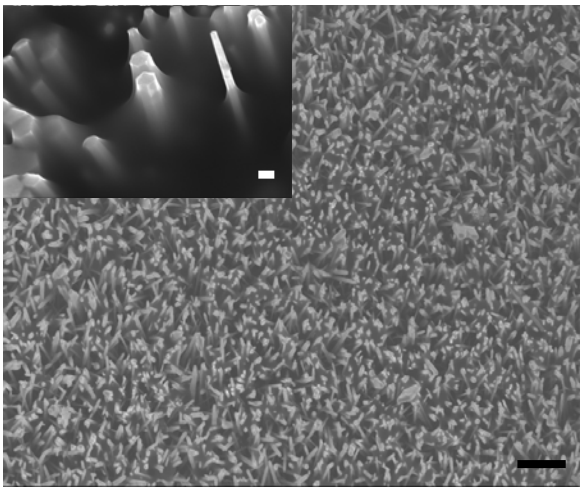

Figure 3.7: SEM image of nanowires extending from grafted polymer layer. Scale bar is 2μm. Inset is high magnification SEM image at 45° tilt of several nanowires projecting out from polymer. Scale bar is 200nm.

A flexible silver-based conducting epoxy (101-42, Creative Materials) is cast over the nanowire tips to provide the top electrode and cured for 5 minutes at 93°C. A liquid polyimide (PI-2770, HD Microsystems) is then drop-casted through a 30G needle over the conducting epoxy, developed with UV light for 2 minutes, and post-cured at 100°C for six minutes (Fig. 3.8). The wires were good conductors along the direction of the wire axes, forming excellent electrical junctions with the neighboring contacts. Two-point current-voltage (I-V) measurements of the devices showed Schottky traces (Fig. 3.8c).

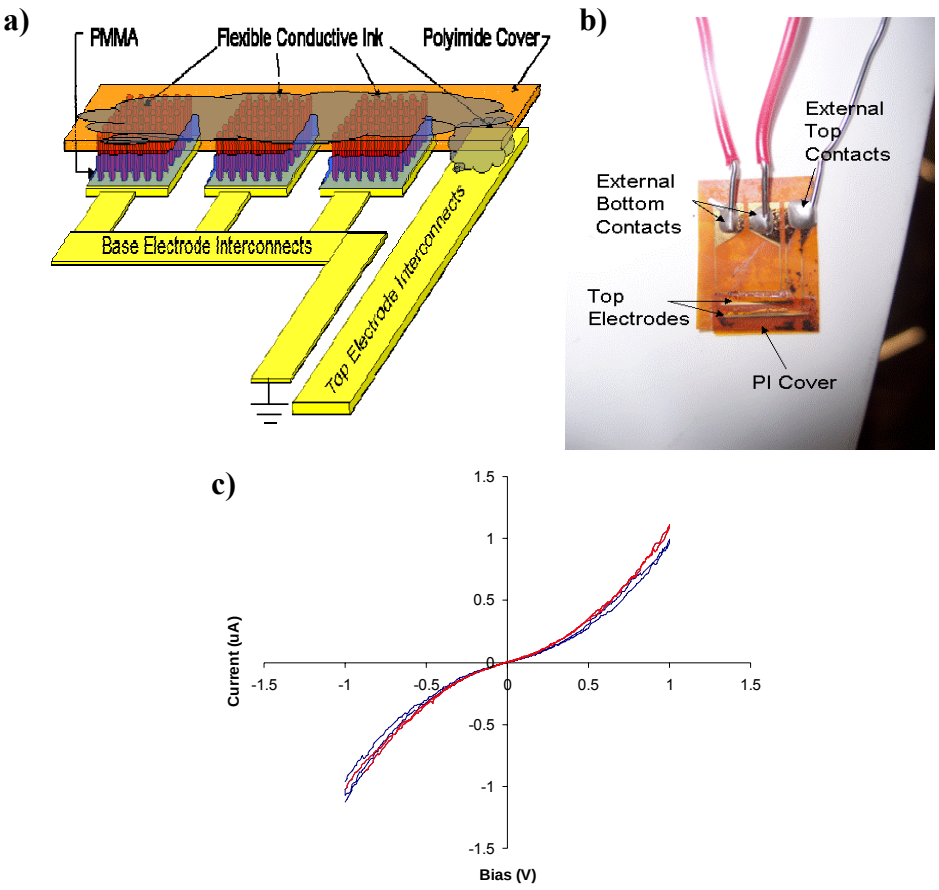


Figure 3.8: Completed device characteristics. a) Schematic of device after nanowire growth, polymer grafting, attachment of contacts and polyimide covering. b) Photograph of an assembled device after external silver wire has been connected with conducting silver epoxy. c) Typical two-point electrical measurement of a finished device.

The devices were then integrated into a testbed that recreated the approximate internal stress environment of an AICD lead in systole. Since the substrates were anticipated to be wrapped around and incorporated within AICDs (Fig 3.9a), the testbed was modified to re-create the sustained stresses and bending radii that would be observed in systole. The testbed consisted of a soft curved strut of PDMS (radius of curvature of ~5mm) rigidly connected to a motorized piezoelectric stage. The device was suspended

over a fixed support and constrained on its edges. The strut was slowly brought into contact from the backside of the substrate until it conformed to the curvature of the PDMS strut. When the substrate was flat, the nanowires were vertically oriented (Figure 3.9c). When the substrate was distorted, the outer portion was pulled into tension and inner segment was pushed in compression due to the different radii of curvature. Since the polymer-embedded nanowires were above the neutral plane and rigidly attached to the substrate, the nanowires were forced to bend rather than remain upright and carry the compressive load of the tensile stress of the surrounding polymer. This effect is because the stiffness of thin beams is much less in bending than in compression. The mechanical deformation of the individual nanowires produces an internal strain field, with the stretched outer surface in tension and inner surface in compression. The strain field across the nanowire produces a potential difference ($\Delta V$) through the direct piezoelectric effect, with the tensile side possessing a positive voltage and the compressed side of the nanowire possessing a negative voltage. Since the contact and nanowires are touching, the interface between the compressed side of the nanowire and contact is a forward-biased Schottky diode. If the potential is large enough to overcome the diode, a current output should be seen from the $\Delta V$-driven flow of electrons from the ZnO nanowire to the metal. The produced current should be able to flow through the nanowire and stabilize the potential distribution. This would represent the discharge process or energy generated. In the case of the nanowires previously not in contact with the top electrode because of height or angle variations, a unique discharge process occurs which is similar to the ultrasonic generator[19]. As the nanowires in contact with the top electrode bend and the top electrode approaches the base of the nanowires, nanowires previously not in contact with the top electrode may now touch the top electrode. Since the nanowires are distorted and possess a built-up potential, when the compressed side contacts the

electrode, the forward-biased Schottky barrier permits an output current, similar as before. This discharging process if substantial, may also contribute to the measured energy.

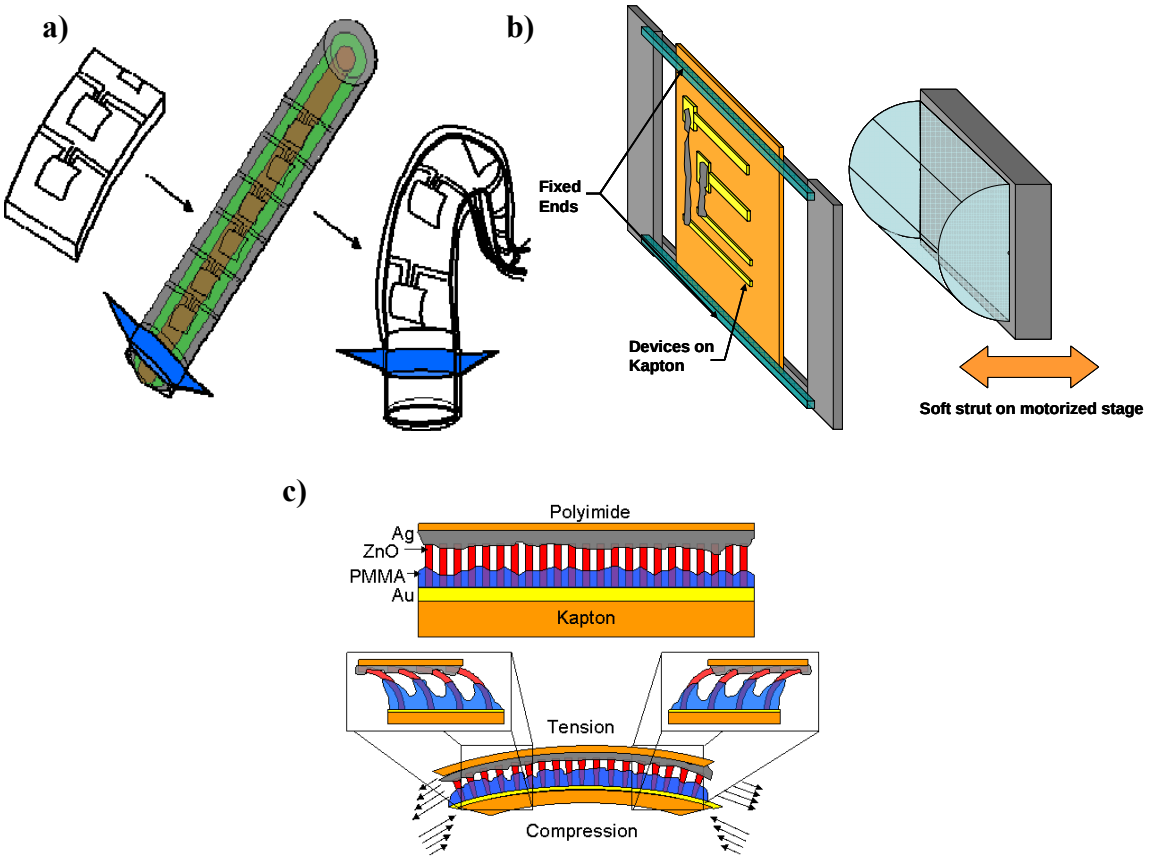


Figure 3.9: Modified testbed. b) Schematic of suspended device fixed at its ends. A curved PDMS strut is brought slowly into contact from the backside until the substrate conformed to its radius of curvature. c) Diagram of nanowires before and during distortion.

Approximately 31 devices were loaded at rate of 1Hz. The electrodes were connected to a low-triboelectric noise BNC cable (Dytran 6013A) that was connected to a voltage pre-amplifier (SR560, Stanford Research Systems), with the bottom electrode

grounded. A homebuilt faraday cage enclosed the test setup and sample to reduce external electric fields and noise. No voltage signal above the noise level was measured from any of the devices. Since the nanowires were connected in parallel, the voltage signal is effectively created by one nanowire. To increase the signal-to-noise ratio, a current pre-amplifier (DL 1211, DL Instruments) was substituted for the voltage pre-amp. Given that the output current is the sum of the individual currents generated from all of the nanowires, the current signal should be larger than the voltage signal. However, no current signal above the noise level was detected for any of the devices. Several reasons were attributed to the devices not producing any measurable output. First, inspection of the surface near the contact pads showed the nanowires repeatedly fractured off of the electrodes as the device was flexed. Since the arrays under the epoxy couldn't be viewed or cross-sectioned without further compromising their state, nanowire arrays that were not electroded or covered with a PI layer but near the area of focus were studied. Figure 3.10a is an SEM image of an array that was severely cracked after a bending test. The magnified view in Figure 3.10b shows the nanowires at the surface were left in tact and well adhered to one another but fractured at their base. The fractured arrays were a primary result of the surface strains that formed from bending. Since the Kapton substrate was less than thirty microns thick, the surface strains withstood were high enough to cause the nanowires to uproot or break off from the substrate (Figure 3.10c-d). There are two primary reasons for this behavior. The first derives from elementary bending mechanics in thin films, where the surface strains are determined by the film thickness, t, divided by twice the radius of curvature associated with bending ($\rho$=5mm). The PI substrate (t = 28μm) can be bent to a radius of ~2mm before the surface strains reach the fracture strain of the nanowires (~2% in tension). For larger bending radii,

rather than fracture, the inorganic nanowires collectively would uproot from the substrate, which is precisely what was observed.

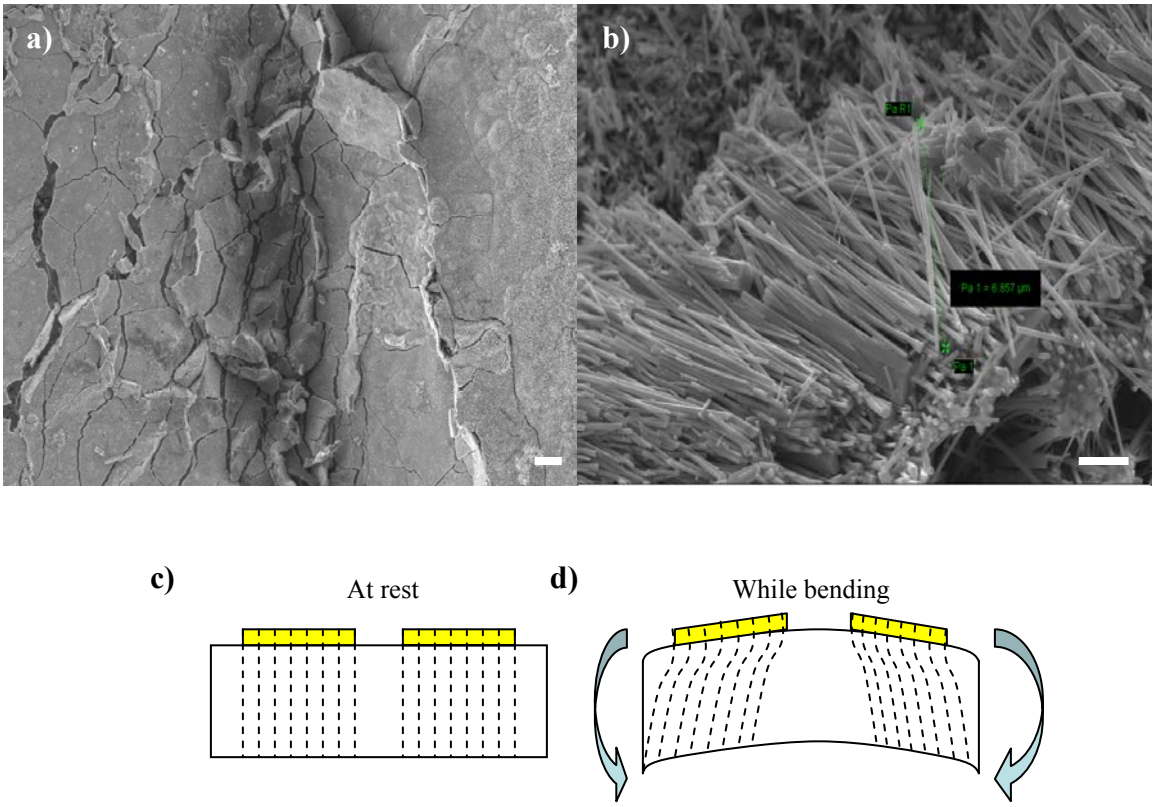


Figure 3.10: SEM images of nanowires fractured from device. a) Far-field image of massively cracked array Scale bar is 30µm. b) Scale bar is 2µm. c) and d) are schematics of the cross sectional strain profiles. The dashed lines are the strain profiles of the polymer substrates during a) rest and b) under deformation. For the case at rest, the strain profiles are straight lines, meaning no strain exists in the material. Under mechanical deformation (defined here as a bending moment creating tension at the top surface and compression at the bottom), the strain profiles are perturbed, especially at the surface. Note the profiles and size of the film are not to scale.

Another limitation of the device design was the limited number of inputs or the size of the active device area. Since each of the sixteen square contact pads (l=150µm)

that the nanowires were grown on represented less than 0.1% of the total device area, a nanowire fracture on the active area basically destroys the device.

### 3.4 2ND GENERATION NANOSTRUCTURED PIEZOELECTRIC DEVICE

To abate the encountered problems, an entirely different device concept was designed and constructed. The device consisted of a sandwich structure that fits together with interlocking pieces (Figure 3.11). One side of the sandwich has ZnO nanowires grown on a wavy metal surface, and the other side is a flat metallized electrode. The two substrates are separated by a thin spacer layer that physically and electrically isolates each side of the device. The device is constructed on thin silicone rubber supports, which can be wrapped around and bonded or incorporated within the lead by dry transfer and subsequent casing.

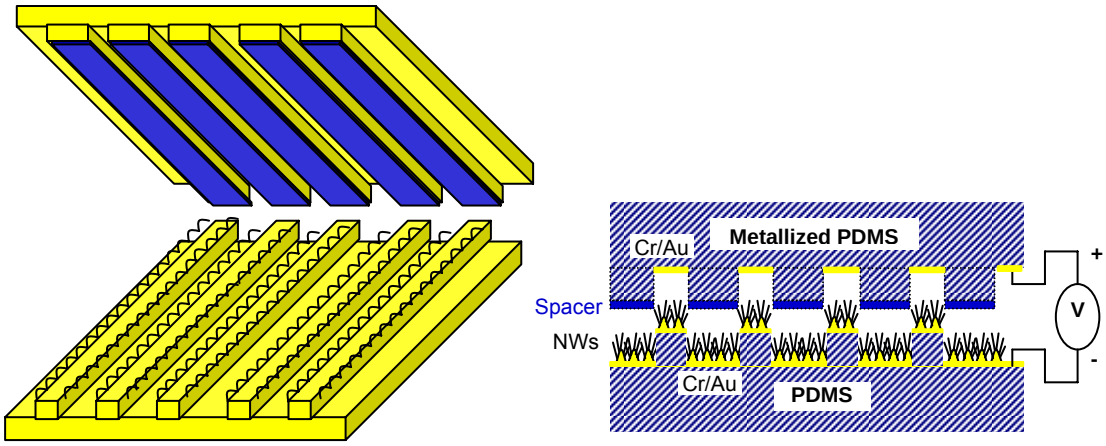


Figure 3.11: 'Sandwich' styled device. a) Angled schematic of sandwich devices. Top device has wider trenches that mesh with the bottom piece. A polymer spacer layer (blue stripes) physically and electrically separates the two pieces from one another and provides a softer interface between the two metal faces. b) Side view schematic of sandwich structure showing wavy metal electrode and nanowires grown on top. The spacer layer (blue) separates the two pieces.

This device architecture has several advantages when compared to the first generation device. First, the nanowires were removed from the surface and the associated surface strains and moved closer to the neutral mechanical plane (NMP). The NMP defines the position through the thickness of the structure where the strains are zero. This situation is highly favorable because it reduces the possibility of fracture or plastic deformation in the nanowires when the device is flexed. Next, to further relieve the strain on the nanowires, the metal base electrode was buckled as it was deposited. Since the silicone support is very compliant (Young's modulus $E_{PDMS}$~500MPa) and the metal film is stiff (Young's modulus $E_{Au}$~100GPa), during the deposition the metal builds a compressive stress between the elastomer and itself, which causes it to wrinkle. The result is a wavy structure or buckled film that resembles aged skin, or a stiff epidermis attached to a soft dermis[93]. The 'waviness' enabled the metal electrode to reversibly change the amplitudes and periods of the wave patterns rather than accommodate the flexural strain, which alleviated the interfacial stress between the electrode and nanowires, where the nanowires were prone to breaking. Finally, the surface offset also helped to strongly order the waves parallel to the direction of the raised portions of the PDMS[92].

To create the sandwich architecture, the process began with a clean Si wafer. The wafer was cleaned with piranha treatment (~3:1 $H_2SO_4$:$H_2O_2$ for 8 min) and $H_2O$ rinsing, washed thoroughly with acetone and isoproponal (IPA) and dried with an air gun. The wafer was then cleaned with oxygen plasma (100 W, 50 sccm $O_2$, 200secs). This plasma treatment removes organic residues and makes the surface hydrophilic. Next, a photoresist (SU-8 2005, Negative Resist, Microchem) was spun-cast at 3000rpm onto the

wafer and soft-baked at 95°C to evaporate the solvent and densify the film. The substrate was then exposed to UV light through a transparency mask for 35 seconds on a mask aligner. Following exposure, the substrate was post-expose baked (PEB) on a hot plate using a two-step ramping procedure. The substrate was first heated at 65°C for 1 minute, then at 95°C for 2 minutes. After PEB, the substrate was immersed in developer (SU-8 Developer, Microchem) and strongly agitated for 1 minute. To assist with agitation, sonication in the developer solution was occasionally used. The substrate was then rinsed briefly with IPA and DI water, blown dry with nitrogen and hard-baked at 150°C for 30 minutes. The formed relief structures are ~6µm tall relative to the wafer surface and have well defined edges (Figure 3.12). To change the height of the relief structures, the spin speed and/or resist with different viscosity (i.e. SU-8 2010, 2025, 2100, etc) can be changed. For the bottom structure, a different mask was used but the resist and procedure was the exact same. The width of the relief patterns on the bottom structure was 50µm thicker on each side so the bottom and top structure would fit together in a conformal fashion.

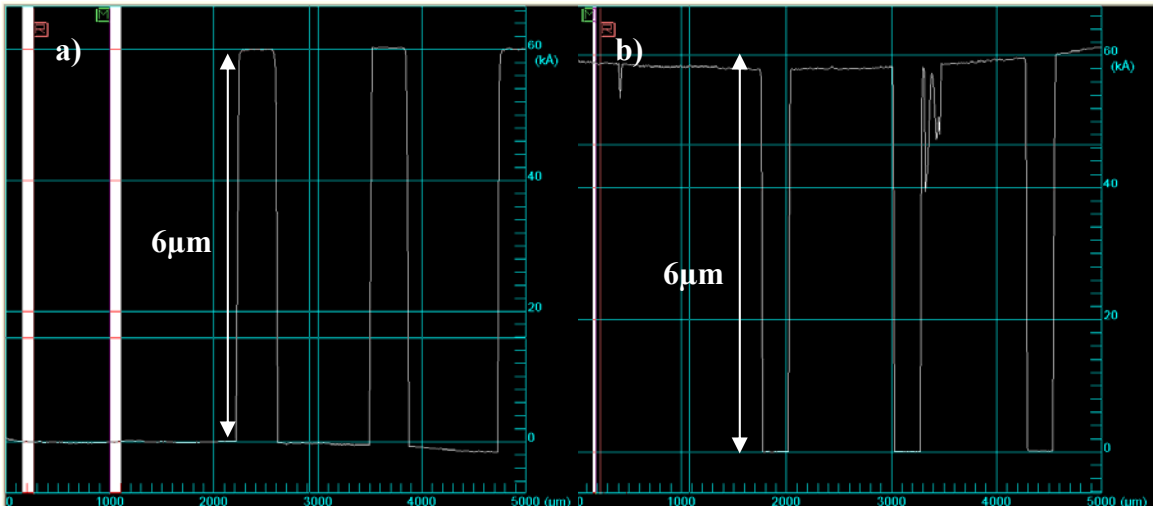

Figure 3.12: Profilometer scans of masters created from optical lithography. a) Profilometer scan of top side master. The height of the relief structures is generally ~6μm tall x Xμm wide for the spin speed and resist used. b) Profilometer scan of bottom side master created from optical lithography. The height of the relief structures are generally ~6μm tall.

Each master was silanized by exposure to a vapor of tridecafluoro-1,1,2,2-tetrahydrooctyl-1 trichlorosilane (United Chemical Technologies) for one hour. Silanization of the wafers prevented the elastomer from sticking and enabled easy peeling after curing. The clean masters were placed in a small dessicator and near a small vial containing a few drops of the fluorinated-silane. The container was then flushed with nitrogen and sealed for one hour to prevent any reactions between ambient and the fluorinated-silane. After silanization, the liquid rubber base, which was vinyl-terminated PDMS (Sylgard 184, DowCorning), and curing agent were mixed vigorously in a beaker, degassed to remove air bubbles, poured over the master, and degassed again until all air bubbles were removed. The master and liquid mixture were then heated to 110°C for one hour in a vacuum oven until the PDMS became a solid, cross-linked elastomer. For the top contact, a negative master was used and for the bottom contact, a positive master was used.

After curing, the polymer substrates used for the top contact were loaded into an e-beam evaporator and metallized with chromium as an adhesion layer and gold (Cr/Au, 10nm/40nm) or aluminum or nickel. To obtain devices with wrinkled metal films, the process was changed slightly. The fabricated PDMS pieces were heated for 30 minutes to one hour above 100°C to thermally expand the material before loading into the e-beam evaporator chamber. Chapter 2.3.8 further detailed the production of ‘wavy’ metal skins

formed on PDMS and the technique to produce oriented nanowires on their surface. After growth, the nanowires were anchored to the waves with a chemically grafted polymer layer as previously described in Chapter 3.3.

To create the soft spacer layer between the devices, a soft contact process[106] using PDMS was utilized. The process flow is depicted in Figure 3.13. Briefly, PDMS monomer and curing agent were mixed in a 10:1 ratio as before. About 1-2 mL of the mixture was placed on a silanized Si wafer and spun at 7000 rpm for 8 minutes using a spin-coater, resulting in a 5μm thick layer of uncured PDMS on the slide. The metallized device to be bonded to the spacer layer was thoroughly cleansed with a swab of IPA and dried with an $N_2$ gun. The device was then placed gently on the uncured PDMS for fifteen minutes and weighted down slightly. The PDMS substrate was then gently lifted off, resulting in the transfer of a layer of uncured PDMS from the glass slide to the contact areas of the device. The device was then degassed and cured at 90º C for 30 minutes.

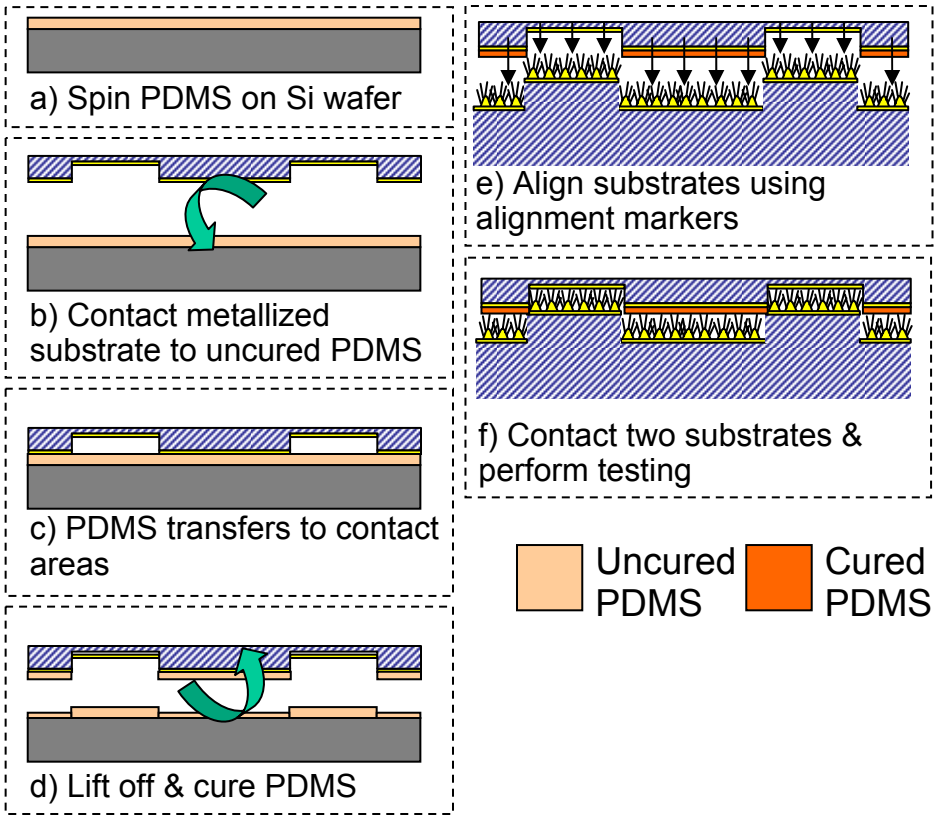


Figure 3.13: Schematic of process flow to create PDMS spacer layer.

Before the assembled devices were tested, a separate test was performed to gauge how well the nanowires were connected and what to expect in terms of the strength of the output. First, one of the rectangular ridges of the bottom substrate near the edge was slowly brought into contact with a flat gold electrode on a glass substrate using a piezoelectric-driven stage monitored by a CCD camera and telescope lens. When the substrate and flat electrode were in contact, the electrode was pressed into the nanowires three microns and immediately retracted. The voltage output of the nanowires was measured using a low-noise voltage pre-amplifier (SR560, Stanford Research Systems) and recorded on an oscilloscope. The current output of the device was measured using a current pre-amplifier (DL1211, DL Instruments). Two tests were performed using this

setup. The first was a single indention to study if any output could be recorded. The second was a repeated deflection to study how the nanowires acted under continuous mechanical input. For this test, the stage would be raised and lowered approximately every few seconds (1Hz was not possible with this type of input because the stage speed could not equilibrate over the small distance so quickly). As can be seen below in Figure 3.14a, the average open circuit voltage output ($V_{oc}$) of the nanowires during a single deflection in forward polarity was approximately 5-10mV. When the electrodes were connected in reverse polarity (negative electrode-positive probe, positive electrode-negative probe) the sign of the voltage flipped and the amplitude remained approximately the same (~7mV). The magnitude of the output voltage was about the same as when an atomic force microscope deformed a single nanowire (~10mV)[42] and twenty times larger than the voltage output from an ultrasonic generator (~0.5mV)[19]. This result is expected since the deflection of the nanowires under the compressive load is relatively large in comparison to that produced from an indirect ultrasonic wave but comparable to that from an AFM. Additionally, the nanowires used for the ultrasonic generator were grown using CVD and generally have less defects, which facilitates less resistivity and less piezoelectric potential. In contrast, the nanowires used here were hydrothermally grown and exhibit more defects and greater resistivities, which have been shown to improve the piezoelectric coefficient for ZnO[70]. The short circuit current ($I_{sc}$) of the nanowires during a single compression in forward polarity and in reverse polarity are displayed in Figure 3.14b. The output ranged from 120pA to 1nA, with the output shown below to be about the average (~650pA). When the electrodes were connected in reverse polarity (negative electrode-positive probe, positive electrode-negative probe) the direction of the current reversed and sign flipped from negative to positive, with the amplitude remaining the same. The double peaks in both the voltage and current signals were present in every

output pulse, regardless of its polarity. The double peak was ascribed to the height difference of the nanowires when they were loaded and unloaded. Since the electrode was wrinkled, the nanowires have different heights relative to the top electrode, and will therefore bend and release their energetic outputs at different times with respect to one another. The nanowires with the largest heights or those closest to the top electrode will release their output at a different time than nanowires at lower heights. Since the currents of each nanowire are in parallel and collectively add, the first peak may be the output of the shortest nanowires as they are bent and released from strain before the tallest wires, which are released from strain last or at a delay. The voltage double peak was less pronounced, which was expected given the weak signal to noise ratio. The background was subtracted from both graphs.

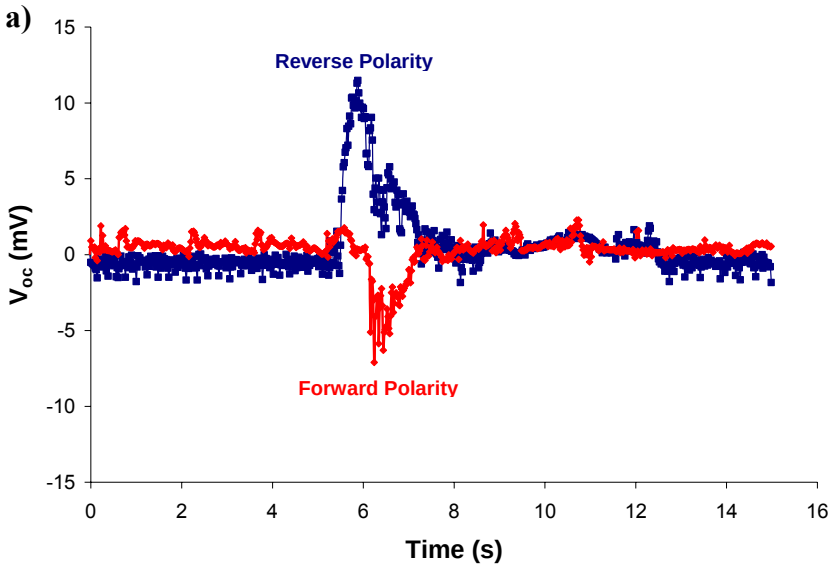

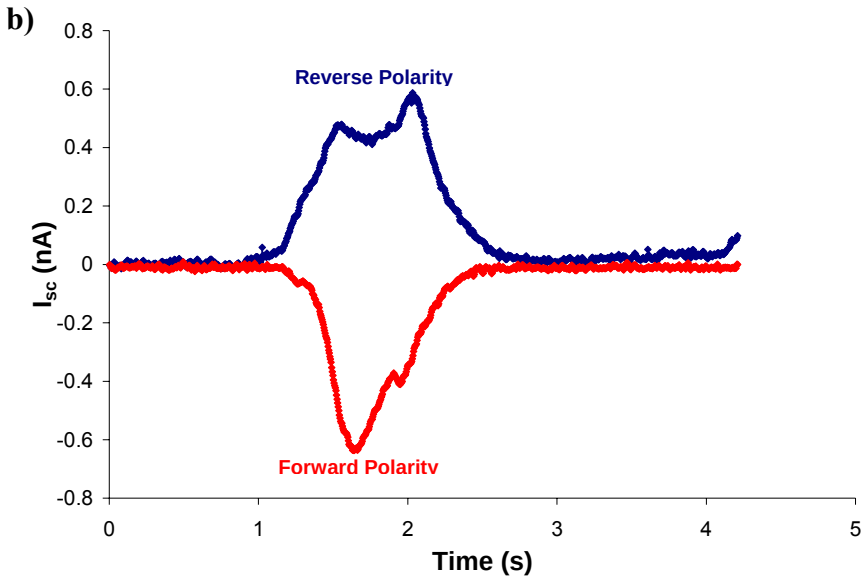


Figure 3.14: Nanowire output during single loading. a) Open circuit voltage ($V_{oc}$) output measured in forward polarity (navy curve) and in reverse polarity (red curve). b) Closed circuit current ($I_{sc}$) output measured in forward polarity (red curve) and in reverse polarity (navy curve). Approximately the same magnitude of the signal was detected for the case when the electrodes were flipped, with only the sign being changed. The background signal was subtracted.

For the case when the nanowires were periodically loaded, the open circuit voltage output in reverse polarity was approximately 6-7mV, and remained stable over the number of applied loadings (Figure 3.15a). The average closed circuit current output in forward polarity was about 180pA for both peaks and in reverse polarity was approximately 200pA for the main peak and 110pA for the tertiary peak (Figure 3.15b). The difference in magnitude of the double peaks for the reverse polarity occurred on a number of substrates measured. The strength of the signal after continuous cycling did not seem to deteriorate, indicating the nanowires remained in tact. Inspection of the surface with SEM showed the nanowires were kept in tact and no visible fractures were

incurred. The measured signals for the cyclic loaded test were less broad than those obtained from a single compression. This result is expected because the response from the plurality of piezoelectric nanowires has a decay time constant that determined by the strain rate. In other words, the faster a nanowire is mechanically deformed and released from strain, the quicker it releases energy and consequently the more energy it can produce per unit time.

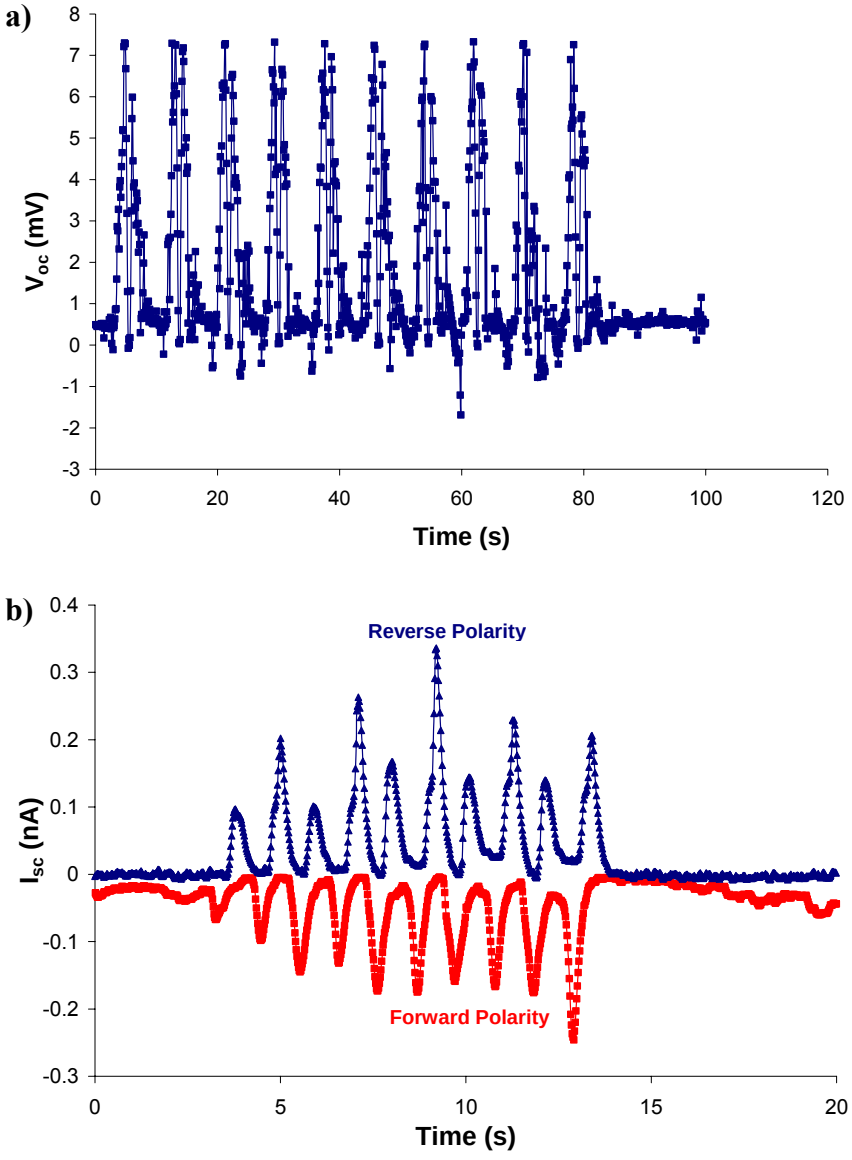

Figure 3.15: Nanowire output during cyclic loading. a) Open circuit voltage ($V_{oc}$) output of sandwich device measured in reverse polarity during periodic loading. b) Closed circuit current ($I_{sc}$) output of sandwich device measured in forward polarity (red curve) and in reverse polarity (navy curve).The observed signal strength was slightly lower in magnitude and less broad than those obtained from a single compression. The background signal was subtracted.

These results prove qualitatively that a strong response can be extracted from the nanowires if they are loaded adequately. The next step was to slowly bring the bottom substrate and top substrate with inverted electrodes and soft spacers in contact using guide pins and the alignment markers. The substrates were then sealed together at their edges. This was accomplished using the exact same setup as the previous tests, using a piezoelectric-driven stage monitored by a CCD camera and telescope lens. Removable pins were used as guides to align the substrates on top of one another. The assembled device was then loaded on the same testbed as the 1st generation device, being fixed at two ends and deflected from the backside. Using this type of loading enabled the waves perpendicular to the experienced compressive and tensile stresses to periodically change their amplitude (A) and wavelength (W), moving the nanowires grown on them up and down. Figure 3.16 illustrates the energy generating mechanism when the substrates are loaded in simulated systole. When the device is deflected and the nanowire surface is compressed (convex case), the heights of the buckles increase and the widths decrease. The small displacement of the buckles drives the nanowire array into the neighboring electrode mechanically deforming them. Analogous to the 1st generation device and ultrasonic generator[19], the nanowire bending creates a potential distrbution within the wire with the stretched side possessing a positive voltage and the compressed side having a negative voltage. When the compressed side of the nanowire with negative voltage at its surface is pushed against the gold electrode, a forward-biased Schottky diode is

constructed. Thus, current flows from the nanowire through the gold electrode, stabilizing the potential, similar as before. When the device is relaxed in diastole, the buckles retract in height and broaden their width, relieving the nanowires from strain. After the relaxation, some recoil of the device or tensile strain is formed (concave case), and the buckles gain wavelength and decrease their amplitude further. The mechanics of the buckled waves have been described elsewhere in more detail[107,108].

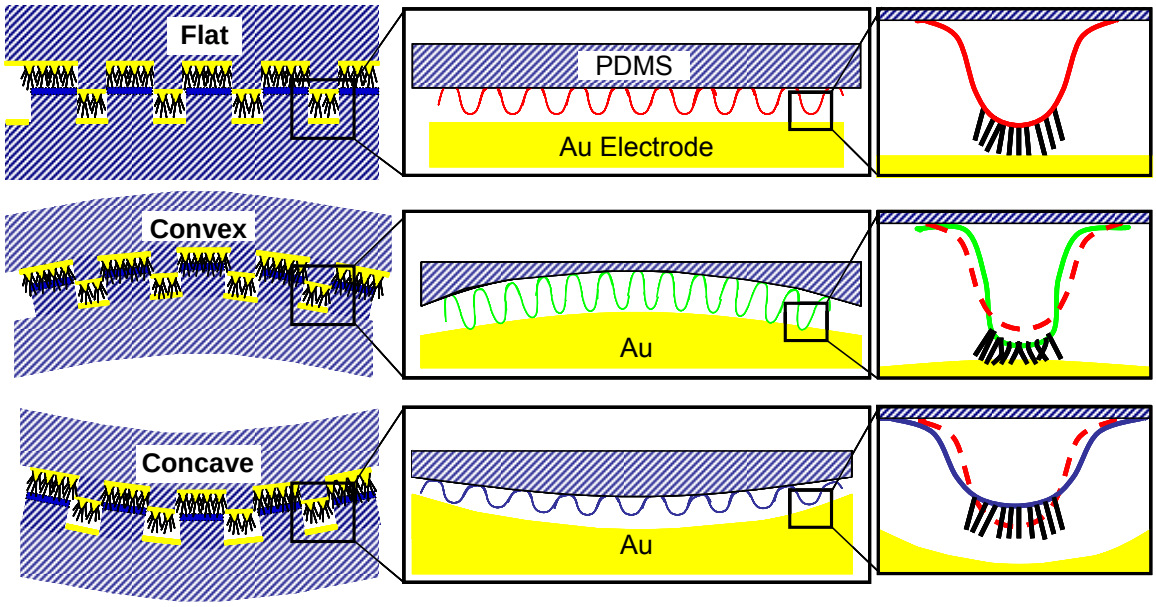


Figure 3.16: Schematic of bending of surface buckled structures on PDMS. The flat surface shows several nanowires touching the gold electrode with very little flexing. As the surface is bent in a convex fashion, the buckles increase their amplitude and press the nanowires into the electrode, bending them as well as capturing the their built up charge. Upon bending the surface in a concave manner, the buckles increase their wavelength and decrease their amplitude, creating a large gap between the nanowires and electrode.

This concept represents an efficient path towards scavenging energy inside AICD leads. Currently, the assembled devices are being tested and optimized. Several key advantages have been demonstrated using this platform. First, the devices should be able

to exhibit longer lifetimes based on the flexible metal electrode. Second, the substrates are amenable to integration with existing AICD leads and do not substantially contribute to the COH, due to their small size and flexible supports. Third, the device architecture permits multiple devices to be stacked on top of one another without loss of performance, enabling the potential for three-dimensional energy generators and higher energy densities. While these advances have pushed this concept, the ideal case of using a flat rigid electrode to compress the substrates illustrated that more power still needs to be withdrawn to fully recharge an AICD battery. To investigate techniques to produce more energy output, a model of the energy generating process was developed.

### 3.5 OPTIMIZATION MODEL

A mechanics model was developed as a means to investigate techniques to produce more output from the energy generator. The model began with the determination of the stress observed inside the lead. An analytical model was constructed that was based off X-ray images of an AICD lead in systole (Figures 3.4a-b), which showed the lead undergoes a bending radius of curvature of 5mm in systole. Assigning a cylindrical coordinate system (r,θ,z) to the lead, the strain ($\varepsilon_{zz}$) resulting from bending during systole (as shown in Fig.3.17) can be determined by the equation:

$$\varepsilon_{zz} = h/\rho = \kappa * h \tag{3.1}$$

where ρ is the curvature under bending and κ is defined as:

$$\kappa = 1/\rho \tag{3.2}$$

If the other strains in the lead are assumed to not contribute as significantly ($\varepsilon_{rr} \approx \varepsilon_{\theta\theta} \approx 0$) and the lead has isotropic properties (Young's modulus, E, Poisson's ratio, υ) the stress from bending at any plane within the lead (P) can be deduced from equation 3.3:

$$\sigma_{zz} = E\,[\varepsilon_{zz} - \upsilon(\varepsilon_{rr} + \varepsilon_{\theta\theta})] = E*\varepsilon_{zz} = E\kappa r \sin[(\theta + \theta_o) - \pi/2] \tag{3.3}$$

From equation 3.3, it can be concluded that the maximum tensile and compressive stresses occur at the top and bottom point of the cross-section. Using the radius of the lead, R, the max stress can be written as equation 3.4:

$$\sigma_{zz} = E\kappa R \tag{3.4}$$

The observable max stress was then calculated for an AICD lead with ρ=5mm and R=3mm as 300kPa.

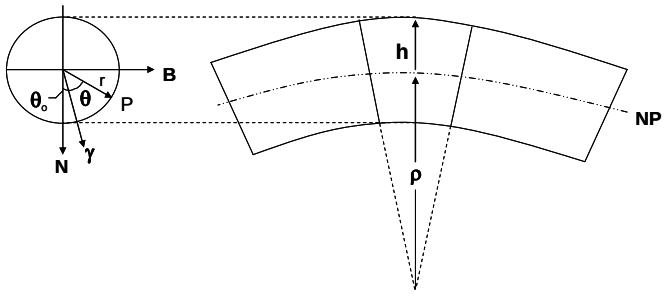


Figure 3.17: Illustration of coordinate system to define AICD lead parameters.

The surface stress can be translated into a load by multiplying the surface area of the lead. Assuming the imparted load is fully absorbed and divided in proportion to the stiffness of the materials within the lead[102], the approximate load inputted onto the nanowires can be obtained. Since the conductor material is a cobalt-based super alloy (MP35N® or 35N LT®, E~207GPa) and the insulating polymer is comparatively much less stiff (E~500MPa), the insulating outer regions of the lead will roughly absorb 0.2% of the bending load. Conservatively assuming a fraction of the load (~5% for a 60μm thick device) experienced in the insulating region is transferred into a nanowire array located approximately 100μm below the surface; the average load acting on an individual nanowire would be approximately 360nN. The transmitted force can be increased or decreased by changing the location of the nanowires within the insulating rubber region. For example, a generator located nearest to the surface experiences a much higher force

than one located near the center of the tube. The determined force was then translated as an input to a mechanics model to analyze the strain experienced a single nanowire for a range of nanowire aspect ratios.

First, using conventional static loaded beam bending, the minimum force needed to bend a single nanowire with different aspect ratios was determined. This calculation was needed to verify the systolic mechanical input would be able to induce bending and in turn a current output through the piezoelectric effect. The buckling of the nanowires occurs when the reduced force ($\psi$) is greater than the angle $\pi^2/2$. $\psi$ is calculated as:

$$\psi = 2fh^2 / EI \tag{3.5}$$

where f is the force experienced by the nanowire, h is the height, E is the Young's Modulus (given as 111GPa[109]), and I is the moment of inertia of the cross section of the nanowire which for a hexagon is given as:

$$I = \frac{5\sqrt{3}}{16}\left(\frac{d}{2}\right)^4 \tag{3.6}$$

where d is the maximal diameter. Using the relationship for $\psi$, the minimum force needed to bend a nanowire was determined. As can be seen in Figure 3.18, the minimum force decreases as a function of aspect ratio, h/d. As the aspect ratio increases, the force needed to bend the nanowire asymptotically decreases. The approximate load determined previously from RV contraction within an AICD lead is marked on the plot by a blue dashed line.

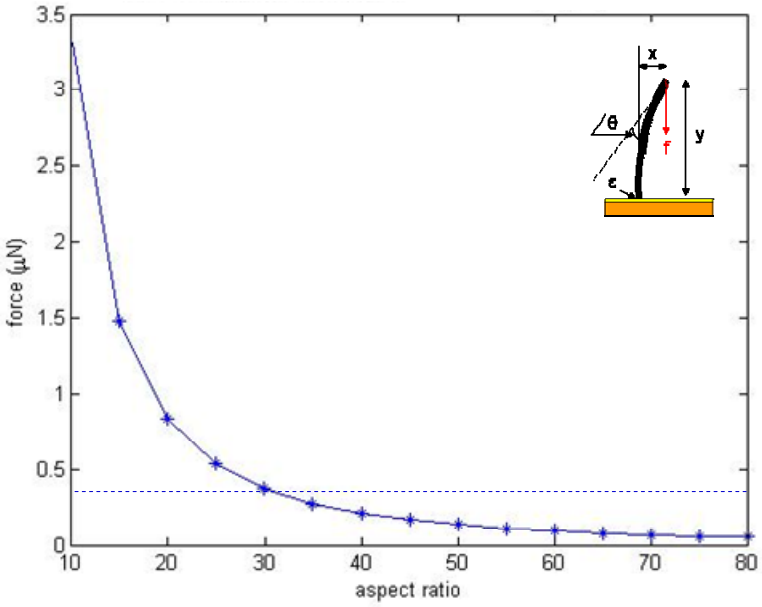


Figure 3.18: Minimum force to bend nanowires with varying aspect ratios.

The maximum strain experienced by the nanowire, which occurs at the base, can then be calculated as:

$$\varepsilon = \frac{1}{4}\frac{d}{h}\frac{x}{h}\Psi \tag{3.7}$$

where x is the horizontal projection (inset to Fig. 3.18). Figure 3.19 shows the strain plotted as a function of angle of deflection for various aspect ratios. The green line on Figure 3.19 represents the fracture strain of ZnO nanowires given as ~5%. Since the equation for strain is inversely proportional to aspect ratio, higher aspect ratios undergo less strain. However, it takes less force to bend a nanowire with a higher aspect ratio, or for a fixed force, a higher aspect ratio nanowire will bend more than a lower aspect ratio nanowire. This result is expected as a nanowire that is shorter and thicker will be harder to bend than a nanowire that is longer and thinner. From Figure 3.19, it can also be deduced that higher aspect ratio nanowires, or those greater than or equal to 40, can be bent to 90° off the vertical without fracturing.

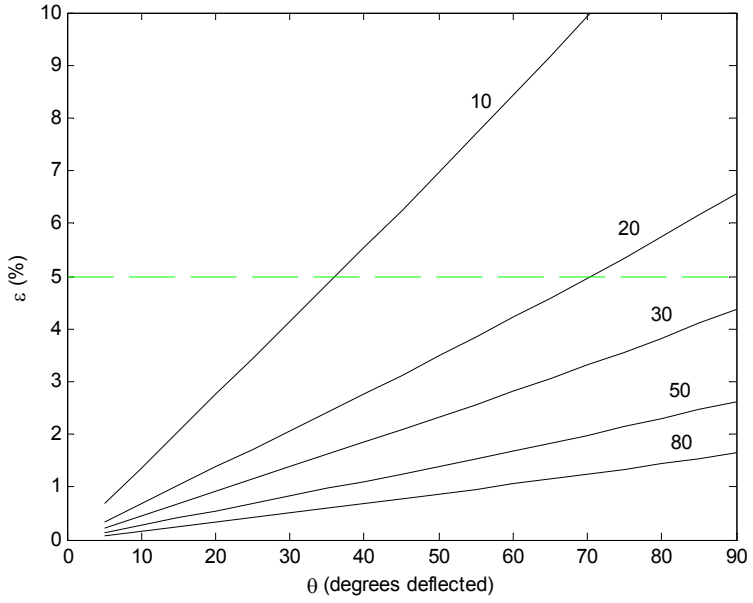


Figure 3.19: Strain as a function of deflection angle for various aspect ratios. Dashed line represents fracture strain for ZnO nanostructures.

The current output from a piezoelectric ZnO nanowire can then be described according to the relationship:

$$i = d\frac{\partial F}{\partial t} = dAE\frac{\partial \varepsilon}{\partial t} \tag{3.8}$$

where d is the piezoelectric charge constant (~7.34pC/m)[70], A is the cross sectional area given as:

$$A = \frac{3\sqrt{3}}{2}\left(\frac{d}{2}\right)^2 \tag{3.9}$$

and $\frac{\partial \varepsilon}{\partial t}$ is the applied strain rate (i.e. strain multiplied by the frequency, 1.1Hz for a heartbeat). Figure 3.20 demonstrates the linear increase in the current output *(i)* as a function of the nanowire bending (θ). This graph depicts the more the nanowire bends, essentially the more current it can output.

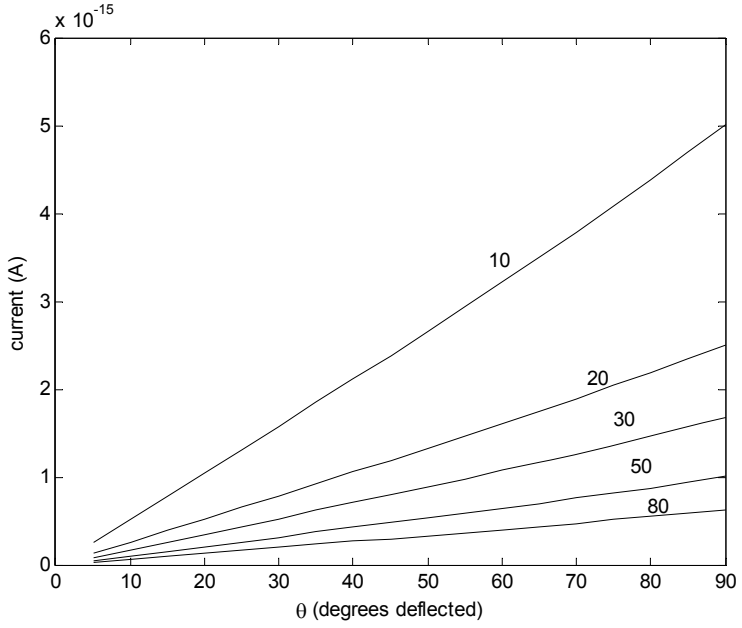


Figure 3.20. Current output versus degrees deflected for nanowires with various aspect ratios.

The previous plots demonstrate how strain and output current are dependent on the degree of the deflection of the nanowires and aspect ratio. However it should be noted that these two results assume different input forces for each aspect ratio, which is a misnomer because the systolic input is fixed. These two plots rather illustrate that the shorter stiffer nanowires can supply more current only if they are supplied with more force. Since the systolic load on the nanowires would be approximately fixed, to tune the deflection and in turn output current, the nanowire aspect ratio was manipulated. Figure 3.21 exhibits the effect of the nanowire aspect ratio has on the output current if they were subjected to the same input load, in this case ~2μN. Clearly, higher aspect ratio nanowires are more susceptible to bending than smaller aspect ratio nanowires; thus, higher aspect ratio wires undergo more strain and produce larger currents.

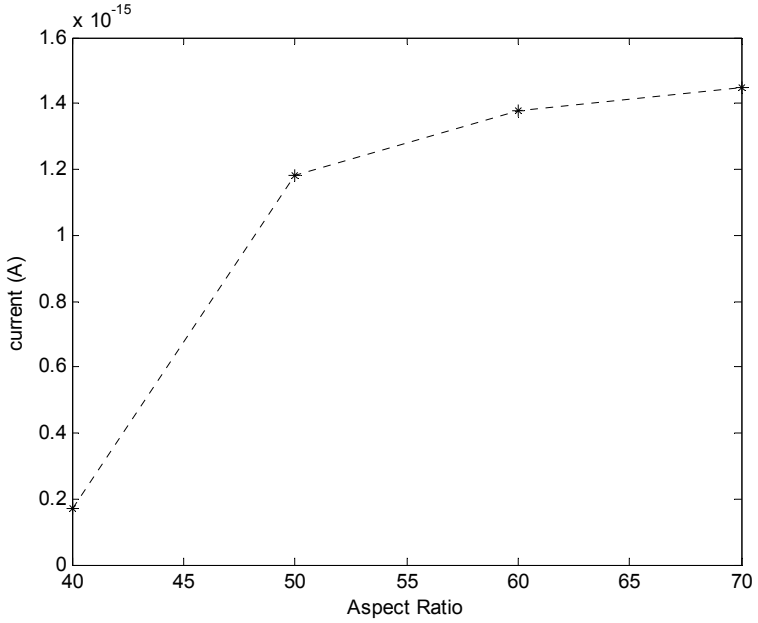


Figure 3.21. Current production as a function of aspect ratio. Each nanowire wire was subjected to the same force, only the aspect ratio was varied.

The Young's Modulus (E) of the nanowires also plays a role in determining the current output. While conventional crystalline materials exert similar mechanical properties, nanostructured materials, such as nanowires, in practice demonstrate broad distributions[110]. The influence of the Young's modulus on the current output for a nanowire with an aspect ratio of 50 and an applied force of ~2μN is plotted below in Figure 3.22. The range of moduli plotted has been quantitatively measured for nanowires with 50-300nm diameters. This plot demonstrates that the harder a nanowire is; the less current can be drawn from it using the fixed load from systole.

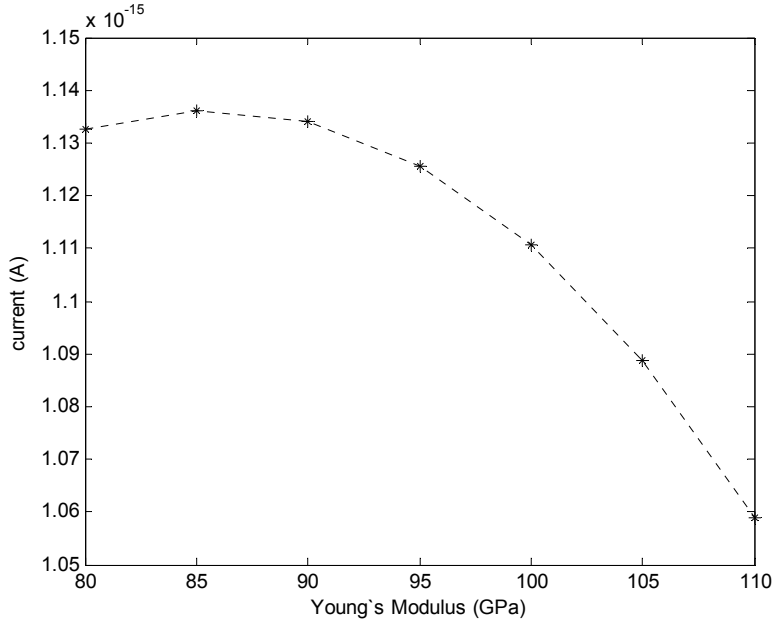


Figure 3.22. Role of Young's Modulus in output current.

The influence of the piezoelectric charge coefficient (d) on the output current can also be investigated. Given that d is linearly proportional to the output current, a reduction of d by 2 would lead to half the current or an increase of d by 2 would result in twice the current. Using these results, we can estimate the energy production of a plurality of nanowires for different aspect ratios. Using the results of the approximate force applied on the nanowire and the two relationships given for the reduced force, the deflection of the nanowire was determined as $\theta$=17 degrees. For the calculated deflection, a single nanowire with aspect ratio of 50 would experience a strain of ~0.47%, leading to a current output of 0.178fA. This output is nearly equal to the output seen from a single nanowire deflected by an AFM[42] (~0.05fA) which was bent further than 17 degrees. For the device constructed in Chapter 3.4, which we assume to utilize at least 10 million nanowires, the model predicts an output of 1.8nA, which is roughly 3 times

higher than the average measured values. The discrepancy can be ascribed to several points. The first is the resistance that forms between the nanowire and gold electrode. The interfacial resistance is very large since the contact area is small and probably consumes most of the potential bias to drive the Schottky diode. Second, the number of nanowires actually participating in the process may be smaller than what was estimated. Though each nanowire was assumed to generate an output, the variation in height of the array and distribution of wave sizes may prevent a substantial number of nanowires from actively engaging the contact and producing energy. Third, the variation of nanowire properties, specifically resistivity, may enact some nanowires to produce less output than others, which would suppress the expected signal.

Several conclusions can be drawn from the model output. First, effective control over the output current can be achieved through changes to the synthetic conditions, specifically by manipulating the nanowire aspect ratio. For example, using nanowires with an average aspect ratio of 50 enables 5 times more current production than nanowires with an average aspect ratio of 40. Second, by changing the location of the nanowires within the lead, different output currents can be also realized. For example by moving the nanowires closer to the surface of the lead, higher forces and nanowire strains can be encountered, which would lead to higher output currents. However, at higher strains, nanowires with high aspect ratios would uproot or plastically deform because of the enhanced bending. Therefore, lower aspect ratio nanowires would have to be used at locations near the surface. This striking observation brings up the notion that for a 3-dimensional array of nanowires to be most effective, its geometrical properties would need to be staggered with the smallest aspect ratio nanowires near the surface and the largest aspect ratio nanowires near the center. If one layer of nanowires with a density of

$10^{10}/cm^2$ was located 100μm below the surface and assuming every nanowire could contribute the same output, the model predicts for the available surface area within the AICD lead (10 $cm^2$), roughly 17.8μA could be withdrawn from a single heartbeat. If 3 or 4 layers of nanowires could be embedded and each could be accessed to produce an energy output along with one layer of PVDF, an AICD could run on the generator output without the use of a battery.

## 3.6 CONCLUSIONS

The goal of this project was to investigate means with which harvesting the energy of the heart could be accomplished imperceptibly. Since ceramic piezoelectrics with large piezoelectric coefficients could not be used, a device comprised of PVDF was first employed. The polymeric piezoelectric generator was tested on a system that mimicked a failing RV and displayed a strong voltage output but rather low current. As a means to raise the current production a "sandwich" device was constructed on interlocking silicone rubber pieces. One side of the device was patterned with wrinkled electrodes that change shape when the device is flexed. The shape change drives the nanowires grown on the electrodes up and down into the other side of the sandwich that was coated in metal. When a nanowire moves up into the neighboring electrode and bends, a potential distribution is built due to the direct piezoelectric effect. When the compressed side of the nanowire with negative voltage at its surface is pushed against the gold electrode, a forward-biased Schottky diode is constructed. An output current is then driven into the gold electrode, stabilizing the potential. When the device is relaxed, the buckles retract in amplitude and broaden their wavelength, relieving the nanowires from strain. Compression tests of one of the ridges on the bottom substrate outputted on average ~6.5pW. Considering the size of the generator, an active power per unit area of

~0.5nW/cm$^2$ was achieved. In contrast to the fiber nanogenerator, which at this time is the only other publication of a nanowire-based energy harvester operating at low frequencies, the output shown here is 182 times higher. This is expected as the mode of deformation of two brushes rubbing against each other is much smaller than the planar compression experienced in this work. The device architecture permits scalable integration with existing AICD leads and also does not heavily contribute to the COH. The device should also demonstrate a longer lifetime than existing nanogenerators because of the wavy metal electrode. Since the devices were fabricated on rubber, several devices should be able to be stacked on top of one another within the lead for higher energy densities. While this progress has facilitated power outputs from devices that can be incorporated within AICD leads at little to no cost in the COH, more power needs to be withdrawn to fully recharge an AICD battery. To increase the output from the nanostructured generator, a mechanics model was developed to investigate the influence of geometrical properties on the piezoelectric response. From the model output, insight was gained as to how to structure the nanowire array within the latitude of the synthesis outlined previously to maximize the power output.

Future research on the device can be divided into a three areas: 1) lifetime and fatigue behavior of the device, 2) more comprehensive analysis of the mechanics of the device, and 3) methods to augment the power density of the device without compromising the COH. The first focus of research studying the lifetime of the developed devices should include periodic SEM studies of the nanowire surface to identify possible mechanisms of failure such as wire fracture from the electrodes and degradation of the electrode buckling. Currently there is no literature available on fatigue behavior of nanowires and only one study on carbon nanotubes, which when

compression-tested as an ensemble, exhibited viscoelastic behavior[111]. If this effect is also present for the nanowires, the device may exhibit lifetimes exceeding those of conventional bulk piezoelectric energy generators. Actuators based on bulk polycrystalline piezoelectrics such as PZT have lasted upwards of $10^9$ cycles with less than a 1% loss of performance. If the device was able to continuously produce output for the same number of cycles loaded at 1.1Hz, it would last approximately 30 years. The degree of polarization during and post-testing should also be locally investigated on the nanowires with AFM. Wear tests on the buckled electrodes and polymer substrates may also elucidate possible points of failure and ultimately lead to mechanically tougher or longer lasting design concepts. The second focus should be geared towards developing a more comprehensive understanding of mechanics of the device and the modes of deformation during systole. Solving the analytical solutions to the complex nonlinear electro-mechanical systems during systole may yield guidelines to further tune the synthesis for enhanced device performance. Additionally, finite element analysis (FEA) of the interface between the polymer substrate and the buckled metal films may provide new insights into other potential failure modes that may impede performance. The third aim to raise the power density of the device without compromising the COH can include an umbrella of approaches. First, one avenue to pursue would be to exchange the spacer layer or substrate from PDMS to PVDF. Replacing the PDMS with PVDF would enable every part of the device a functionality that could produce energy, rather than just the nanowires on the raised ridges. Or changing the device design to include the nanowires that are currently impacting the spacer layer would also raise the power density. Yet another variant would be to embed the nanowires in PVDF and use a composite material as shown in Figure 1.6 as the interlocking pieces. In addition to exhibiting increased efficiency and possibly condensing the charging time, hybrid biphasic structures also

possess better mechanical toughness than the individual phases that comprise them, which would permit a longer lifetime. Second, using nanowires with larger piezoelectric coefficients such as $BaTiO_3$ or $KNbO_3$ may also increase the energy density. However synthetic techniques to grow 1-D perovskite materials have not been able to produce an ordered array, much less at low temperature on plastic. Nonetheless, new device designs and assembly techniques to integrate such nanowires may ultimately deliver enhanced performance. Third, controlling the interface between the nanowires and neighboring contacts by modulating the barrier height can also permit higher piezoelectric responses. Chapter 4 details this avenue of research further.

# Chapter 4: Molecular Engineered ZnO Nanowires

Improving the piezoelectric performance of ZnO nanowires relies on several factors as previously outlined in Chapters 1 and 3. One method to augment the output is to tune the size of the barrier between the nanowires and metal electrode to control the flow of charge carriers. Typically, in an ideal rectifying metal/n-type semiconductor junction, the Schottky barrier height ($\Phi_b$) is defined as the energy difference between the metal work function ($\Phi_m$) and the semiconductor electron affinity ($\chi_s$), as $\Phi_b=\Phi_m-\chi_s$[112,113]. Controlling $\Phi_b$ can be accomplished with a variety of techniques such as metal selection and thermal treatment. While metal selection would be the most direct approach, the number of metal choices are limited and it has been shown that the semiconductor surface (specifically the presence and activity of surface states) rather than the metal work function dominates the behavior of the Schottky diode[114,115]. Accordingly, a technique was sought to control the size of the barrier by modulating the semiconductor surface. One solution is to decorate the semiconductor surface with a layer of molecules, and use the molecular functionality to electrostatically influence the semiconductor interfacial properties. Adsorption of polar organic molecules on semiconductor surfaces has been shown to induce significant changes in the electrostatic potential and in turn, electron affinity ($\chi$) and work function ($\Phi$). However, quantitatively measuring the impact of systematic molecular surface treatments on the electron affinity or work function of a single nanowire has not been accomplished.

In this chapter a low photon energy photoelectron spectroscopy tool is developed to measure the interfacial electronic properties that directly influence $\Phi_b$ and the energy generator output. First, native ZnO nanowires were characterized and the nanowire

surface was then perturbed to highlight the influence of several adsorbate molecules on the measured properties and the adsorption and desorption events were correlated to electronic property changes. As a significant next step, for the first time, quantitative optical measurements of interactions between various dipolar phosphonic acid-based SAMs and the nanowire work function were assessed. Self-assembled monolayers (SAMs) of various phosphonic acid (PA) based molecules were chosen as a platform to study changes in Φ because PAs are strong binders to metal oxides and have been shown to have a pronounced effect on Schottky barriers applied to thin films of ZnO [114]. The molecular effect was modulated using SAMs with different dipole strength and almost fully reversed by environmental substitution or heat.

## 4.1 LOW PHOTON ENERGY PHOTOELECTRON SPECTROSCOPY

Electrical test structures such as field-effect transistors (FETs) are normally used to characterize the physical properties of nanoscale materials. However, the ability to reproducibly form high-quality contacts to ZnO nanowires has remained a significant impediment towards electrical assessment of their intrinsic properties[116]. A general optical diagnostic technique that can noninvasively measure such electronic properties on individual nanowires and nanotubes is needed. Among existing optical diagnostic techniques studying individual nanostructures, Rayleigh scattering[117,118] and Raman spectroscopy[119] have been performed on carbon nanotubes but other metrology techniques have been scarce. Conventional scanned probe techniques such as scanning Kelvin probe microscopy are primarily applicable to planar thin films and versions of scanning tunneling microscopy can provide information on local electronic structure but are limited by the size of the probe tip[120]. All of these technologies and issues point to

the need for significant improvements in metrology measurements for 1-D nanostructures.

Low photon energy photoelectron spectroscopy is a salient tool suited to study the electronic properties of individual 1-D nanostructures[121]. Photoelectron Spectroscopy (PES) refers to the measurement of energetic electrons emitted by the photoelectric effect, in order to determine the binding energies of the electrons. In low photon energy PES, the photon energy is much lower than conventional PES, which usually is carried out in the 20–100eV energy range, where the typical mean free paths range from 3-5Å and are at the universal minimum of photoelectron mean free path in solids[122,123]. Rather low photon energy has a much deeper penetration depth (~10nm) from the surface (Fig. 4.1a), enabling the ability to probe bulk states. Another feature of the low kinetic energy is the technique is highly surface sensitive and can be coupled to synthetic studies of different environments and various adsorbed surface species to elucidate their respected influences on surface-sensitive properties such as the work function. Given that the work function of a material is directly affected by any surface dipole or molecular charge[124], via changes in the electron affinity, the work function and the electronic performance of individual ZnO nanowires can be engineered using molecular functional groups and studied using low energy PES.

In PES, the process begins with a sample in vacuum that is irradiated with monochromatic light. A three-step model can be used to describe the next 3 phases. In the first step, photoionization takes place, where according to Einstein's photoelectric effect, upon absorption of a photon, an electron is excited. In the second step, the electron travels through the sample to the surface. In the third step, if the photon is

sufficiently energetic to promote an electron to a state above the vacuum level of the sample, a photoelectron is emitted where it can then be detected. The emitted electrons, each with discrete kinetic energies, are collected and analyzed with an electrostatic analyzer that builds a distribution (spectrum) that reflects the electronic structure of the sample[125]. Figures 4.1b-c display schematics of the proposed PES experiment on ZnO. Figure 4.1b shows the energy-level diagram of a ZnO sample and the kinetic energy distribution measured at the detector. Figure 4.1c shows how the photoemitted electrons measured at the detector relate to binding energies within the sample. The binding energy of an energy level measured here is generally referred to with respect to the Fermi level, where a positive binding energy refers to an energy level below the Fermi level.

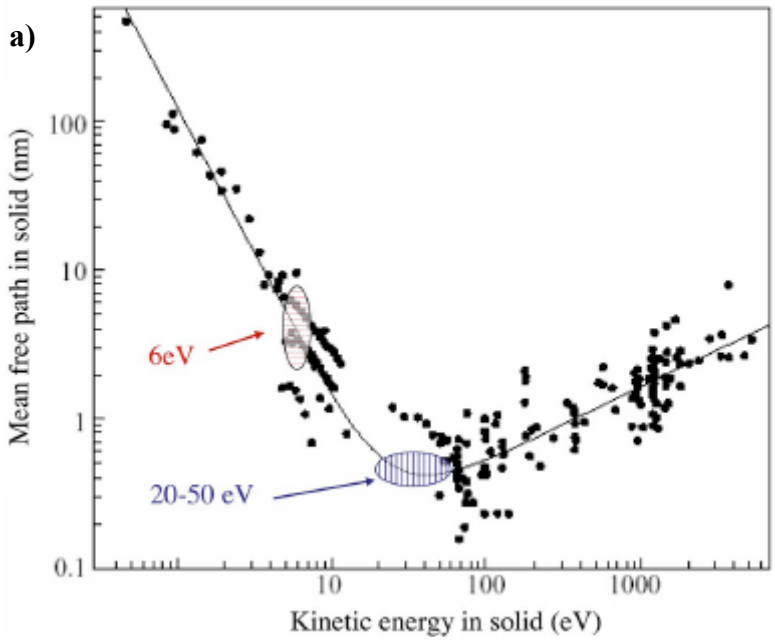

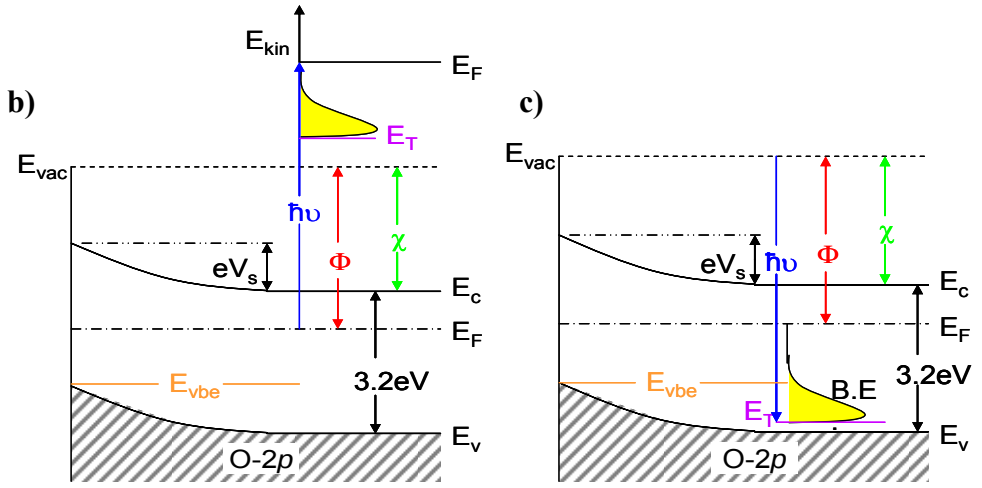


Figure 4.1: Theoretical framework for PES experiment. a) The "universal curve" for electron inelastic mean free paths from a variety of materials are plotted vs the kinetic energy relative to the Fermi level (reprinted from Koralek et al [122]). The mean free path for the experiment (6eV) is highlighted on the graph. b)-c) Relation between electron energy distribution and energy levels in solid. Photons of energy (ħυ) are absorbed and eject photoelectrons above the vacuum level ($E_{vac}$), where they hit the detector with a discrete kinetic energy ($E_{kin}$). The spectrum of kinetic energies is related to binding energies (B.E.) that correspond to discrete energy levels in the semiconductor. The binding energy of an energy level measured here is generally referred to with respect to the Fermi level. b) Represents a spectrum at the detector and c) represents the spectrum within the material.

## 4.2 EXPERIMENTAL DESIGN AND SETUP

To probe individual nanostructures using PES, an experimental setup needed to be constructed that would be able to focus deep ultraviolet (DUV) laser light onto an isolated nanostructure. The low photon energy PES system was constructed on a vibration isolated / free floating optical table. 150 femtosecond (fs) pulses of 200nm (6.2eV) light were generated at a 250kHz repetition rate from a regeneratively amplified Ti:sapphire laser operating at a fundamental wavelength of 800nm. The 800nm light was frequency quadrupled in three different beta-borium borate (BBO) crystals to 200nm

(6.2eV) and the collimated beam was then passed into an ultra-high vacuum (UHV) chamber where it was focused down through a Swarzchild reflective objective (NA=0.5) onto a sample at normal incidence (Figure 4.2).

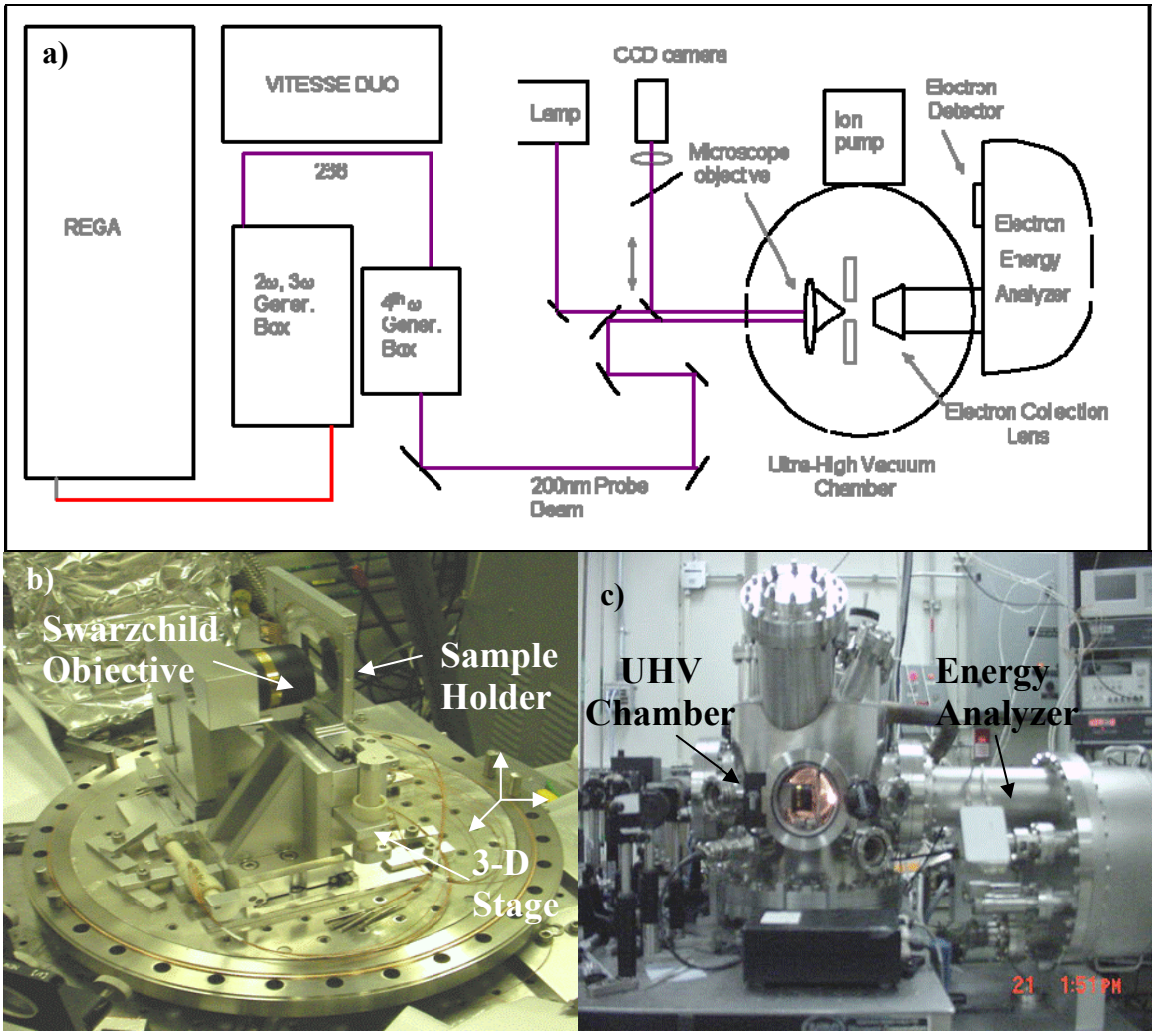


Figure 4.2: Experimental setup to perform photoelectron spectroscopy on individual nanowires. a) Outline of laser and UHV system on optical table. b) Photograph of 3-dimensional stage, sample holder and Swarzchild objective lens. c) Photograph of UHV chamber and hemispherical electrostatic energy analyzer.

In order for individual, isolated nanowires to be irradiated and photoelectrons collected from them, the nanowire had to be suspended so the electron collecting lens could be positioned behind it. To create such a support for the nanowires, Si wafers were lithographically patterned with micrometer spaced through holes/slots, over which the nanowires were suspended. Slotted Si wafers were created by photolithography and anisotropic etching to yield completely etched-through slots (~20-30μm wide x 1mm length). Reflective metal alphanumeric characters (Cr, 50nm) were dressed onto the wafer using photolithography near the edges of the created slots to help identify the nanowire locations in the ultra-high vacuum (UHV) chamber (Figure 4.3a-b). ZnO nanowires were grown using the method outlined in Chapter 2 and sonicated off from their growth substrate into a solution of VLSI grade ethanol. The solution was then flow directed[67] perpendicular to the long axis of the slots in an effort to align the nanowires. However, very few nanowires would extend into the gap based on fluidic alignment. Individual nanowires of interest were picked up and aligned by nanomanipulation (Zyvex S100) (Figure 4.3c). Using the nanomanipulator, nanowires were picked up and placed so that about 4-5 nanowires, typically well separated from one another (at least 50μm), were placed over the width of the slit. This procedure was performed several times to yield a high number of nanowires on the same sample wafer to give a broad distribution of nanowire sizes. Once the nanowires were assembled and aligned to hang over the slot, a small layer of platinum was e-beam evaporated at the base of the nanowire using FIB to hold it in place. Samples were tested before and after the soft metal deposition, and no difference in the spectrum was recorded. Immediately after metal deposition, the nanowires and Si substrate on which they rested substrate were washed with deionized water and ethanol three times, dried with an $N_2$ gun, and cleaned with $O_2$ plasma (50sccm $O_2$, 100W, 60secs) to remove any residual organics. The substrates were then loaded into

the UHV chamber and the system was pumped down overnight until adequate vacuum pressure was reached to perform analysis. When the sample had reached vacuum pressure ($2x10^{-7}$ torr), a three-dimensional piezoelectric stage drove the Si substrate to the location of the welded nanowires. A lamp (248nm) was used to illuminate the substrate when it was loaded into the chamber and a charge-coupled device (CCD) camera was used to identify the locations of the assembled nanowires. Once the sample was placed into position, the laser was focused onto the individual nanowire (Figure 4.3d-e), which could be monitored by the nanowire fluorescence using the developed imaging system. Upon laser irradiation, photoemitted electrons were produced and collected from the opposite side of the nanowire and analyzed by a hemispherical electrostatic analyzer with 20meV resolution.

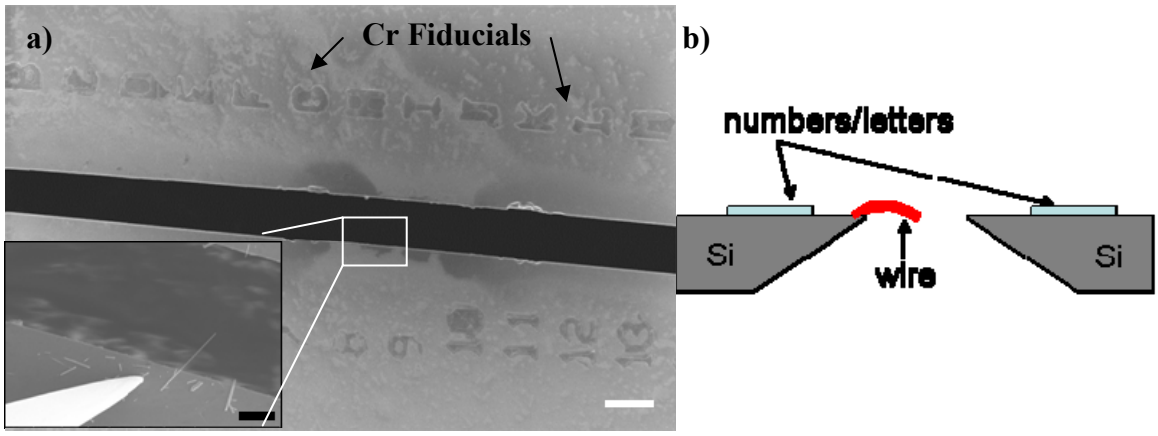

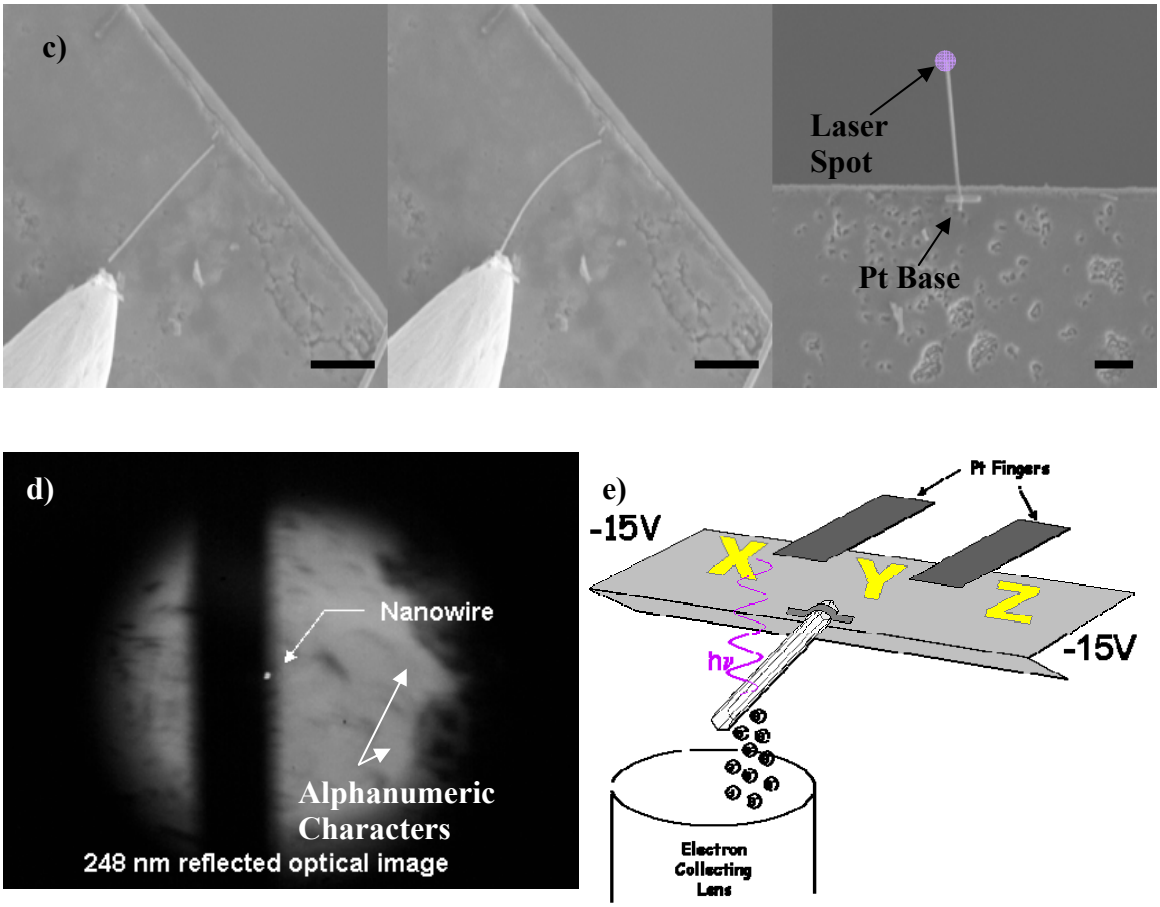


Figure 4.3: Nanomanipulation assembly and integration. a) SEM image of lithographically patterned Si wafer with alphanumeric characters (Cr) and anisotropically etched from the opposite side with (20-30μm width x 2mm length) through slots. Scale bar is 20μm. Inset is SEM image of typical nanowire extending into a patterned slot. Scale bar is 5μm. b) Schematic of laser extending over edge of anisotropically etched Si wafer with alphanumeric characters patterned on both sides to act as guides. c) Consecutive SEM images of nanomanipulation assembly of individual ZnO nanowires from initial movement to final position after securing with Pt at the base. The approximate size of the focal spot is indicated on the last SEM image. The scale bar is 2μm in each SEM image. d) Reflected optical image taken from CCD camera of slotted substrate in UHV chamber. The laser is irradiating a single nanowire extending over the edge, which can be seen fluorescing (bright white spot near edge). The patterned characters in the edge of the image act as guides for the nanowire location. e) Schematic of laser light knocking photoelectrons off of nanowire into collecting lens situated underneath.

To minimize background scattering and to produce spectra free from the local perturbations of the underlying substrate, several spectra were recorded at different positions along the nanowire and averaged (Fig. 4.4). This capability offers sufficient versatility and speed to probe spatially localized doping regions along an individual 1-D nanostructure, which could have implications for studying on-wire p-n junctions as well as axial doping profiling for 1-D nanostructures. Each spectrum taken was performed five times and averaged.

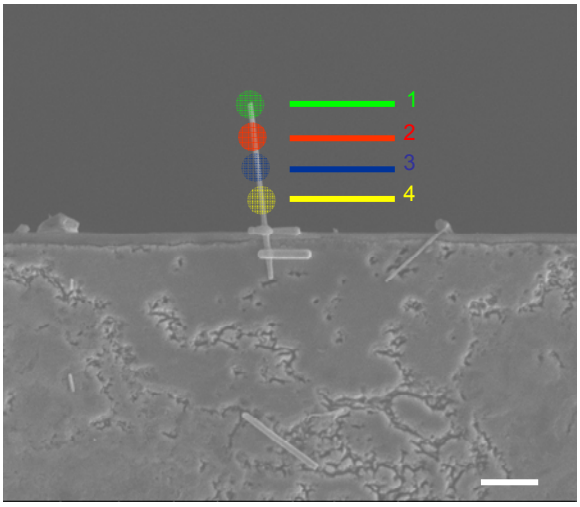


Figure 4.4: SEM image of nanowire extending into lithographically patterned gap. Colored circles indicate approximate laser spot size and position where spectra were recorded on nanowire. Scale bar is 2µm.

### 4.3 ELECTRONIC PROPERTIES OF INDIVIDUAL ZnO NANOWIRES

A Pt film was placed in contact with the sample to identify the location of the Fermi level ($E_F$) of both the nanowires and the Pt film. All spectra were collected with the sample negatively biased (U=-15V) to permit observation of the entire nanowire spectrum and the photoemission threshold ($E_T$), which was necessary for work function

determination. The spectrum read from the detector is a kinetic energy distribution of the emitted electrons (Fig.4.5a), which give a replica of the electron-energy distribution in the solid. When the electrons reach the detector, the kinetic energy ($E_{kin}$) with which they are measured has an extra 15eV, which is subtracted according to equation 5.1:

$$E_{kin} = \hbar\upsilon - (E_{gap} + \chi) + eU \quad (5.1)$$

where $\hbar\upsilon$ is the photon energy, $E_{gap}$ is the bandgap energy, and $\chi$ is the electron affinity (Fig. 4.1b-c). To transform the kinetic energies into binding energies, first, the location of the Fermi level ($E_F$) of the Pt film and the nanowire sample were determined. The Fermi level was determined by studying where there was a sharp drop-off in the intensity spectrum at the highest kinetic energy. The Fermi level was nominally assigned as the half height point (inset to Fig. 4.5a). The Fermi level of the Pt and nanowire sample was located at a kinetic energy of 16.98eV. In all PES measurements, $E_F$ is taken as the natural zero. Next, the kinetic energies were transformed into binding energies (B.E.). The binding energy of an energy level measured here is generally referred to with respect to $E_F$, where a positive binding energy refers to an energy level below $E_F$. $E_F$ was subtracted from the kinetic energies to give the binding energies (B.E.), via equation 5.2:

$$B.E. = E_{kin} - E_F \quad (5.2)$$

A typical spectrum of an individual native ZnO nanowire is portrayed in Figure 4.5b in terms of its binding energies[126]. The position of the Fermi level at 0eV binding energy is noted, and the photoelectron emission threshold ($E_T$) was identified at 1.51eV. $E_T$ varied within 400meV for spectra taken on thirty different nanowires (Fig. 4.5b). Identifying where the binding energy ($E_B$) turns on from the recorded spectra, $E_T$, and the photon energy, the work function ($\Phi$) can be obtained via equation 5.3:

$$\Phi = \hbar\upsilon - E_T \quad (5.2)$$

For the nanowire in Figure 4.5b, the work function is 4.69eV. The average Φ for a distribution of nanowires was 4.67eV (Figure 4.5c), 540meV lower than its bulk value for the {1010} face. With several exceptions, most of the work functions populated a range of 4.58-4.73eV and did not show a dependence on nanowire diameter. The hexagonal faceting of the nanowire, orientation of the facet/edge relative to the detector and cleanliness of the surface all may be responsible for the Φ variation.

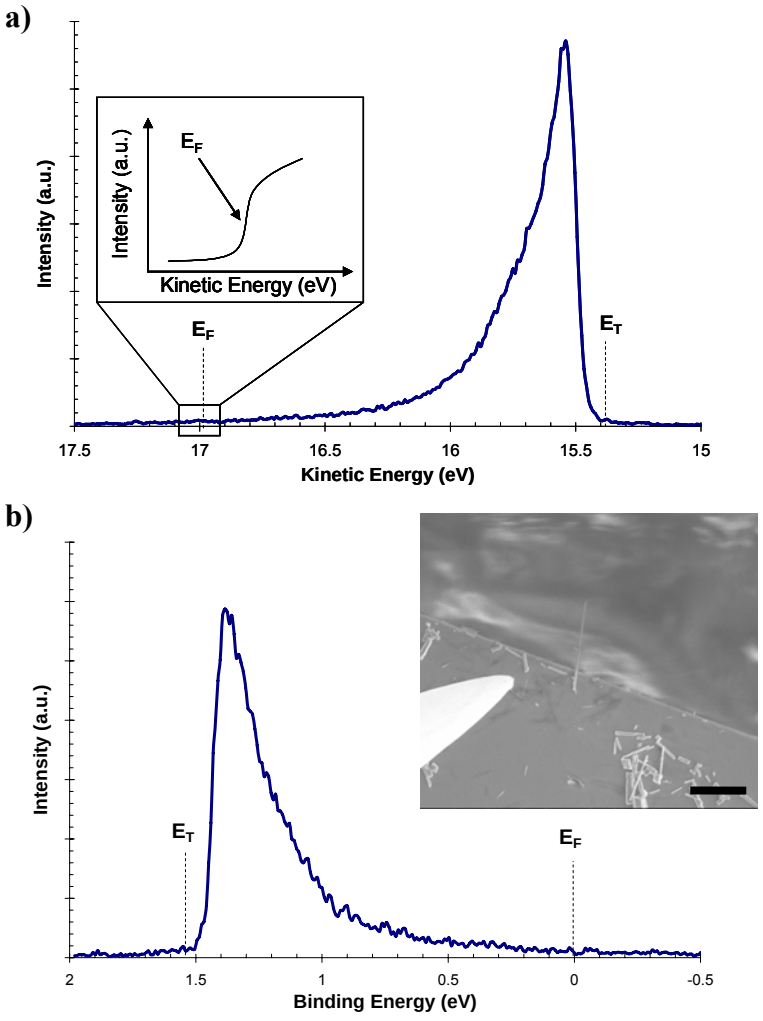

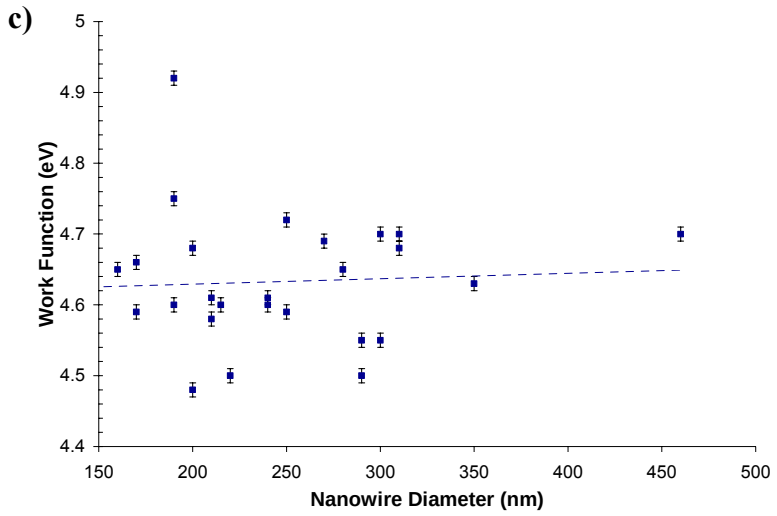


Figure 4.5: Photoelectron spectra of individual native ZnO nanowire. a) Spectrum as read by the detector in terms of the kinetic energies of the impacting electrons. b) The spectrum is plotted as a function of binding energy. The position of the Fermi level ($E_F$), which was measured from the Pt film in contact with the sample, is identified at 0eV binding energy and the photoelectron emission threshold ($E_T$) is also identified at 1.51eV. The work function ($\Phi$) of the nanowire can be deduced from $E_T$, and for this nanowire, the work function is calculated as 4.69eV. Inset is SEM image of ZnO nanowire which spectra was taken on, partially extending into lithographically patterned gap. Scale bar is 5μm. c) Distribution of $\Phi$ vs nanowire diameter for several different nanowires.

### 4.3.1 SURFACE SENSITIVITY OF NANOWIRE ELECTRONIC PROPERTIES

Native ZnO is intrinsically n-type, owing to its primary defects, zinc interstitials and oxygen vacancies. ZnO nanostructures also exhibit a native surface that is rich in excess zinc, which can serve as binding sites for adsorption of various organic and inorganic molecules. The high surface defect density of hydrothermally grown ZnO nanowires[91] has been reported to be as high as $10^{14}/cm^2$. Such surface defects can lead to electronic states that are both spatially and energetically localized and can be 'binding magnets' for adsorbed species, such as water, carbon dioxide and oxygen. Extrinsic

surface states that correspond to dangling bonds of such adsorbates energetically may lie within the band gap or overlap with continuum bulk states and trap holes or electrons, producing a space-charge layer[127]. The width of the space-charge layer (W) plays a critical role in the carrier dynamics of the nanowires, which in turn has a dramatic influence on the Schottky barrier. The depletion width or space-charge layer can be calculated according to equation 5.4:

$$W = \sqrt{(2\varepsilon_{ZnO}\Phi_s) / (eN_D)} \quad (5.4)$$

where $\varepsilon_{ZnO}$ is the dielectric constant of ZnO (8.66), $\Phi_s$ is the surface barrier potential or built-in potential (0.3eV), e is the charge of an electron and $N_D$ is the doping density of the material ($10^{17}/cm^3$). The depletion width can then be calculated as 54nm. The depletion width can be altered by electronegative adsorbates on the nanowire surface, such as water, which can both oxidize zinc interstitials and take up oxygen vacancies, effectively acting like a mask (Figure 4.6a). The inset to Figure 4.6a is a schematic of the depletion width of a typical nanowire (blue is the depletion layer, red is the conduction layer), illustrating how thick the depletion width is for a small diameter nanowire (d>150nm). To remove water vapour and other surface species ($CO_2$, $O_2$); the substrate was annealed in-*situ* at 300ºC for 1 minute. Figures 4.6b-c demonstrate spectra taken on individual nanowires before and after annealing. A shift of the valence band edge towards lower binding energies was detected, which was induced primarily by thermolysis of water vapour and detachment of depletive ions bound to the surface. The shift may also be attributed to the influence of the co-adsorption of water on the adsorption of another electron acceptor adsorbate[128]. In any of these mechanisms, thermal desorption of adsorbed water and other oxidizing species increased the density of bulk and surface oxygen vacancies, which in ZnO act as electron donors. The increase in

the number of oxygen vacancies caused electrons to become trapped in ‘f-center’ defects and accumulate negative charge at the surface, bending the bands slightly upward.

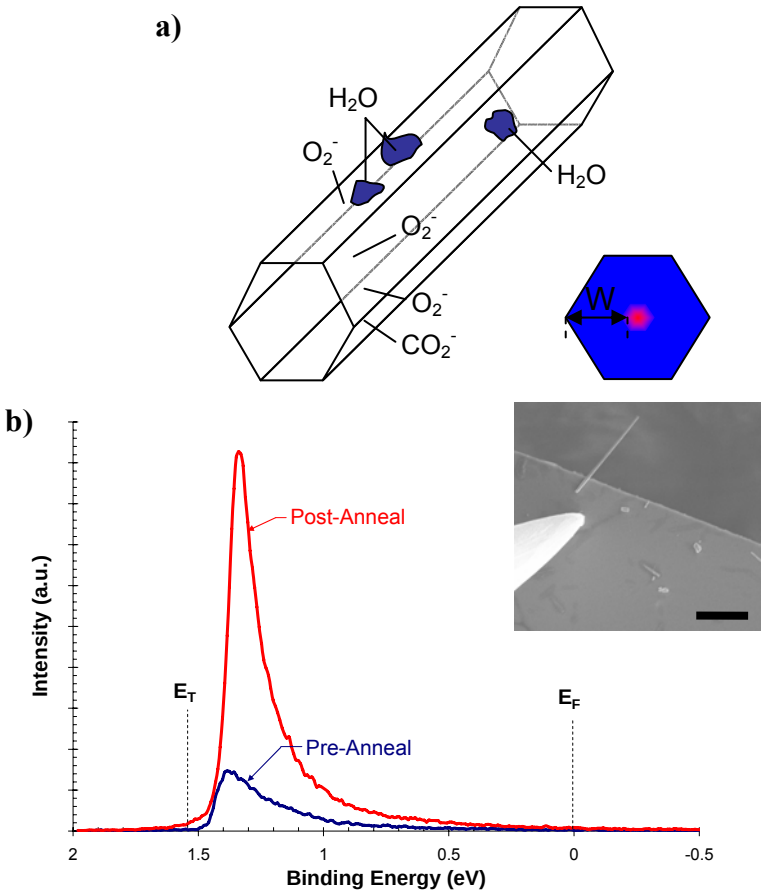

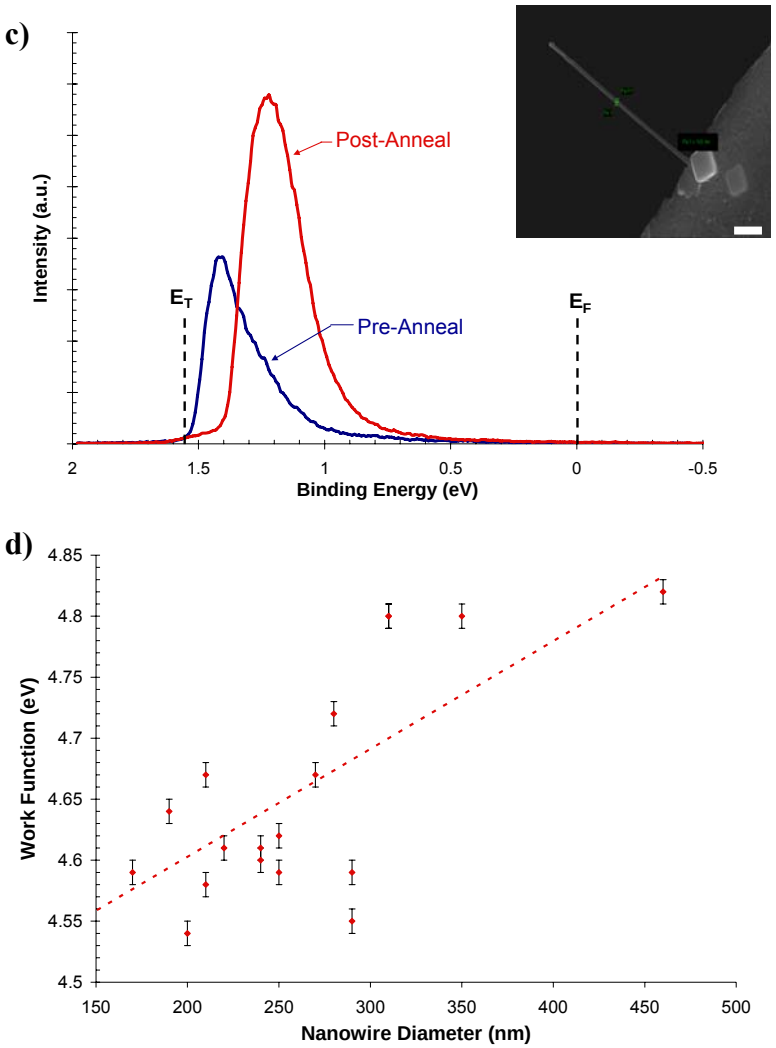


Figure 4.6: Photoelectron spectra after thermolysis of electronegative adsorbates. a) Schematic of nanowire surface before excision of water and other oxidizing species. Several typical photoemission spectra taken before (navy) and after (red) annealing native ZnO nanowires at 300°C for 1 minute as a function of binding energy. b) The electron emission threshold ($E_T$ = 1.53eV) and Fermi level ($E_F$ = 0) are labeled by dashed lines and the work function (Φ) for this nanowire is 4.67eV. Inset is SEM image of nanowire probed (diameter=270nm) where the scale bar is 5μm. c) A more dramatic energetic shift of the valence edge towards the Fermi level was detected for this particular nanowire. $E_T$ = 1.55eV for this nanowire and the corresponding work function was calculated to be 4.65eV. Inset is SEM image of nanowire probed (diameter=105nm) where the scale bar is 1μm. d) Distribution of Φ vs nanowire diameter after annealing for a number of nanowires.

Since the number of equilibrium surface and bulk oxygen defects in ZnO is a function of the environmental oxygen partial pressure and temperature[129,130], the samples were annealed in-situ at 300ºC for 1 minute in $10^{-5}$ torr dry oxygen. Figure 4.7b demonstrates spectra taken before and after annealing an individual ZnO nanowire in a partial pressure of oxygen. Upon introduction into the chamber, adsorbed oxygen molecules repopulated the surface vacancies, became ionized and induced a spectral shift away from the Fermi level. Large changes to the surface potential due to small changes in the partial pressure of oxygen are substantiated by the fact that the states near the Fermi level are mostly oxygen derived (Fig. 4.1b-c)[131]. Carbon in and on the nanowire surface may have also been responsible for the energetic shift; as oxygen is chemisorbed onto the surface and an electron is captured, a depletive $CO_2^-$ ion could have been formed. The decrease of surface oxygen vacancies effectively abated the number of filled (donor) intragap states, which in turn reduced the surface charge and band bending.

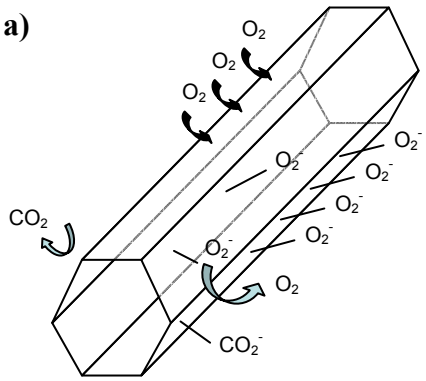

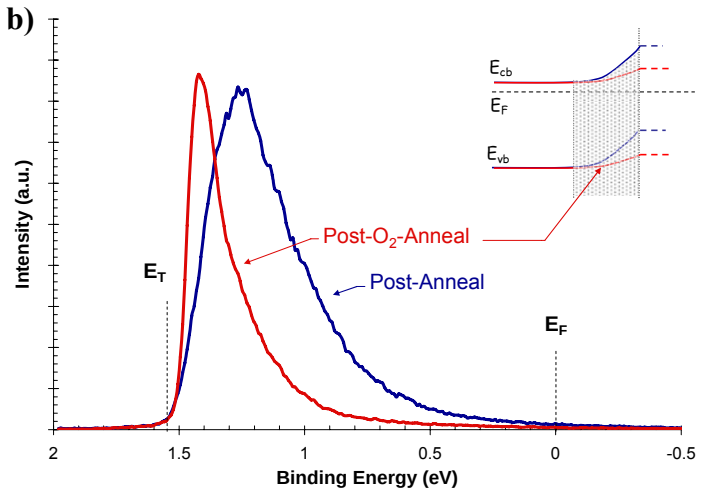
b)
Intensity (a.u.)
E_cb
E_F
E_vb
Post-O2-Anneal
Post-Anneal
E_T
E_F
2
1.5
1
0.5
0
-0.5
Binding Energy (eV)

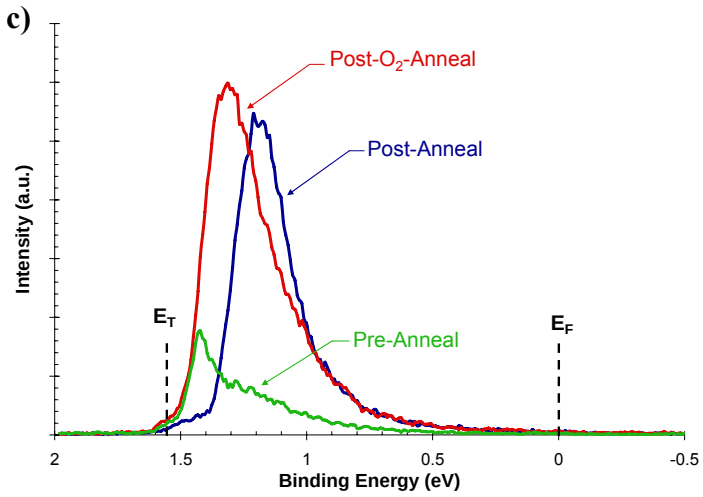
c)
Intensity (a.u.)
Post-O2-Anneal
Post-Anneal
Pre-Anneal
E_T
E_F
2
1.5
1
0.5
0
-0.5
Binding Energy (eV)

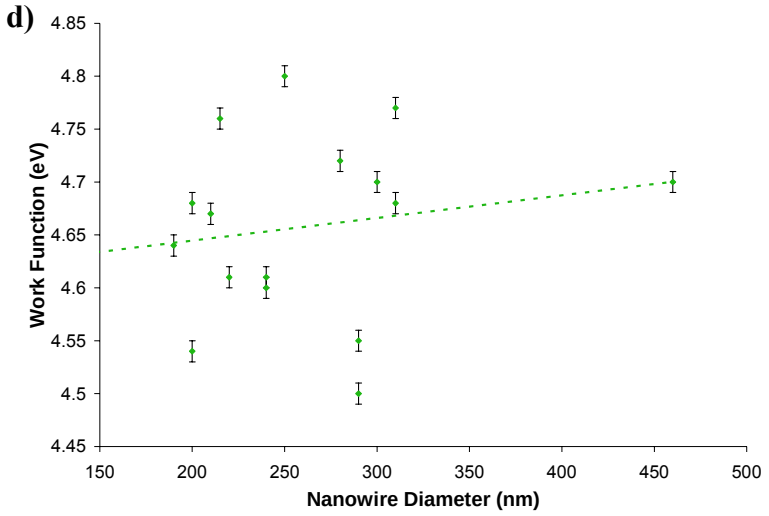


Figure 4.7: Photoelectron spectra after annealing in dry oxygen. a) Schematic of ionized oxygen at surface and several oxygen molecules being adsorbed. The oxygen recombines with surface oxygen vacancies and/or carbon to form a depletive carbon dioxide ion. b) Characteristic photoemission spectra taken before (navy) and after (red) annealing a ZnO nanowire in a partial pressure of oxygen (1e-5 torr $O_2$). An energetic shift away from the Fermi level of is detected, indicating band bending and a reduction in negative charge at the surface. $E_T$ was measured at 1.53eV for this nanowire (diameter=200nm) and the corresponding work function is calculated to be 4.67eV. Inset is schematic of band bending before (navy) and after (red) annealing in partial pressure of oxygen. c) Spectra of a native nanowire (green), post-annealed (blue), and annealed in a partial pressure of oxygen (red). A somewhat smaller movement of the valence edge away from the Fermi level was detected for this particular nanowire. $E_T$ was measured at 1.56eV for this nanowire (diameter =220nm) and the corresponding work function is calculated to be 4.64eV. d) Distribution of $\Phi$ vs nanowire diameter after annealing in oxygen for a number of nanowires.

To reverse the effect of adsorbed oxygen, nanowires were irradiated with UV light for an extended period. Figure 4.8a depicts a schematic of the photodesorption process where electron-hole pairs are created upon absorption of optical pulses. The scattered electrons can partake in a variety of processes such as scattering into surface states (capture). The photogenerated holes can migrate to the surface along the potential

slope created by band bending[132] and combine with surface state electrons, excising the electronegative surface species ($O_2^-$ and $CO_2^-$). Figure 4.8b displays the photoemission threshold ($E_T$) shift towards the Fermi level with extended exposure. This result was qualitatively consistent with generation of surface oxygen vacancies by annealing, whereby donated electrons get trapped in 'f-center' defects and acceptor molecules are discharged. The localized charge layer bent the bands upward again.

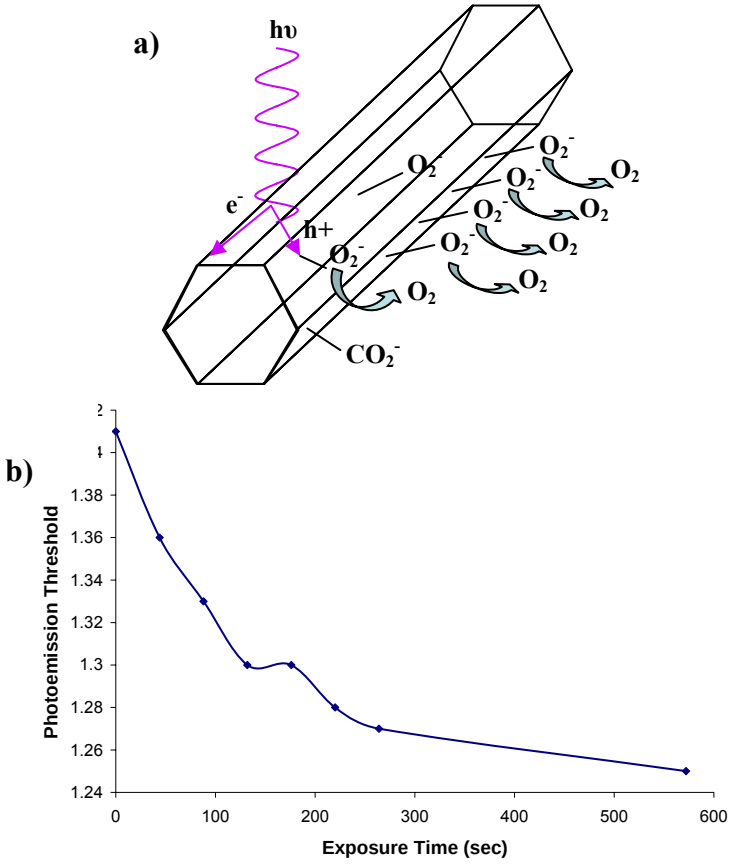


Figure 4.8: Photolysis of $O_2^-$ and $CO_2^-$ from the nanowire surface. a) Schematic of detachment of surface adsorbates from photogenerated holes. b) Prolonged exposure of ZnO nanowire to UV light induces the photoemission threshold ($E_T$) to shift towards the Fermi level, indicating upwards band bending, and discharge of chemisorbed acceptor ions.

These results illustrate the high sensitivity of the ZnO nanowire surface to molecular adsorption processes, which makes them ideal candidates to study other adsorption signatures such as those generated from covalently bound polar organic molecules.

## 4.4 MOLECULAR ENGINEERED NANOWIRE ELECTRONIC PROPERTIES

Adsorption of polar organic molecules on semiconductor surfaces has been shown to induce significant changes in the electrostatic potential and in turn, electron affinity and work function[133]. To date quantifying the degree SAMs exert on various physical properties has been challenging, as electrical contacts to passivated surfaces often degrade the organic monolayer. Correlating the interaction between adsorbed dipolar molecules and ZnO nanowires was perfectly suited for PES, as the technique gives a signal that is highly susceptible to molecule-substrate interactions as was seen in the last section. Self-assembled monolayers (SAMs) of various phosphonic acid (PA)-based molecules were chosen as a platform to study changes in $\Phi$ because PAs are strong binders to metal oxides[134] and have been shown to have a pronounced effect on the properties of ZnO thin films[114]. Additionally, the high density of surface binding sites in ZnO provides good accessibility for PA-based SAMs to target the surface and form up to three bonds at the interface[135], exerting a strong molecule-surface coupling. The layer of organic molecules with a net dipole moment perpendicular to the surface was grafted onto individual nanowires using the tethering by aggregation and growth (T-BAG) method[136].

### 4.4.1 FUNCTIONALIZATION OF NANOWIRES USING T-BAG METHOD

To functionalize the nanowires, the nanowire and Si substrate on which they rested were washed with deionized water and ethanol, dried with $N_2$, and cleaned with UV/Ozone for ten minutes. The substrates were then vertically submerged into 50μM solutions of benzylphosphonic acid (Alfa Aesar), (4-bromophenyl)phosphonic acid (Aldrich) prepared in tetrahydrofuran (THF) at 40°C and let saturate for approximately 9-10 hours. Slightly tempering the solvent above room temperature provided some thermal energy to assist the binding of the capping ligand to the surface as well as aid in evaporating the solvent. As the solvent slowly evaporated and the meniscus traversed the substrate, the molecules were transferred to the nanowire surfaces in inverse analogy to the Langmuir-Blodgett method, but without pressure. After functionalization, the samples were placed in an oven at 80°C for 24 hours to covalently bond the molecules[137]. Figure 4.9a displays a schematic of the self-assembly process of the molecules selectively adsorbing onto the nanowire surface. The samples were then washed thoroughly with THF, washed again with a solution of water/THF/triethylamine (10:3:1) to remove nonspecific molecules that aren't strongly chemisorbed to the nanowire surface, and washed again with THF. A control experiment was performed in the absence of the ligand under the same condition. To demonstrate the selective binding nature of the phosphonic acids to the nanowire surface, a high concentration of molecules (5mM) was dispersed into THF and an array of nanowires was functionalized using the T-BAG protocol except the substrate was not rinsed. Figure 4.9b displays large aggregates of molecules decorating the nanowire surface, clearly showing the SAMs are bound to the nanowires, albeit in this case, multilayered and in large aggregates.

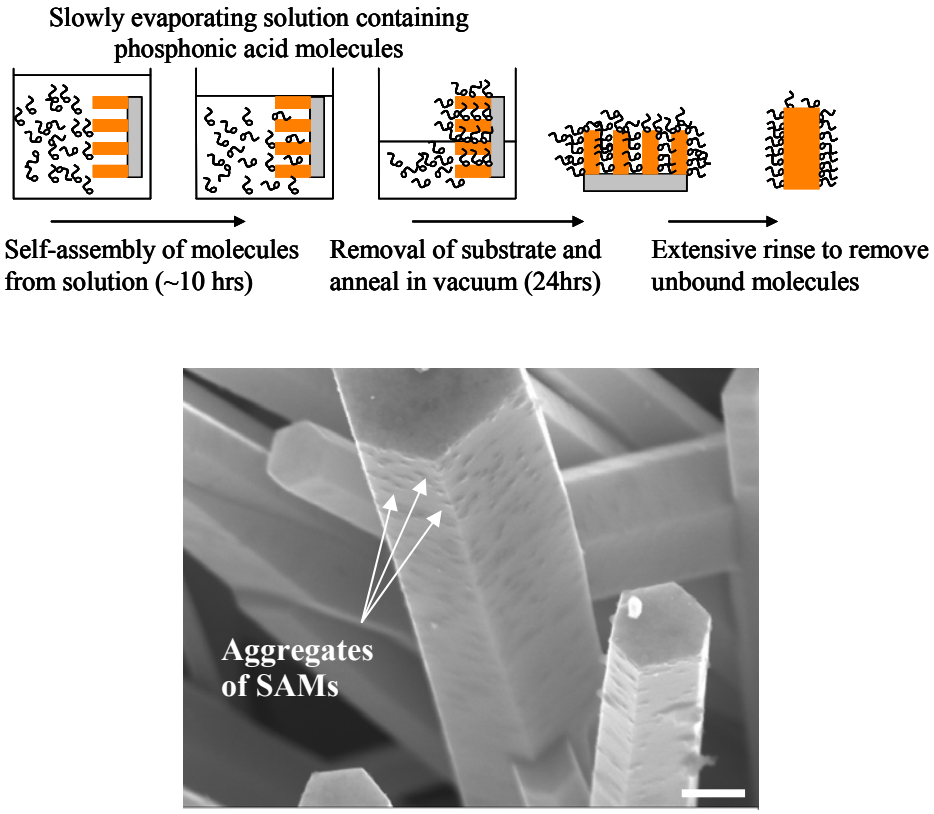


Figure 4.9: Functionalization of nanowires using T-BAG method. a) Schematic of self-assembly process using T-BAG method. Nanowire substrate is first immersed into a solution of phosphonic acids where the molecules self-assemble onto the surface as the solvent slowly evaporates with slight heat. After removal from solution, the substrates were annealed in an oven for 24 hours. After overnight heat treatment to bond the molecules to the surface, the samples are washed rigorously to remove any physisorbed molecules. b) High-magnification SEM image of a nanowire functionalized with higher concentration of 4-nitrophenyl phosphonic acid. Large clumps can be seen decorating the surface. Scale bar is 300nm.

The functionalized nanowires and substrate were then immediately loaded into the UHV system and interrogated the next day after the system had been fully pumped down. Figure 4.10a demonstrates spectra taken before and after functionalization with benzyl phosphonic acid (BPA), an electron-donating SAM with net dipole moment pointing

towards the surface. The spectra and $E_T$ for a native nanowire (navy curve) identified in Figure 4.10 at 1.59eV has clearly been shifted by 390meV to 1.20eV after passivation (red curve), indicating a large change in the effective work function. The shift of the work function arises from how the distribution of the dipoles at the interface perturbs the distribution of surface states, and in turn the net surface charge density[133]. To test whether the effect of the adsorbed molecule could be reversed, the substrate was annealed in-*situ* at 300°C for 2 minutes. Figure 4.10a shows the spectrum shift back towards its original state (green curve), but not fully recover due to residual hydrocarbon left from the SAM. The spectra did not fully recover but proved a near reversal of the molecular modified surface can be achieved by annealing. Figure 4.10b demonstrates a representative spectrum taken before (navy curve) and after functionalization (red curve) with 1-octyl phosphonic acid (OPA). OPA is also an electron-donor phosphonic acid but is an aliphatic system, and was selected to contrast the aryl-phosphonic acid SAMs used. Alkylphosphonic acids have been shown to have higher molecular packing densities and exert better coverage than aromatic SAMs. For the native nanowire, $E_T$ was identified in Figure 4.10b at 1.6eV. After functionalization, $E_T$ was spectroscopically shifted by 210meV to 1.40eV, indicating a smaller change in the effective work function than for BPA. The results of the nanowires functionalized with BPA and OPA are qualitatively consistent with the results of other electron donors at the surface (oxygen vacancies), where a shift towards the Fermi level was detected.

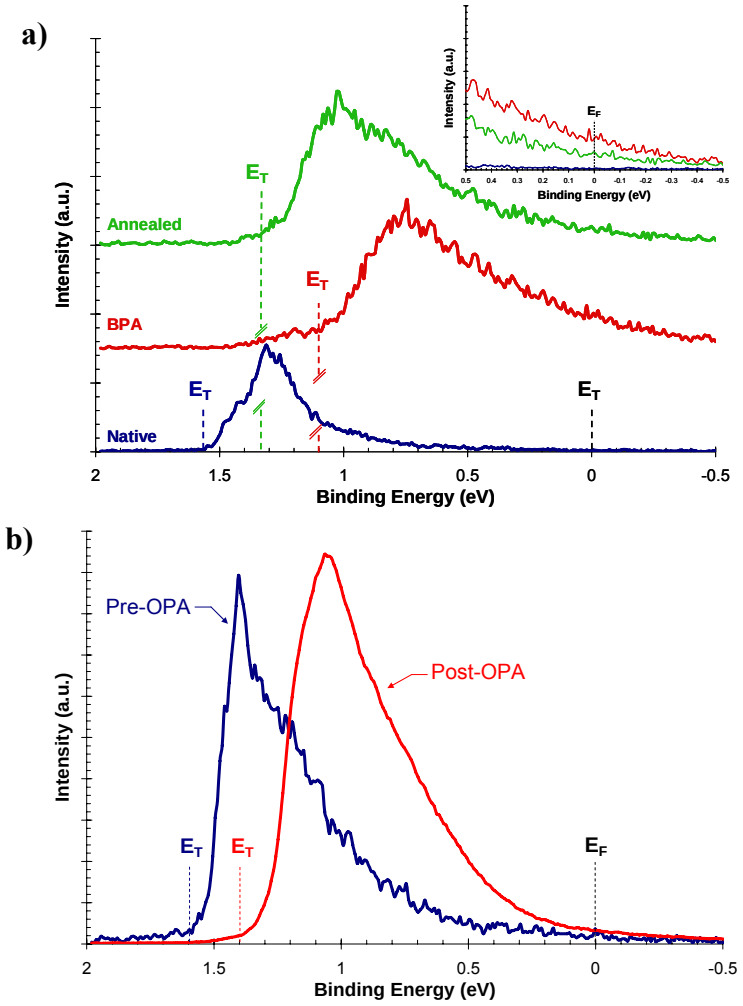


Figure 4.10: Spectra of ZnO nanowires coated with electron-donating SAMs. a) Photoemission spectrum taken on native nanowire (blue), after functionalization with benzyl phosphonic acid (red), and post annealing the functionalized nanowire in-*situ* (green). The spectra have been offset for clarity. The electron emission thresholds ($E_T$) for each are colour labeled by dashed lines (blue ~1.59eV, red ~1.20eV, green ~1.36eV). The spectra did not fully recover due to residual hydrocarbon left from the SAM. The work function is 4.61eV for native ZnO, 5.0eV for functionalized ZnO, and 4.84eV for a functionalized nanowire that has been annealed. The inset is a magnified view of the Fermi level for all 3 plots. The diameter of the nanowire probed was 150nm. b) Photoemission spectrum taken on clean nanowire (blue), and after functionalization with 1-octyl phosphonic acid (red). $E_T$ was been shifted by 0.2eV for the OPA functionalized wire and is colour labeled by a dashed line. The diameter of the nanowire probed was 170nm.

To gauge the binding mode(s) of the molecules to the nanowire surface, Fourier Transform Infrared (FTIR) spectroscopy in attenuated total reflectance mode (Thermo Mattson Infinity Gold) was used. For BPA, binding was evidenced by strong methylene asymmetric ($\upsilon_a(CH_2)$) and symmetric ($\upsilon_s(CH_2)$) stretching absorptions at 2918 and 2850 $cm^{-1}$, respectively (Figure 4.11a). The P-O stretching region between 1300 and 800 $cm^{-1}$ also demonstrated considerable changes in the number and frequencies of the P=O and P-O stretching bands (990-1010, 1130, 1260-1300$cm^{-1}$), which is indicative of a pronounced interaction of the phosphonate headgroup with the ZnO surface (Figure 4.11b). Also apparent is the disappearance of the peaks at 1200 and 950 $cm^{-1}$, which was also observed for phenylphosphonic acid on $ZrO_2$[138] and ITO[139]. The absence of these two bands, which were assigned to the P=O and P-O-H groups, indicate that the majority of the ligand is bound to the surface in a tridentate form, or involving all three oxygen atoms. For OPA, the methylene stretching absorptions show the binding was much less pronounced (Figure 4.11c). One possible case for the lack of strong binding could be the phosphonic acids reacted with the surface to make a phosphonate salt. Or another scenario could be the phosphonic acid formed a weak hydrogen bond to the surface and perhaps to neighboring molecules. The changes to the P-O stretching region also showed a relatively weak interaction, which corroborates the magnitude of the small spectroscopic shift. It should be noted however that since the ranges for the different P-O stretching peaks greatly overlap and depend on the degree of metal-binding, a definitive assignment of these bands was difficult.

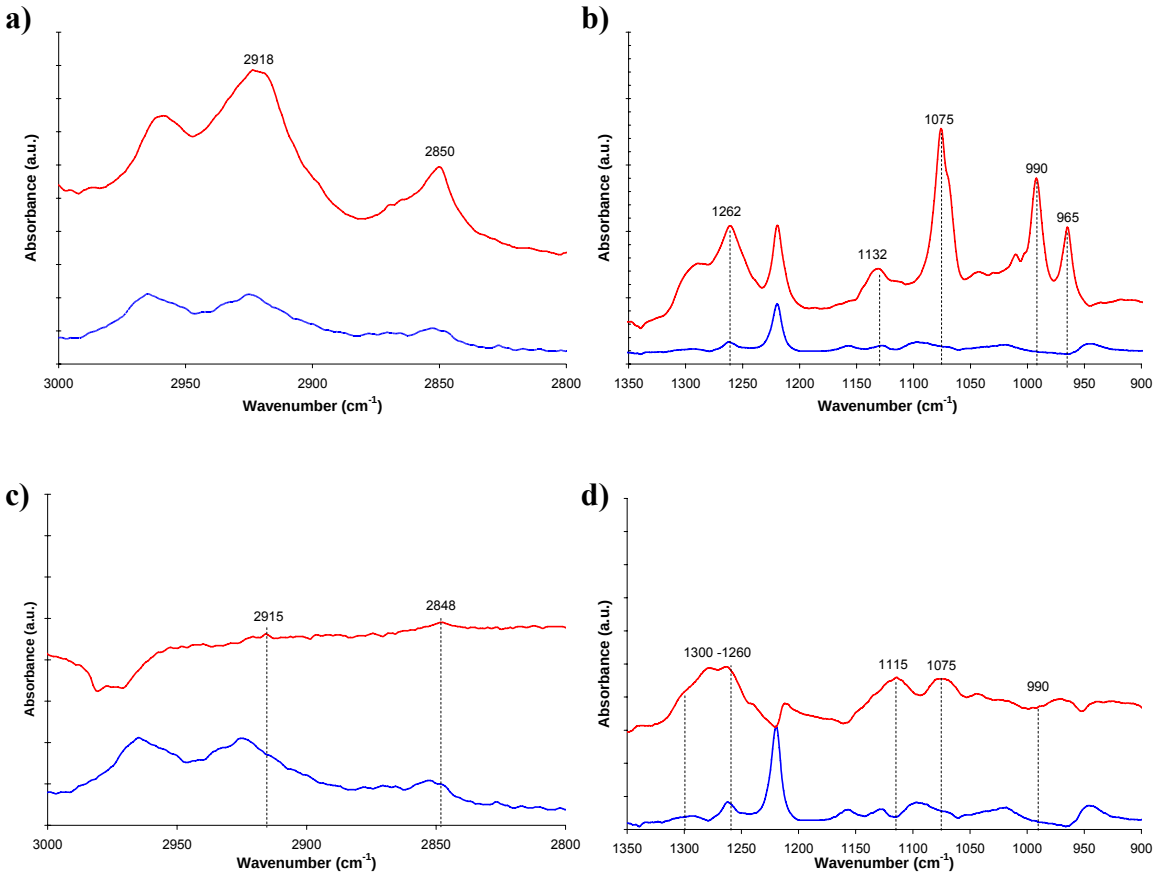


Figure 4.11: FTIR spectra of nanowires grafted with electron-accepting SAMs. a)-b) The nanowires functionalized with BPA (red) are compared to untreated (blue) nanowires. a) The methylene stretching vibration bands (2915 and 2848 $cm^{-1}$) clearly show enhanced stretching modes. b) The changes in the number and frequencies of the P=O and P-O stretching bands (990-1010, 1130, 1260-1300$cm^{-1}$) show tri-dentate surface bonding of the SAM to the nanowire surface. c)-d) The nanowires functionalized with OPA (red) are compared to untreated (blue) nanowires. c) The methylene stretching vibration bands (2915 and 2848 $cm^{-1}$) show no enhancement, indicating weak binding. d) The P-O stretching region (1300-800 $cm^{-1}$) also showed relatively weak interaction, which corroborates the spectroscopic results of a relatively weak interaction between the SAM and the nanowire surface.

To gauge if the dipolar effect could be shifted in the reverse direction using an oppositely charged dipole, an aryl electron-accepting phosphonic acid was grafted onto

the nanowire surfaces using the T-BAG method. 4-bromophenyl phosphonic acid (4-BrPA), an electron-withdrawing molecule pointing away from the surface with slightly stronger dipole moment than BPA[140] was adsorbed. Figure 4.12a shows a representative spectrum of a nanowire passivated with 4-BrPA. The spectra and photoelectron emission threshold for a clean nanowire (red curve) were shifted by 390meV after passivation (navy curve), indicating a large change in the effective work function. For the number of samples treated with 4-BrPA, the average shift was 390meV. The results were qualitatively consistent with generation of surface acceptors such as oxygen or water vapour, whereby a shift away from the Fermi level was detected.

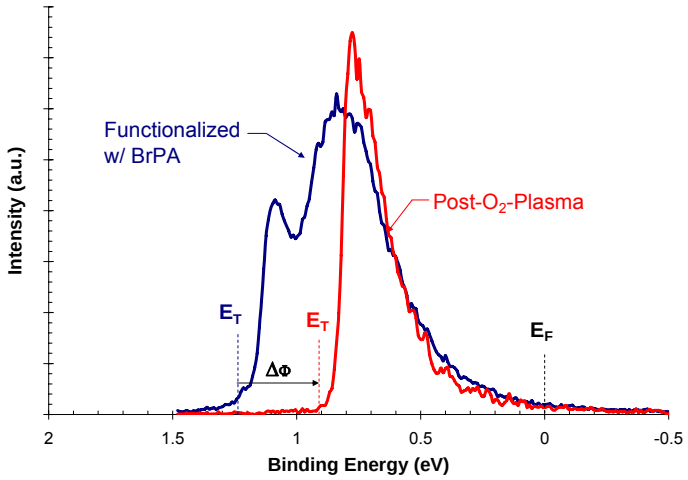


Figure 4.12: Spectrum of ZnO nanowire coated with electron-accepting SAMs. 4-bromophenyl phosphonic acid (4-BrPA) is an electron-accepting molecule with dipole moment similar to BPA. The nanowire functionalized with 4-BrPA (blue), when compared to its clean spectrum (red), showed an energetic shift of $E_T$, by nearly 0.4eV away from the Fermi level. The measurement was done on a nanowire with diameter of 160nm.

To assess the binding mode(s) of the molecules to the nanowire surface, FTIR-ATR was again employed. Nanowires functionalized with BrPA (red curves) experienced strong binding as depicted by the bands assignable to the C-H stretching modes of the methylene ($CH_2$) chain at 2917 and 2849 $cm^{-1}$ when compared to unfunctionalized nanowires (blue curves, Figure 4.13a). The P-O stretching region between 1300 and 800 $cm^{-1}$ also underwent substantial changes, consistent with the results for found for BPA (Figure 4.13b).

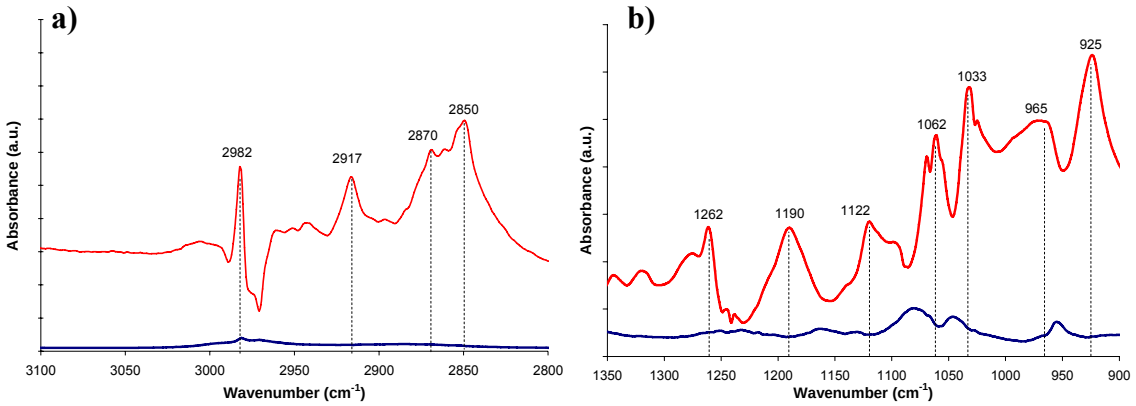


Figure 4.13 FTIR spectra of nanowires grafted with electron-accepting SAMs. a) Nanowires functionalized with 4-bromophenyl phosphonic acid (red) showed enhanced stretching modes for the methylene vibration bands (2915 and 2848 $cm^{-1}$) when compared to unfunctionalized nanowires (blue). b) Substantial changes to the number and frequencies of the P=O and P-O stretching bands were observed, similar to nanowires functionalized with BPA.

The changes in Φ due to adsorption of phosphonic acids stem from several molecular contributions. The first is a constant charge transfer effect from the phosphonic acid binding groups to the semiconductor surface that occurs from binding. The next is the effect of the electronegativity of the headgroup of the molecule. The headgroup contains the functional element that determines the net dipole moment of the entire molecule, and the direction in which it points (to or from the surface). The

relationship between the changes to the work function and the dipole moment of the molecule can be seen in equation 5.5. Equation 5.5 also depicts how changes in $\Phi$ depend not just on the dipole moment ($\mu_{sam}$), but also on the surface density of the molecules ($\Gamma$) and on their tilt relative to the surface normal ($\theta$):

$$\Delta\Phi = \Gamma \mu_{sam} \cos\theta / \varepsilon_r\varepsilon_o \quad (5.5)$$

where $\varepsilon_r$ is the relative dielectric constant and $\varepsilon_o$ is the vacuum permittivity. Herein, the para-substituents on the phenyl fragments were varied facilitating the change in work function. Changes in $\Gamma$ also were studied by contrasting an alkylphosphonic acid with the aryl systems, though the binding results were not as conclusive.

In addition to the dipolar effect, the molecules can also change the net surface charge and depletion width by modulating the distribution of surface states. This can occur if the active molecular levels (HOMO, LUMO) and surface states become equi-energetic and produce new energy levels, or if the surface states are changed. For example if an acceptor molecule has a low-lying LUMO, the molecule can combine with a filled surface state, and accept electrons from the electron-rich surface, which in turn would change the net surface charge density. Another case would be if the LUMO energy is between the valence band and $E_F$, and the surface states are split, where the levels that were initially below the LUMO energy will be shifted down, and those above the LUMO energy will be shifted up. This would cause a decrease in the band bending and since the energy levels measured in this experiment were close to the Fermi level, the changes in surface states from adsorbates measured here would have to be close to the band edges.

Tethering organic molecules to the surface of nanowires to control their electronic properties enables a hybrid system, where a new level of control can be used to influence Schottky barrier and magnitude of the piezoelectric output. When the passivated nanowires and metal electrode contact, the molecular layer can be viewed as modifying the Au vacuum level, even though the layer is adsorbed on the ZnO side. By forming an interfacial dipole layer at the metal-semiconductor interface, systematic changes in the barrier height during charge transfer can be effected. Herein, the work function of the nanowires was adjusted using PA-based SAMs. The effect of the molecules on the nanowire properties is shown below in Table 4.1 along with their dipole moments. The dipole moments were calculated with Spartan software (Wavefunction Inc.) in an equilibrium geometry in the ground state using the Hartree-Fock method and 3-21G* basis set. The measured work functions were substantially lower than their bulk values. This is not unexpected since edges associated with the faceted surfaces are expected to reduce Φ in a manner similar to that found for stepped or roughened surfaces[141]. Using molecular layers or annealing in various environments or even synergetic combinations of both enable a versatile approach to tune the barrier height and performance of the Schottky interface between the nanowires and metal electrode.

| | **BPA** | **OPA** | **4-BrPA** |
|---|---|---|---|
| **Molecular Structure** | 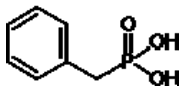 | 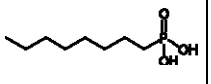 | 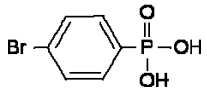 |
| **Dipole Moment (D)** | -1.36 | -1.45 | +1.97 |
| **Avg. Change in Φ (eV)** | +0.33 (±0.13) | +0.20 (±0.05) | -0.39 (±0.13) |

Table 4.1 Comparison of changes to ZnO nanowire work functions.

## 4.5 CONCLUSIONS

The goal of this spectroscopy project was to study how small molecules affect the electronic properties that control the interface between the hydrothermally grown ZnO nanowires and metal electrode, or the Schottky barrier. A general low photon energy photoelectron spectroscopy tool was developed to evaluate such electronic properties on individual nanowires. Systematic surface treatments were conducted to reveal the impact of environmental adsorbates on the nanowire work function as well as allow estimation of their effects on the electronic structure. The spectroscopically found defects corroborate the TEM images in Chapter 2. The technique was then extended to assess the interactions between various dipolar phosphonic acid-based SAMs and the nanowire work function. The molecular effect could be modulated using SAMs with different dipole strength and almost fully reversed by environmental substitution or heat.

Coating the nanowires with PA-based SAMs should improve the generator's performance by several modes. First, populating the surface with chemically bound molecules should generate more chemical homogeneity and in turn, more uniform properties from wire to wire. In one example of such an effect, the dipolar effect from the molecules changes the space-charge layer, which largely influences the resistivity of the nanowire. Since resistivity in turn influences the piezoelectric coefficient[70], nanowires that were previously contributing little or no energy when strained because of low resistivity may be able to output more energy. Second, by modulating the Schottky barrier height, nanowires that previously were only "leaking" small amounts of current, may now have a barrier height that is high enough to hold the charges from leaking.

The work studied in this chapter on individual ZnO nanowires provides a novel diagnostic technique that lends itself to the study of other materials and offers sufficient versatility and speed to probe spatially localized doping regions along an individual 1-D nanostructure. The method can be easily combined with other types of single wire or tube optical measurements such as Raman or Rayleigh and electrical measurements. Additionally the technique may also supply new insights into novel doping techniques for 1-D metal-oxide nanostructures based on molecular adsorption. Future studies with this technique may also shed light on the diameter dependence of surface states, where according to x-ray absorption near-edge structure (XANES) spectra of ZnO nanowires, when the diameter is decreased, the effect of surface states are greatly enhanced[142]. Further correlating the spectroscopy measurements on individual nanowires with atomic force microscopy (AFM) measurements of energy generation may yield a more quantitative analysis on the relationship between a molecular engineered surface and the amount of the energy generated. In addition, dynamic testing of the molecular layer over time would need to be completed to determine how well the SAMs withstand repeated contact and abrasion. Construction of single-nanowire FETs may also generate more insight into quantitative changes to the barrier height but extreme care must be taken not to contaminate or damage the passivation layer during processing. Analysis on the surface binding of the phosphonic acid in a setting that would resemble an implanted AICD lead must also be performed. The humidity of the environment and temperature may degrade the molecular contact over time and reduce the energy generated thereby limiting its long term performance. Additional progress using one or a combination of the synthetic conditions, annealing treatments and molecular layers should provide improvement of the device performance as well enable a significant advance in complexity and functionality of the energy generators.

# Chapter 5: Conclusions and Outlook

## 5.1 CONCLUSIONS

The present work has focused on development of a nanostructured device to efficiently convert the kinetic movement of the heart into electrical power with the aim of recharging an AICD/BVP battery. While piezoelectric generators have been researched for decades, implantable piezoelectric generators are just beginning to be explored. Using nanostructured piezoelectrics as a means to convert the energy of the body may in the coming years represent a paradigm shift from battery dependant AICD modules to completely autonomous functional systems. This thesis makes progress towards harvesting the energy of the heart using nanostructured piezoelectric devices that can be incorporated into conventional AICD leads.

An optimized two-step method was first developed to hydrothermally grow highly oriented piezoelectric nanowires of zinc oxide on plastic substrates. The synthetic technique was based on a controlled nucleation and growth process that was selectively controlled to produce a nanowire array that would produce the max amount of energy. The catalyst, substrate and reaction conditions were systematically varied to control key parameters such as the density, nanowire diameter and aspect ratio (length to width), all of which are critical to the device energy density. The growth procedure is at low temperature, possesses the ability to scale up, and is environmentally benign. Characterization of the nanowire arrays revealed the high degree of orientation and high-aspect ratio, as well as the inclusion of defects into the nanowire lattice, which makes them more resistive and better piezoelectrics.

A piezoelectric generator comprised of PVDF was first tested on a system that mimicked a failing right ventricle. The polymeric generator returned a somewhat small output per unit area, such that it would take approximately 50 years to fully recharge an AICD battery. In order to raise output without sacrificing the cost of harvesting, oriented piezoelectric nanowires grown on a flexible plastic device were investigated. The device was constructed from interlocking silicone rubber pieces, so they fit together like a "sandwich". One side of the device was patterned with buckled metal electrodes that change shape when the device is flexed. The shape changes drove the nanowires grown on them up and down into the other side of the sandwich that was coated in metal. When the compressed sides of the deformed piezoelectric nanowires touched the electrode, a forward-biased Schottky diode was created. The result enabled an external current to flow through the electrode, stabilizing the nanowires built up potential. When the device was relaxed, the buckles retracted in amplitude and broadened their wavelength, relieving the nanowires from strain. Compression tests of one of the ridges on the bottom substrate outputted on average ~6.5pW. Considering the size of the generator, an active power per unit area of ~0.5nW/cm$^2$ was achieved. Although this device has produced respectable power outputs at little to no cost in the COH, more power still needed to be withdrawn to fully recharge an AICD battery. To increase the output from the nanostructured generator, a mechanics model was developed to investigate the influence of geometrical properties on the piezoelectric response. From the model output, insight was gained as to how to structure the nanowire array within the latitude of the synthesis outlined previously to maximize the power output.

To further improve the piezoelectric output of the nanowires, the barrier height or Schottky contact between the hydrothermally grown nanowires and neighboring

electrode was modulated. To investigate the properties that dictate the barrier size between the two surfaces, a novel low energy photoemission technique was developed. The technique permitted observation of the average work function for an individual nanowire. Systematic surface treatments were conducted to reveal the impact of environmental adsorbates on the work function as well as allow estimation of their effects on the surface densities of states. The spectroscopically found defects corroborate the TEM images in Chapter 2 and support the conclusion of highly resistive nanowires with several atomic defects. The photoemission technique was then extended to assess the interactions between various dipolar phosphonic acid-based SAMs and the nanowire work function. The phosphonic acid-based SAMs were found to be bound to the surface in a tri-dentate mode and packed in an organized monolayer fashion. Tethering organic molecules to the surface of nanowires to control their electronic properties enabled another level of control to influence the Schottky contact and piezoelectric output and improve the generator's performance.

## 5.2 OUTLOOK

There is a large scope for further developing technologies that can harness the energy of the heart. The platform described here represents an efficient path but there is still room for alternative approaches that will aid in energy conversion. For instance, one innovative approach would be to use a thin "pericardium-like" sac of plastic that is embedded with flexible networks of piezoelectrics and encircles the heart, stretching with each beat. Such a system would also provide an innovative framework to perform myocardial tensiometry and when combined with telemetric measures, relay real-time information about global cardiac outputs. Another approach would be one that would assist the cardiac muscle in performing negative work, analogous to regenerative braking

in hybrid cards, where the energy dissipated in diastole would drive a micro-generator. This type of technology could selectively engage during diastole, which would maintain the low COH, and if combined with feedback also give real-time cardiac output measurements. Granted, the micro-generator would require sophisticated lithographic techniques to connect and transfer into the curvilinear surface of the lead, and friction of the gear train within the plastic housing may hinder the performance.

Each of the individual chapters can be further extended to improve the energy generator. Further extension of the growth optimization may lead to even further enhancements of the energy generator. For example, by extending the developed procedure (seed deposition, growth time, solution composition, etc) the oriented nanowires may act as efficient templates for growth of more complex hierarchical architectures such as branched crystallites. Such higher-order crystal structures produced in multi-stage chemical reactions could yield more deflection and energy production without compromising additions to volume or AICD lead stiffness. Moreover, such a step-wise synthesis could extend to mixed-material systems such as cadmium-sulfide (CdS) nanorods/wires on ZnO crystal cores. Such mixed material super-structures offer both the potential to extract even higher piezoelectric responses and more resistance to fatigue. Additionally, core-shell structures may also offer higher piezoelectric potentials by inducing mismatch strains between the core and shell and also add stiffness to the wires, increasing their lifetimes. Lastly, augmenting solely the growth time may yield hollow microtubes or nanotubes, which would act as efficient pathways for higher capacity nanocomposites or templates for composite materials with other piezoelectric nanoparticles adsorbed onto the surface.

Future research on the device itself can be divided into a three areas: 1) lifetime and fatigue behavior of the device, 2) more comprehensive analysis of the mechanics of the device, 3) methods to augment the power output of the device without compromising the COH. The first focus of research studying the lifetime of the developed devices should include periodic SEM studies of the nanowire surface to identify possible mechanisms of failure such as wire fracture from the electrodes and degradation of the electrode buckling. Currently there is no literature available on fatigue behavior of nanowires and only one study on carbon nanotubes, which when compression-tested as an ensemble, exhibited viscoelastic behavior. If this effect is also present for the nanowires, the device may exhibit lifetimes exceeding those of conventional bulk piezoelectric energy generators. Actuators based on bulk polycrystalline piezoelectrics such as PZT have lasted upwards of $10^9$ cycles with less than a 1% loss of performance. If the device was able to continuously produce output for the same number of cycles loaded at 1.1Hz, it would last approximately 30 years. The degree of polarization during and post-testing should also be locally investigated on the nanowires with AFM. Wear tests on the buckled electrodes and polymer substrates may also elucidate possible points of failure and ultimately lead to mechanically tougher or longer lasting design concepts. The second focus should be geared towards development of more comprehensive analysis of the mechanics of the device and the modes of deformation during systole. Solving the analytical solutions to the complex nonlinear electro-mechanical systems during systole may yield guidelines to further tune the synthesis for enhanced device performance. Additionally, finite element analysis (FEA) of the interface between the polymer substrate and the buckled metal films may provide new insights into other potential failure modes that may impede performance. The third aim to raise the power output of the device without compromising the COH can include an umbrella of

approaches. First, one avenue to pursue would be to exchange the spacer layer or substrate from PDMS to PVDF. Replacing the PDMS with PVDF would enable every part of the device a functionality that could produce energy, rather than just the nanowires on the raised ridges. Or changing the device design to include the nanowires that are currently impacting the spacer layer would also raise the power density. Yet another variant would be to embed the nanowires in PVDF and use a composite material as shown in Figure 1.6 as the interlocking pieces. In addition to exhibiting increased efficiency and possibly condensing the charging time, hybrid biphasic structures also possess better mechanical toughness than the individual phases that comprise them, which would permit a longer lifetime. Second, using nanowires with larger piezoelectric coefficients such as $BaTiO_3$ or $KNbO_3$ may also increase the energy density. However synthetic techniques to grow 1-D perovskite materials have not been able to produce an ordered array, much less at low temperature on plastic. Nonetheless, new device designs and assembly techniques to integrate such nanowires may ultimately deliver enhanced performance. Third, controlling the interface between the nanowires and neighboring contacts by modulating the barrier height can also permit higher piezoelectric responses.

Further correlating the spectroscopy measurements on individual nanowires with atomic force microscopy (AFM) measurements of energy generation[42] may yield a more quantitative analysis on the relationship between a molecular engineered surface and the amount of the energy generated. In addition, dynamic testing of the molecular layer over time would need to be completed to determine how well the SAMs withstand repeated contact and abrasion. Construction of single-nanowire FETs may also generate more insight into quantitative changes to the barrier height but extreme care must be taken not to contaminate or damage the passivation layer during processing. Analysis on the

surface binding of the phosphonic acid in a setting that would resemble an implanted AICD lead must also be performed. The humidity of the environment and temperature may degrade the molecular contact over time and reduce the energy generated thereby limiting its long term performance. Additional progress using one or a combination of the synthetic conditions, annealing treatments and molecular layers should provide improvement of the device performance as well enable a significant advance in complexity and functionality of the energy generators.

# References


1. Elixhauser A, Yuk A, Steiner C, et al. The top ten conditions in which patients are admitted to the hospital. Hospitalization in the United States: HCUP Fact Book NO. 1, Rockville, MD: Agency for Healthcare research and Quality; 200.
2. Bristow M, Saxon L, Boehmer J, Krueger S, Kass D, De Marco T, Carson P, DiCarlo L, DeMets D, White B, DeVries D, Feldman A. Cardiac-resynchronization therapy with or without an implantable defibrillator in advanced chronic heart failure. N. Engl. J Med. 2004, 350:21, 2140-2150.
3. Moss A, Zareba W, Hall W, et al, for the Multicenter automatic defibrillator implantation trial II. Prophylactic implantation of a defibrillator in patients with myocardial infarction and reduced ejection fraction. N. Engl. J. Med. 2002, 346, 877-883.
4. Barry GH, Lee KL, Mark DB, et al. Amiodarone or an implantable cardioverter–defibrillator for congestive heart failure. N. Engl. J. Med. 2005, 35, 225-237.
5. Bristow MR, Saxon LA, Boehmer J, et al. Cardiac-resynchronization therapy with or without an implantable defibrillator in advanced chronic heart failure. N. Engl. J. Med. 2004, 350, 2140-2150.
6. Cleland JF, Daubert JC, Erdmann E, et al. The effect of resynchronization on morbidity and mortality in heart failure. N. Engl. J. Med. 2005, 352, 1539-1549.
7. Hauser RG, Hayes D, Parsonnet V, et al. Feasibility and initial results of an Internet-based pacemaker and ICD pulse generator and lead registry. Pacing and Clinical Electrophys. 2001, 24, 82–7.
8. Hauser RG. The Growing Mismatch Between Patient Longevity and the Service Life of Implantable Cardioverter-Defibrillators. J. Am. Coll. Cardio. 2005, 45:12, 2022–2025.
9. Wild DM, Fisher JD, Kim SG, Ferrick KJ, Gross JN, Palma EC. Pacemakers and implantable cardioverter defibrillators: Device longevity is more important than smaller size: The patient's viewpoint. Pacing and Clinical Electrophys. 2004, 27:11, 1526-1529.
10. Webster J. Design of Cardiac Pacemakers. IEEE Press 1995, New York, NY.
11. Voigt A. Device Implant Infections Way Up. Heart Rhythm Society 2006, Scientific Sessions.
12. Bracke FA, Meijer A, van Gelder LM. Lead extraction for device related infections: a single-centre experience. Europace. 2004, 6, 243–7.
13. Parsonnet V, Driller J, Cook D, Rizvi SA. Thirty-One Years of Clinical Experience with "Nuclear-Powered" Pacemakers. Pacing and Clinical Electrophys. 2006, 29:2, 195-200.
14. Starner T, Paradiso JA. Human generated power for mobile electronics. Low-Power Electronics, CRC Press, 2004, 45, 1-35.
15. Donelan JM, Li Q, Naing V, Hoffer JA, Weber DJ, Kuo AD. Biomechanical Energy Harvesting: Generating electricity during walking with minimal user effort. Science 2008, 318, 807-810.
16. Shenck NS, Paradiso JA. Energy scavenging with shoe-mounted piezoelectrics. IEEE Micro 2001, 21, 30-42.

17. Hausler E, Stein L, Harbauer G. Implantable physiological power supply with PVDF film. Ferroelectrics 1984, 60, 277–282.
18. Ramsay MJ, Clark WW. Piezoelectric energy harvesting for Bio-MEMS applications. Smart Structures and Materials, Proc. Of SPIE. 2001, 4332, 429-438.
19. Wang XD, Liu J, Song J, Wang Z. Integrated Nanogenerators in Biofluid. Nano Lett. 2007, 7, 2475-2479.
20. Haber I, Metaxas DN, Geva T, Axel L. Three-dimensional systolic kinematics of the right ventricle. Amer. J. Physiol. Heart Circ. Physiol. 2005, 289, H1826–H1833.
21. Feldman MD, Chen SC, Aguilar CA, Korgel BA, Lee DC et al, U.S. Patent Pending PCT/US2008/000114, filed 1/4/08.
22. Parsonnet V, Myers GH, Zucker R, Lotman H, Asa MM. A cardiac pacemaker using biologic energy sources. ASAIO Trans 1963, 9, 174–177.
23. Konikoff J. In vivo energy sources. Digest of 7th Int Conf BME, 1967;517.
24. Roth W. Bioenergy electrical power source. Digest of 7th Int Conf BME, 1967;518.
25. Lewin G, Myers GH, Parsonnet V, Raman KV. An improved biological power source for cardiac pacemakers. ASAIO Trans 1968; 14:215–219
26. Myers GH, Parsonnet V, Zucker IR, Lotman, HA, Asa MM. Biologically energized cardiac pacemaker. IEEE Trans. Biomed. Electron. 1963, 10, 83.
27. Ariav A. Method and apparatus for body generation of electrical energy. U.S. Patent 7,081,683.
28. Rasor NS, Spickler JW. Self powered pacers and stimulators. U.S. Patent 3,943,936.
29. Spitzer DE. Apparatus for powering a body implant device. U.S. Patent 4,453,537.
30. Schroeppel EA. Pacing lead with piezoelectric power generating means. U.S. Patent 4,690,143.
31. Mitcheson PD, Miao P, Stark BH, Yeatman EM, Holmes AS, Green TC. Sens. Actua. A. 2004, 115, 523-529.
32. Tashiro R, Kabei N, Katayama K, Tsuboi F, Tsuchiya K. Development of an electrostatic generator for a cardiac pacemaker that harnesses the ventricular wall motion. Jpn. J Artif Organs 2002, 5, 239–245.
33. Uchino K, Giniewicz JR. Micromechatronics. Marcel Dekker, New York, 2003.
34. Roundy S, Wright PK. A piezoelectric vibration based generator for wireless electronics. Smart Mater. And Struc. 2004, 13, 1131-1142.
35. Saito Y, Takao H, Tani T, Nonoyama T, Takatori K, Homma T, Nagaya T, Nakamara M. Lead-free piezoceramics. Nature 2004, 432, 84-87.
36. Rankin C, Chou CH, Conklin D, Bonnell DA. Polarization and Local Reactivity on Organic Ferroelectric Surfaces: Ferroelectric Nanolithography Using Poly(vinylidene fluoride). ACS Nano 2007, 1:3, 234-238.
37. Brown RH. Energy Generation using Piezo Film. ATOCHEM Sensors LTD. 1999
38. Cook-Chennault KA, Thambi T, Sastry AM. Powering MEMS portable devices-a review of non-regenerative and regenerative power supply systems with special emphasis on piezoelectric energy harvesting systems. Smart Mater. And Struc. 2008, 17, 043001-33.
39. Klicker KA, Biggers JV, Newnjam RE. Composites of PZT and epoxy for hydrostatic transducer applications. J. Amer. Ceram. Soc. 1981, 64, 5.

40. Wickramasinghe VK, Hagood NW. Material characterization of active fiber composites for integral twist-actuated rotor blade application. Smart Mater. Struct. 2004, 13, 1155-1165.
41. Suyal G, Colla E, Gysel R, Cantoni M, Setter N. Piezoelectric response and polarization switching in small anisotropic perovskite particles. Nano Lett. 2004, 4:7, 1339-1342.
42. Wang ZL, Song JH. Piezoelectric nanogenerators based on zinc oxide nanowire arrays. Science 2006, 312, 242-246.
43. Wang Z, Hu J, Suryavanshi AP, Yum K, Yum MF. Voltage generation from individual BaTiO3 nanowires under periodic tensile mechanical load. Nano Lett. 2007, 7:10, 2966-2969.
44. Cui Y, Lieber CM. Functional Nanoscale Electronic Devices Assembled Using Silicon Nanowire Building Blocks. Science 2001, 291, 851-853.
45. Xiang J, Vidan A, Tinkham M, Westervelt RM, Lieber CM. Ge/Si nanowire mesoscopic Josephson junctions, Nature Nano. 2006, 1, 208-213.
46. Yu C, Hao Q, Saha S, Shi L, Kong X, Wang ZL. Integration of Metal Oxide Nanobelts with Microsystems for Nerve Agent Detection. Appl. Phys. Lett. 2005, 86, 063101:1-3.
47. Law M, Greene LE, Johnson JC, Saykally R, Yang P. Nanowire dye-sensitized solar cells. Nature Mater. 2005, 4, 455-459.
48. Tian B, Zheng X, Kempa T, Fang Y, Yu N, Yu G, Huang J, Lieber CM. Coaxial silicon nanowires as colar cells and nanoelectronic power sources. Nature 2007, 449, 885-890.
49. Abramson A, Kim W, Huxtable S, Yan H, Wu Y, Majumdar A, Tien CL, Yang P. Fabrication and Characterization of a Nanowire/Polymer-based Nanocomposite for a Prototype Thermoelectric Device. J. Microelectromech. Sys. 2004, 13, 505.
50. Huang M, Mao S, Feick H, Yan H, Wu Y, Kind H, Weber E, Russo R, Yang P. Room-temperature ultraviolet nanowire nanolasers. Science 2001, 292, 1897-1899.
51. Law M, Sirbuly D, Johnson J, Goldberger J, Saykally R, Yang P. Ultralong nanoribbon waveguides for sub-wavelength photonics integration. Science 2004, 305, 1269-1273.
52. Avouris P, Chen J. Nanotube electronics and optoelectronics. Mater. Today 2006, 9, 45-54.
53. Xia YN, Yang PD, Sun YG, Wu YY, Mayers B, Gates B, Yin YD, Kim F, Yan YQ. One-dimensional nanostructures: Synthesis, characterization, and applications. Adv. Mater. 2003,15:5, 353-389.
54. Wagner RS, Ellis WC. Whisker Technology. Appl. Phys. Lett. 1964, 4, 89.
55. Trentler TJ, Hickman KM, Geol SC, Viano AM, Gibbons PC, Buhro WE. Solution-Liquid-Solid growth of crystalline III-V semiconductors – an analogy to Vapor-Liquid-Solid growth. Science 1995, 270, 1791-1794.
56. Greene LE, Law M, Tan DH, Montano M, Goldberger J, Somorjai G, Yang P. General Route to Vertical ZnO Nanowire Arrays Using Textured ZnO seeds. Nano Lett. 2005, 5:7, 1231-1236.

57. Vayssieres L. Growth of arrayed nanorods and nanowires of ZnO from aqueous solutions. Adv. Mater. 2003, 15:5, 464-466.
58. Hung CH, Whang WT. A novel low-temperature growth and characterization of single crystal ZnO nanorods. Mater. Chem. Phys. 2003, 82, 705-710.
59. Greene LE, Yuhas BD, Law M, Zitoun D, Yang P. Solution-Grown ZnO Nanowires. Inorg. Chem. 2006, 45, 7535-7543.
60. Zhou J, Xu N, Wang ZL. Dissolving behavior and stability of ZnO wires in biofluids: A study on biodegradability and biocompatibility of ZnO nanostructures. Adv. Mater. 2006, 18, 2432-2435.
61. Urban JJ, Yun WS, Gu Q, Park H. Synthesis of single-crystalline perovskite nanorods composed of barium titanate and strontium titanate. J. Amer. Chem. Soc. 2002, 124:7, 1186-1187.
62. Magrez A, Vasco E, Seo JW, Dieker C, Setter N, Forro L. Growth of single-crystalline KNbO3 nanostructures. J. Phys. Chem. B 2006, 110, 58–61.
63. Sun Y, Rogers JA. Inorganic Semiconductors for flexible electronics. Adv. Mater. 2007, 19, 1897-1916.
64. Sun YG, Rogers JA. Fabricating semiconductor nano/microwires and transfer printing ordered arrays of them onto plastic substrates. Nano Lett. 2004, 4, 1953-1959.
65. Yerushalmi R, Jacobson ZA, Ho JC, Fan Z, Javey A. Large scale, highly ordered assembly of nanowire parallel arrays by differential roll printing. Appl. Phys. Lett. 2007, 91, 2031041-3.
66. Meitl MA, Zhu ZT, Kumar V, Lee KJ, Feng X, Huang YH, Adesida I, Nuzzo RG, Rogers JA. Transfer printing by kinetic control of adhesion to an elastomeric stamp. Nature Mater. 2006, 5, 33-38.
67. Huang Y, Duan X, Wei Q, Lieber CM. Directed Assembly of One-Dimensional Nanostructures into Functional Networks. Science 2001, 291, 630-633.
68. Yu G, Cao A, Lieber CM. Large-area blown bubble films of aligned nanowires and carbon nanotubes. Nature Nano. 2007, 2, 372-377.
69. Jin S, Whang D, McAlpine MC, Friedman RS, Wu Y, Lieber CM. Scalable Interconnection and Integration of Nanowire Devices without Registration. Nano Lett. 2004, 4, 915-919.
70. Scrymgeour DA, Hsu JWP. Correlated Piezoelectric and Electrical Properties in Individual ZnO Nanorods. Nano Lett. 2008, 8, 2204-2209.
71. Stal S, Spira M. Plastic Surgery. Lippincott- Raven 1997, Philadelphia, PA.
72. Wang ZL. Nanowires and Nanobelts Materials, Properties and Devices: Nanowires and Nanobelts of Functional Materials-Volume II. Kluwer 2003, New York, NY.
73. Park WI, Yi GC, Kim MY, Pennycook SJ. ZnO nanoneedles grown vertically on Si substrates by non-catalytic vapor-phase epitaxy. Adv. Mater. 2002, 14, 1841-1843.
74. Yang PD, Yan HQ, Mao S, Russo R, Johnson J, Saykally R, Morris N, Pham J, He RR, Choi HJ. Controlled growth of ZnO nanowires and their optical properties. Adv. Func. Mater. 2002, 12, 323-331.
75. Manna L, Scher EC, Alivisatos AP. Shape control of colloidal semiconductor nanocrystals. J. Cluster Science 2002;13:4, 521-532.

76. Meulenkamp EA. Size dependence of the dissolution of ZnO nanoparticles. J. Physical Chemistry B 1998; 102:40, 7764-7769.
77. Sakohara S, Ishida M, Anderson MA. Visible luminescence and surface properties of nanosized ZnO colloids prepared by hydrolyzing zinc acetate. J. Physical Chemistry B 1998; 102:50, 10169-10175.
78. McBride RA, Kelly JM, McCormack DE. Growth of well-defined ZnO microparticles by hydroxide ion hydrolysis of zinc salts. J. Materials Chemistry 2003;13:5, 1196-1201.
79. Pacholski C, Kornowski A, Weller H. Self-Assembly of ZnO: From nanodots to nanorods. Angew. Chem. Int. Ed. 2002; 41:7, 1188-1191.
80. Andelman T, Gong Y, Polking M, Win M, Kuskovsky I, Neumark G, O'Brien S. Morphological control and photoluminescence of zinc oxide nanocrystals. J. Physical Chemistry B 2005; 109, 14314 -14318.
81. Peng XG, Manna L, Yang WD, Wickham J, Scher E, Kadavanich A, Alivisatos P. Shape control of CdSe nanocrystals. Nature 2000; 404:6773, 59-61.
82. Lee YJ, Sounart TL, Scrymgeour DA, Voigt JA, Hsu JWP. Control of ZnO nanorod array alignment synthesized via seeded solution growth. J. Crystal Growth 2007; 304:1, 80-85.
83. Nosker RW, Mark P, Levine JD. Polar surfaces of wurtzite and zinc blende lattices. Surface Sci. 1970, 19, 291-317.
84. Dulub O, Boatner LA, Diebold U. STM study of the geometric and electronic structure of ZnO(0001)-Zn, (0001)-O, (1010), and (1120) surfaces. Surf. Sci. 2002, 519, 201-217.
85. Govender K, Boyle DS, Kenway PB, O'Brien P. Understanding the factors that govern the deposition and morphology of thin films of ZnO from aqueous solution. J. Mater. Chem. 2004, 14:16, 2575-2591.
86. Yamabi S, Imai H. Growth conditions for wurtzite zinc oxide films in aqueous solutions. J. Mater. Chem. 2002, 12:12, 3773-3778.
87. Hung CH, Whang WT. A novel low-temperature growth and characterization of single crystal ZnO nanorods. J. Mater. Chem. Phys. 2003, 82, 705-710.
88. Sounart TL, Liu J, Voigt JA, Hsu JWP, Spoerke ED, Tian Z, Jiang Y. Sequential nucleation and growth of complex nanostructured films. Adv. Func. Mater. 2006, 16, 335-344.
89. Taubert A, Kubel C, Martin DC. Polymer-induced microstructure variation in zinc oxide crystals precipitated from aqueous solution. J. Phys. Chem. B 2003, 107: 12, 2660-2666.
90. Hubbard, AT. Encyclopedia of Surface and Colloid Science. CRC Press, 2004, 4230.
91. Greene LE, Law M, Goldberger J, Kim F, Johnson JC, Zhang Y, Saykally RJ, Yang P. Low-Temperature Wafer-Scale Production of ZnO Nanowire Arrays. Angew. Chem. Int. Ed. 2003, 42, 3031 – 3034.
92. Bowden N, Brittain S, Evans AG, Hutchinson JW, Whitesides GM. Spontaneous formation of ordered structures in thin films of metals supported on an elastomeric polymer. Nature 1998, 393, 146-149.

93. Cerda E, Mahadevan L. Geometry and physics of wrinkling. Phys. Rev. Lett. 2003, 90;7, 074302.
94. Zhang T, Dong W, Keeter-Brewer M, Konar S, Njabon RN, Tian ZR. Site-specific nucleation and growth kinetics in hierarchical nanosyntheses of branched ZnO crystallites. J. Amer. Chem. Soc. 2006, 128, 10960-10968.
95. Niquet YM. Effects of a shell on the electronic properties of nanowire superlattices. Nano Lett. 2007, 7, 1105-1109.
96. Vayssieres L, Keis K, Hagfeldt A, Lindquist SE. Three-dimensional array of highly oriented crystalline ZnO microtubes. J. Mater. Chem. 2001, 13, 1-3.
97. Li Q, Kumar V, Li Y, Zhang H, Marks TJ, Chang RPH. Fabrication of ZnO nanorods and nanotubes in aqueous solutions. Chem. Mater. 2005, 17, 1001-1006.
98. Brooks GA, Fahey TD, Baldwin KM. Exercise Physiology: Human bioenergetics and its applications. 2005, Mcgraw-Hill, Boston, MA.
99. Shenck NS, Paradiso JA. Energy scavenging with shoe-mounted piezoelectrics. IEEE Micro 2001, 21, 30-42.
100. Axel L. Biomechanical dynamics of the heart with MRI. Annu. Rev. Biomed. Eng. 2002, 4, 321-347.
101. Haber I, Metaxas DN, Axel L. Three-dimensional motion reconstruction and analysis of the right ventricle using tagged MRI. Med. Image Anal. 2000, 4, 335-355.
102. Juvinall RC, Marshek KM. Fundamentals of machine component design. 3rd Ed. Wiley 2000, New York, NY.
103. Wang JW. The mechanical behavior of a pacemaker lead. In preparation, 2008.
104. Wickramasinghe VK, Hagood NW. Material characterization of active fiber composites for integral twist-actuated rotor blade application. Smart Mater. Struct. 2004, 13, 1155-1165.
105. Jungk T, Hoffmann A, Soergel E. Influence of the inhomogeneous field at the tip on quantitative piezoresponse force microscopy, Appl. Phys. A 2007, 86, 353-355.
106. Satyanarayana S, Karnik RN, Majumdar A. Stamp-and-stick room temperature bonding technique for microdevices. J. Microelectromech. Sys. 2005, 14, 392-399.
107. Jones J, Lacour SP, Wagner S, Suo Z. Stretchable wavy metal interconnects. J. Vac. Sci. Tech. A 2004, 22, 1723-1725.
108. Sun Y, Choi WM, Jiang H, Huang Y, Rogers JA. Controlled buckling of semiconductor nanoribbons for stretchable electronics. Nature Nano. 2006, 1, 201-207.
109. Kucheyev SO, Bradby JE, Williams JS, Jagadish C, Swain MV. Mechanical deformation of single-crystal ZnO. Appl. Phys. Lett. 2002, 80, 956-958.
110. Stan G, Ciobanu CV, Parthangal PM, Cook RF. Diameter-dependent radial and tangential elastic moduli of ZnO nanowires. Nano Lett. 2007, 7, 3691-3697.
111. Suhr J, Victor P, Ci L, Sreekala S, Zhang X, Nalamasu O, Ajayan PM. Fatigue resistance of aligned carbon nanotube arrays under cyclic compression. Nature Nano., 2, 417 – 421.
112. Sze S. Physics of Semiconductor Devices. 2nd Ed. Wiley, New York, New York. 1981.
113. Bardeen J. Surface states and rectification at a metal-semiconductor contact. Phys. Rev. 1947, 71, 717-727.

114. Salomon A, Berkovich D, Cahen D. Molecular modification of an ionic semiconductor-metal interface: ZnO/molecule/Au diodes. Appl. Phys. Lett. 2003, 82, 1051-53.
115. Tersoff J. Schottky barriers and semiconductor band structures. Phys. Rev. B 1985, 32, 6968-6971.
116. Goldberger J, Sirbuly DJ, Law M, Yang P. ZnO nanowire transistors. J. Phys. Chem. B, 2005, 109, 9-14.
117. Sfeir MY, Wang F, Huang LM, Chuang CC, Hone J, O'Brien SP, Heinz TF, Brus LE. Probing electronic transitions in individual carbon nanotubes by Rayleigh scattering. Science 2004, 306**,** 1540-1543**.**
118. Sfeir MY, Beetz T, Wang F, Huang L, Huang X, Huang M, Hone J, O'Brien S, Misewich J, Heinz TF, Wu L, Zhu Y, Brus LE. Optical Spectroscopy of Individual Single-Walled Carbon Nanotubes of Defined Chiral Structure. Science 2006, 312, 554-556.
119. Bachilo SM, Strano MS, Kittrell C, Hauge RH, Smalley RE, Weisman RB. Structure-assigned optical spectra of single-walled carbon nanotubes. Science 2002, 298, 2361-2366**.**
120. Vogel EM. Technology and metrology of new electronic materials and devices. Nature Nano. 2007, 2, 25-32.
121. Haight R, Sirinakis G, Reuter M. Photoelectron spectroscopy of individual nanowires of Si and Ge. Appl. Phys. Lett. 2007, 91, 233116.
122. Koralek JD, Douglas JF, Plumb NC, Griffith JD, Cundiff ST, Kapteyn HC, Murnane MM, Dessau DS. Experimental setup for low-energy laser-based angle resolved photoemission spectroscopy. Rev. Sci. Instr. 2007, 78, 053905.
123. Seah MP, Dench WA. Quantitative electron spectroscopy of surfaces: A standard data base for electron inelastic mean free paths in solids. Surf. Inter. Analy. 1979, 1, 2-11.
124. Ashkenasy G.; Cahen, D.; Cohen R.; Shanzer A.; Vilan A. Molecular engineering of semiconductor surfaces and devices. Acc. Chem. Res. 2002, 35, 121-128.
125. Haight R. Electron dynamics at surfaces. Surf. Sci. Rep. 1995, 21, 275-325.
126. Aguilar CA, Mavrokefalos A, Korgel BA, Chen SC, Haight R. Electronic Properties of Molecular Engineered Zinc Oxide Nanostructures. 2008, to be submitted.
127. Seker F, Meeker K, Kuech TF, Ellis AB. Surface chemistry of prototypical bulk II-VI and III-V semiconductors and implications for chemical sensing. Chem. Rev. 2000, 100, 2505-2536.
128. Barsan N, Weimar U. Conduction model of metal oxide gas sensors. J. Electroceram. 2001, 7:143–67.
129. Arnold MS, Avouris P, Pan ZW, Wang ZL. Field-effect transistors based on single semiconducting oxide nanobelts. J. Phys. Chem. B 2003, 107, 659-663.
130. Takahashi Y, Kanamori M, Kondoh A, Minoura H, Ohya Y. Photoconductivity of ultrathin zinc oxide films. Jpn. J. Appl. Phys. 1994, 33, 6611-6615.
131. Jacobi K, Zwicker G, Gutmann A. Work function, electron affinity and band bending of zinc oxide surfaces. Surf. Sci. 1984, 141, 109-125.
132. Kolmakov A, Moskovits M. Chemical sensing and catalysis by one-dimensional metal-oxide nanostructures. Annu. Rev. Mater. Res. 2004, 34, 151–80.

133. Vilan A, Cahen D. How organic molecules can control electronic devices. Trends in Biotech. 2002, 20, 22-29.
134. Gao W, Dickinson L, Grozinger C, Morin FG, Reven, L. Self-assembled monolayers of alkylphosphonic acids on metal oxides. Langmuir 1996, 12, 6429-6435.
135. Mutin PH, Guerrero G, Vioux A. Hybrid materials from organophosphorus coupling molecules. J. Mater. Chem. 2005, 15, 3761-3768.
136. Hanson EL, Schwartz J, Nickel B, Koch N, Danisman MF. Bonding self-assembled, compact organophosphonate monolayers to the native oxide surface of silicon. J. Am. Chem. Soc. 2003, 125, 16074-16080.
137. Gouzman I, Dubey M, Carolus MD, Schwartz J, Bernasek SL. Monolayer vs multilayer self-assembled alkylphosphonate films:X-ray photoelectron spectroscopy studies. Surf. Sci. 2006, 600, 773-381.
138. Randon J, Blanc P, Paterson R. Modification of ceramic membrane surfaces using phosphoric-acid and alkyl phosphonic-acids and its effects on ultrafiltration of BSA protein. J. Membrane Sci. 1995, 98, 119-129.
139. Koh SE, Mcdonald KD, Holt DH, Dulcey CS, Chaney JA, Pehrsson PE. Phenylphosphonic acid functionalization of indium tin oxide: surface chemistry and work functions. Langmuir 2006, 22, 6249-6255.
140. Cahen D, Hodes G. Molecules and electronic materials. Adv. Mater. 2002, 14, 789-798.
141. Bescocke K, Krahl-Urban B, Wagner H. Dipole moments associated with edge atoms; a comparative study on stepped Pt, Au and W surfaces. Surf. Sci. 1977, 68, 39-46.
142. Chiou JW, Kumar KPK, Jan JC, Tsai HM, Bao CW, Pong WF, Chien FZ, Tsai MH, Hong IH, Klauser R, Lee JF, Wu JJ, Liu SC. Diameter dependence of the electronic structure of ZnO nanorods determined by x-ray absorption spectroscopy and scanning photoelectron microscopy. Appl. Phys. Lett. 2004, 85, 3220-3222.

# Vita

Carlos Andres Aguilar was born in San Antonio, Texas, the son of Raul and Cynthia Aguilar. He graduated from Edinburg High School in Edinburg, Texas in 1998. He attended the University of Michigan in Ann Arbor, Michigan where he graduated with a bachelor's of science in mechanical engineering in 2002. Carlos then entered the University of Texas at Austin in 2003, where he received a master's of science in mechanical engineering in 2005. Upon completion, he entered the doctoral program in biomedical engineering at Texas. He worked as a research intern and visiting scientist at I.B.M.-T.J. Watson Research Center in Yorktown Heights, New York in 2006 and 2008, respectively. While at Texas he received the HENAAC-Graduate Student Leadership Award and University Co-Op/George H. Mitchell Award for Excellence in Graduate Research and was inducted into Tau Beta Pi.

Permanent address: 1320 S. 7th, Edinburg, TX 78539

This dissertation was typed by the author.

***S.D.G.***